Intercalation in High-Temperature Oxide and Fullerene Superconductors

by

William Alan Vareka

B.S. (University of Wisconsin at Madison) 1983
M.S. (University of Illinois at Urbana-Champaign) 1985

A dissertation submitted in partial satisfaction of the requirements for the degree of

DOCTOR OF PHILOSOPHY

in

PHYSICS

in the

GRADUATE DIVISION

of the

UNIVERSITY of CALIFORNIA at BERKELEY

Committee in charge:

Professor Alex Zettl, Chair
Professor Marvin L. Cohen
Professor Norman Phillips

1993

The dissertation of William Alan Vareka is approved:

Alex Zettl Nov. 16, 1993
Chair Date

Marvin L. Cohen Nov. 16, 1993
Date

Norman E. Phillips November 18, 1993
Date

University of California at Berkeley

1993

Intercalation in High-Temperature Oxide and Fullerene Superconductors

Copyright 1993

by

William Alan Vareka

Abstract

Intercalation in High-Temperature Oxide and Fullerene Superconductors

by

William Alan Vareka

Doctor of Philosophy in Physics

University of California at Berkeley

Professor Alex Zettl, Chair

This thesis work has mainly been comprised of using intercalation and pressure techniques to examine the physical properties of the high T_c oxide and fullerene superconducting materials. We discovered the first epitaxially intercalated high T_c oxide compound: Iodine-$Bi_2Sr_2CaCu_2O_x$ (I-BSCCO). In an effort to probe the underlying superconducting mechanism, I conducted a series of studies on the intercalation of all members of the BSCCO family, on the correlation of stage index and superconducting transition temperature, and on the effect of intercalation on the electro- and magneto-transport properties in this material. These studies have imposed strict constraints on models for the superconductivity in the oxides by coupling the expansion of the **c**-axis lattice parameter, the small reduction in the transition temperature, the reduction of the inter-layer coupling and the dramatic change in the **c**-axis conduction properties.

In addition to my work on the high T_c oxide superconductors, I have also worked on intercalation into single crystals of C_{60} (fullerene) with potassium and rubidium. These novel superconductors have generated considerable interest due to their unique

crystal structure and their relatively high transition temperatures. I have performed an extensive study on the pressure and temperature dependence of the electrical resistivity in the Rb_3C_{60} compound. This study has helped to clarify the normal state electrical transport properties and has allowed us to put bounds on fundamental parameters like the electron-phonon coupling strength.

To Susan with loving appreciation

Table of Contents

List of Figures

List of Tables

Acknowledgments

First and foremost I would like to acknowledge my wife Susan for her nearly infinite patience and understanding. She took in stride my long nights in the lab and prolonged sessions in front of the computer and was always there for me when I needed her most. Though she might not believe it, the "3-years" are really over. To my daughter Jaime I can only say that, although you may not yet realize it, your bright face and little laugh had the power to erase away in an instant any temporary disappointment I had during my research. Watching you grow up has been and will always be one of the greatest sources of joy in my life. I can't imagine completing this work without both of you at my side. In addition, I want to thank my Mom and Dad for all their support and encouragement. They gave me the independence and strength necessary to succeed in reaching this point and the self-confidence to know that I will be successful in anything I put my mind to in the future. I also wish to thank my brothers and sisters. To John, for showing me strength of character and perseverance. To Jim and Barb (yes you're my sister), for showing me commitment and dedication to family. To Anne, for showing me independence and Carolyn for showing me that we can overcome any adversity through dedication and hard work. And to Jean, for showing me that what first may look like self-sacrifice can actually return the greatest rewards.

Next I would like to thank Professor Alex Zettl for giving me the opportunity to work with and learn from him. As a thesis advisor, he provided an invaluable list of intriguing and exciting projects and the knowledge necessary to make them successful. Alex's unique combination of insight, intelligence, and sense of humor not only made my time in his group enjoyable but also made group meetings worth missing cookies over. I also thank Professor Marvin Cohen who helped to unravel and interpret our experimental results. In addition, I will always remember when he took the time out of his schedule to

talk to me when I first considered coming to Berkeley. That conversation helped to finalize my decision to come to UCB. To Professor Raymond Chiao I also give a special thanks. In the year and a half that I worked with Ray I found him to be one of the most intelligent, kind-hearted persons I've known. His enthusiasm and excitement in physics, and in the pursuit of knowledge in general, is unparalleled.

Much of the work done in this thesis was in collaboration with others. In particular, I have benefited enormously by working closely with Xiao-Dong Xiang. XD was able to do in days what might have otherwise taken months. His insight into theoretical and experimental problems is something I strive to emulate. I also wish to thank the other members of the Zettl group that I have worked with. Bill Creager, whose H-P computer program I freely lifted from to build the data acquisition system on the Mac. Ian Parker who built (and taught me how to use) the pressure cell I relied so heavily on for the latter part of this thesis. Stors Hoen with his mad scientist picture that still makes me laugh when I think of it. Mike Crommie who taught me how to paint contacts on mere specs of samples and who is truly becoming a computer nerd in his own right. Brian Burk who seemed to be able to build a new specialized probe in an afternoon. Gabrial Briceño who taught me how to bring the superconducting magnet to life. My only regret was introducing him to *Maelstrom*. Jian Gou Hou and Li Lu (or is it Lu Li?) who were always more than willing to help me work out any problem I was having. Mike Fuhrer who was the envy of the APS meeting for the C_{60} crystals he could grow. Nasreen Chopra who is learning the lessons of time management: "estimate the time required to complete the project, multiply by two, add three and increase to the next unit of time; hours, days, weeks, etc." Even with this hard lesson she continues to show the most outgoing excitement in research of anyone I know. Kasra Kashi, may math forever serve you well. Phil Collins, thanks for taking over LabView so that all my work does not become obsolete. And finally, Kelly Cherrey, who is only now pulling himself

from the quicksand of internet but has also not only kept up but significantly improved the lab computer system while I was diligently writing this thesis. All of you have made the lab a truly enjoyable place to work.

Outside of the Zettl lab there are also a number of people who helped to make the last six plus years of graduate school a pleasure. First, Paul Kwiat who's own father when asked if Paul was the smartest of his children, replied,"He's the smart aleckiest!" May you never lose that sharp sense of humor. To Steve Johnson and Peter Grudberg I wish to say that after our first two years of graduate school I knew I could live through just about anything (except maybe another two years like that!) To the three of you and all the others associated with our adventure I'd like to say that no matter how it ends, we have all gained by the experience. And finally I would like to thank Dwight Fronsdahl for being the best friend I could ever ask for. Whenever I needed help, you were there and when I needed to recharge my batteries you showed me Bonny Dune Road.

Vita

May 3, 1960	Born in Appleton, Wi.
September 1980 to December 1983	B.S. in Physics at the U. of Wisconsin at Madison
September 1984 to September 1985	M.S. in Physics at the U. of Illinois at Urbana-Champaign
November 1985 to August 1987	Associate Engineer at Lockheed Missiles and Space Co.
October 1987 to December 1988	Technical consultant to Lockheed Aircraft Service Co.
August 1987 to December 1993	Teaching and research assistant, Department of Physics, U. of California at Berkeley

Publications

1. P. G. Kwiat, W. A. Vareka, C. K. Hong, H. Nathel and R. Y. Chiao: Correlated two-photon interference in a dual-beam Michelson interferometer, *Phys. Rev. A* **41**, 2910 (1990).

2. X.-D. Xiang, S. McKernan, W. A. Vareka, A. Zettl, J. L. Corkill, T. W. Barbee and Marvin L. Cohen: Iodine intercalation of a high-temperature superconducting oxide, *Nature* **348**, 145 (1990).

3. X.-D. Xiang, A. Zettl, W. A. Vareka, J. L. Corkill, T. W. Barbee and Marvin L. Cohen: Epitaxial intercalation of the Bi-Sr-Ca-Cu-O superconductor series, *Phys. Rev. B* **43**, 11496 (1991).

4. N. Kijima, R. Gronsky, X.-D. Xiang, W. A. Vareka, A. Zettl, J. L. Corkill and Marvin L. Cohen: Crystal structure of stage-1 iodine-intercalated superconducting $IBi_2Sr_2CaCu_2O_x$, *Physica C* **181**, 18 (1991).

5. N. Kijima, R. Gronsky, X.-D. Xiang, W. A. Vareka, A. Zettl, J. L. Corkill and Marvin L. Cohen: Crystal structure of stage-2 iodine-intercalated superconducting $IBi_4Sr_4Ca_2Cu_4O_x$, *Physica C* **184**, 127 (1991).

6. X.-D. Xiang, W. A. Vareka, A. Zettl, J. L. Corkill, T. W. Barbee, Marvin L. Cohen, N. Kijima and R. Gronsky: Tuning high-T_c superconductors via multistage intercalation, *Science* **254**, 1487 (1991).

7. N. Kijima, R. Gronsky, X.-D. Xiang, W. A. Vareka, A. Zettl, J. L. Corkill and Marvin L. Cohen: Crystal structures of stage-n iodine-intercalated compounds $IBi_{2n}Sr_{2n}Ca_nCu_{2n}O_x$, *Physica C* **190**, 597 (1992).

8. X.-D. Xiang, W. A. Vareka, A. Zettl, J. L. Corkill, Marvin L. Cohen, N. Kijima and R. Gronsky: Metallization of the resistivity tensor in $Bi_2Sr_2CaCu_2O_x$ through epitaxial intercalation, *Phys. Rev. Lett.* **68**, 530 (1992).

9. N. Kijima, R. Gronsky, X.-D. Xiang, W. A. Vareka, J. Hou, A. Zettl, J. L. Corkill and Marvin L. Cohen: Structural properties of stage-1 iodine-intercalated superconducting $I(Bi_{0.915},Pb_{0.085})_2(Sr_{0.93},Pb_{0.07})_2(Ca_{0.965},Pb_{0.035})_2Cu_3O_x$, *Physica C* **198**, 309 (1992).

10. X.-D. Xiang, J. G. Hou, G. Briceno, W. A. Vareka, R. Mostovoy, A. Zettl, V. H. Crespi and Marvin L. Cohen: Synthesis and electronic transport of single crystal K_3C_{60}, *Science* **256**, 1190 (1992).

11. S. L. Dexheimer, D. M. Mittleman, R. W. Schoenlein, W. Vareka, X. Xiang, A. Zettl and C. V. Shank, Ultrafast dynamics of solid C_{60}, J. L. Martin, A. Migus, G. A. Mourou and A. H. Zewails, Eds., Ultrafast Phenomena VIII (Springer-Verlag, 1992), pp. 81.

12. S. Hoen, N. G. Chopra, X.-D. Xiang, R. Mostovoy, J. Hou, W. A. Vareka and A. Zettl: Elastic properties of a van der Waals solid: C_{60}, *Phys. Rev. B* **46**, 12737 (1992).

13. J. G. Hou, V. H. Crespi, X.-D. Xiang, W. A. Vareka, G. Briceno, A. Zettl and Marvin L. Cohen: Determination of superconducting and normal state parameters of single crystal K_3C_{60}, *Solid State Comm.* **86**, 643 (1993).

14. S. L. Dexheimer, D. M. Mittleman, R. W. Schoenlein, W. Vareka, X. Xiang, A. Zettl and C. V. Shank, Ultrafast dynamics of photoexcited C_{60}, T. R. Gosnell, A. J. Taylor, K. A. Nelson and M. C. Downers, Eds., Ultrafast pulse generation and spectroscopy (SPIE Proceedings, 1993), vol. 1861, pp. 328.

15. S. L. Dexheimer, W. Vareka, A. Zettl and C. V. Shank: Nonexponential relaxation in solid C_{60} via time-dependent singlet exciton annihilation, *Submitted to Phys. Rev. Lett.*, (1993).

16. W. A. Vareka and A. Zettl: Linear temperature dependent resistivity at constant volume in Rb_3C_{60}, *Submitted to Phys. Rev. Lett.*, (1993).

Chapter 1

Introduction

1.1 General introduction

It took over 45 years from the initial discovery[1] of superconductivity in Hg for the development of a microscopic theory of this phenomenon. The theory of Bardeen-Cooper-Schrieffer (BCS)[2] and the subsequent extensions of Eliashberg[3] and McMillan[4] have been very successful in explaining many of today's superconductors. In 1986, a new class of superconductors[5] referred to as the high T_c oxides was discovered. These new layered compounds raised the maximum obtainable superconducting transition temperature in just two years from 23.2 K in Nb_3Ge prior to their discovery to 125 K in the Tl-based compound. Recently[6] that number has increased to ~160 K for the Hg-based compounds under externally applied pressure. In the seven years since their discovery, no consensus has yet been reached as to whether or not superconductivity in these materials can be explained within the framework of the BCS formalism or if it will be necessary to consider more exotic mechanisms, e.g., the model of Wheatley, Hsu, and Anderson.[7]

The one common element in all the high T_c oxides is the presence of CuO_2 sheets. These sheets are believed to be the critical structural unit related to the superconductivity in these compounds. For all the basic high T_c compounds there are one or several CuO_2 sheets separated from each other by one atomic layer and these are then separated from the next set of CuO_2 sheets by a one or more intervening atomic spacer layers. As a result, these materials display a very layered-like structure with a high anisotropy between in-plane and out-of-plane behavior. We set out to use intercalation techniques to tune this anisotropy in a controlled way. This would allow us to carefully probe the role of this anisotropy on the normal and superconducting state parameters of these materials. Since many models directly couple the anisotropy to the superconducting and normal

state parameters, this study could not only produce a new variety of high T_c superconductors, but also could provide critical constraints within which the models must remain.

In the rest of this chapter I will give some background information on the intercalation technique. This general knowledge was the starting point for this research. As a representative structure of the high T_c oxides we chose to first intercalate $Bi_2Sr_2CaCu_2O_x$ (Bi-2212) which has the highest degree of anisotropy and the most micaceous morphology of all the high T_c oxides. This compound is discussed more fully in chapter 2. In chapter 3 I will discuss in detail the technique used to intercalate this compound and the other closely related compounds of the Bi-family. X-ray and transmission-electron-microscopy (TEM) results are presented which conclusively show that these compounds have been successfully intercalated. I then set out to perform numerous studies on the effects of intercalation on the normal and superconducting state parameters in these new intercalated high T_c materials. Chapter 4 will focus on how intercalation can be used to tune the superconducting transition temperature. In addition, I will look at the effect of staging (described below) on T_c. In chapter 5, I will address the effects of intercalation on the electrical transport properties. In particular, how does intercalation affect the huge anisotropy between the in-plane and out-of-plane conductivity and their intrinsic temperature dependencies? Finally, chapter 6 will consider the anisotropic conductivity when the material is placed in a high magnetic field. This chapter ends the first part of this thesis on intercalation in the high T_c oxides.

Early in 1991 another new superconducting material was discovered,[8] K_3C_{60}. This compound is based on the extremely unusual molecule of C_{60} (fullerene), consisting of 60 carbon atoms in an icosahedral cage-like structure. By intercalating the host C_{60} material with alkali-metals one obtains superconductors with transition temperatures ~150% of the pre-high T_c oxide record in Nb_3Ge. Given the exotic nature of this

material, again the questions arose as to whether or not the BCS theory would be capable of explaining the superconductivity. The second part of this thesis is concerned with these alkali-metal intercalated fullerene compounds. In chapter 7, I will discuss some of the background information on C_{60} and A_3C_{60} (A = alkali-metal). We were the first group to measure the true intrinsic temperature dependence of the resistivity in these materials and these experiments are covered in chapter 8. Finally, in chapter 9, I will discuss experiments performed on the pressure dependence of the resistivity. These experiments showed that the increase in the lattice constant which occurs due to thermal expansion when the material is warmed from T_c to room temperature has a considerable impact on the measured temperature dependence of the resistivity performed at constant pressure. To obtain the more theoretically relevant constant volume resistivity, I measured the resistivity while changing both temperature and pressure. This experiment allowed us to extract the temperature dependence of the constant volume resistivity from which we could then set bounds on fundamental parameters like the electron-phonon coupling constant.

1.2 Introduction to intercalation

Intercalation is defined as the insertion of guest atoms or molecules into a pre-existing host structure. The guest species or intercalant migrates into voids or weakly bonded regions in the host structure thereby leaving intact the main structural features of the host. The interaction of the intercalant and host can result in a wide range of changes to the physical, geometric, chemical, electronic, and optical properties of the original host structure. Numerous materials from insulators (e.g., MoO_3, zeolites, and clays) to semiconductors (e.g., graphite) to metals (e.g., $LaNi_5$) can serve as host structures. The intercalants cover an equally wide array from alkali-metals to halides to inorganic and organic molecules. Generally only one species at a time is intercalated into the host

structure but cointercalated systems do exist in which more than one species simultaneously intercalates. By suitably choosing the intercalant one can control the parameters of the system in an attempt to tailor them for the desired behavior. For example, through intercalation the host can be changed[9] from insulating to semiconducting to metallic or the anisotropy in the material can be changed by several orders of magnitude or the superconducting transition temperature can be radically increased.

The bonding in the host structure can be used to classify the type of intercalation observed for that material. Fig. 1.1 shows a schematic of the three different types of bonding found in the host material. The first, Fig. 1.1(a) represents a material consisting of one-dimensional chains which are locally aligned and are weakly coupled to each other. In a material of this type the guest species intercalates between the long chains in the weakly bonded regions. An example of a material of this form is $NbSe_3$ which can be intercalated with many materials including potassium and rubidium. The second morphology, Fig. 1.1(b) is the most commonly studied host structure. It consists of a layered structure where the bonding between a pair of layers is typically a weak van der Waals type force. Numerous host structures of this type are known with graphite and the transition metal dichalcogenides being the most studied and best understood. In the case of graphite each hexagonally bonded graphitic sheet is weakly coupled to its neighbor so the host slab is a single layer of carbon atoms one atom thick. In the dichalcogenides, a layer of transition metal atoms (T) is sandwiched between two layers of chalcogen atoms (X). These three layer TX_2 sandwiches or blocks are only weakly coupled to each other as is demonstrated by the fact that the crystals can be easily cleaved. These two hosts have been intercalated with the widest variety of guest species. The third form of bonding has a host structure shown schematically in Fig. 1.1(c) consisting of a 3-dimensional type bonding. In this type of structure a 3-dimensional network of voids

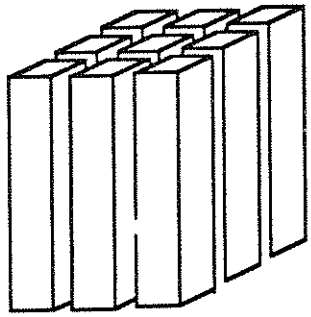

(a)

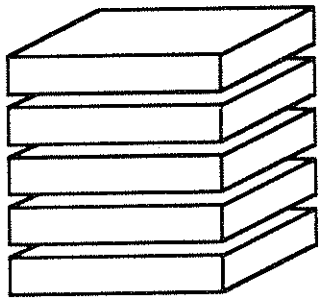

(b)

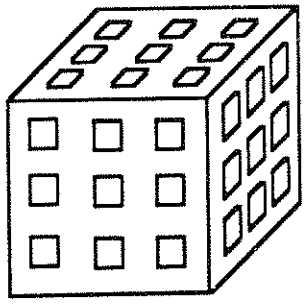

(c)

Figure 1.1 Dimensionality of bonding in host structures used for intercalation. (a) one-dimensional, (b) two-dimensional or layered, (c) three-dimensional.

exists in the host structure and it is in these voids that the intercalant resides. One example of this structure is zeolite (commonly used as a molecular sieve) which consists of silica and alumina tetrahedra linked together to form a cubooctahedron. Another beautiful example of this type of 3-d weak bonding occurs in solid C_{60} which is discussed later.

To simplify this introduction, I will limit the rest of the discussion to the layered host structures; however the results can be carried over equally as well to the 1-d and 3-d bonded host structures. In most cases the intercalant registers onto a grid pattern related to the host structure. However, some intercalants can undergo a kind of two-dimensional 'melting' at some transformation temperature[10] resulting in a 'liquid-like' disordered state. The most common physical effect of intercalation in a layered structure is the expansion of the system perpendicular to the layers which I will refer to as the **c**-axis. This expansion can vary dramatically even in the same host structure and is closely related to the size of the intercalant. For example[9], TaS_2 intercalated with Li undergoes little or no **c**-axis expansion whereas if it is intercalated with the long-chain organic molecule octadecylamine the gap between the blocks can be expanded by nearly 60 Å since these molecules line up end to end between the TaS_2 blocks. Clearly the coupling between the original host blocks can be significantly modified by the presence of an intercalant allowing us to probe the inherent dimensionality in the original system. In TaS_2, for example,[11] the compound was still superconducting even after the intercalation of the long chain amines which separated the individual blocks by almost 60 Å. This strongly suggested that the superconductivity in this material was truly two-dimensional in nature. Further studies[11] using magnetic intercalants proved this fact. It was the combined nature of modifying the block-block coupling while leaving intact the intra-block structure that makes intercalation ideally suited for this type of study.

Although there are a broad range of intercalants available, generally only a limited subset will actually intercalate into a given host structure. In addition to geometric constraints which limit what species will intercalate based on the intercalant size and bonding distances, another property which often restricts what types of intercalants will enter a host is charge transfer. As one of the driving forces of the intercalation process,[12] typically one observes that there is a net charge transfer between the guest and host species. Most hosts will only readily accept either charge donors or charge acceptors as intercalants. Graphite is an exception to this rule since it can easily be intercalated with either type of guest species. This charge transfer can dramatically affect the conduction properties of the host structure. In the graphite intercalation compounds (GIC's) this charge transfer can increase the in-plane conductivity by more than an order of magnitude making it as good of a conductor as copper at room temperature. This, when combined with the intercalation induced reduction in the **c**-axis conduction,[13] can result in an increase in the conduction anisotropy σ_{ab}/σ_c of more than three orders of magnitude.

Another phenomenon associated with intercalation in layered materials is that of staging. The stage index n identifies a structure which has n identical host layers or blocks sandwiched between each pair of intercalant layers. Fig. 1.2 shows a schematic of the staging phenomenon for stage index n = 1, 2, and 3. In the GIC's, high stage single-phase compounds can be synthesized[12] with n as high as 7, but in other layered compounds it is difficult to achieve single-phase intercalation with $n > 1$. There are three principle considerations governing the staging energetics.[12] The first is charge transfer which can lead to an effective repulsion between different guest layers. The second is elastic effects due to the distortion of the host upon intercalation of the guest species which can lead to a repulsive force between adjacent partially intercalated layers. A related issue is the cohesion between the layers which must be overcome in order for the intercalants to enter the host. And third, one must consider the interactions between guest

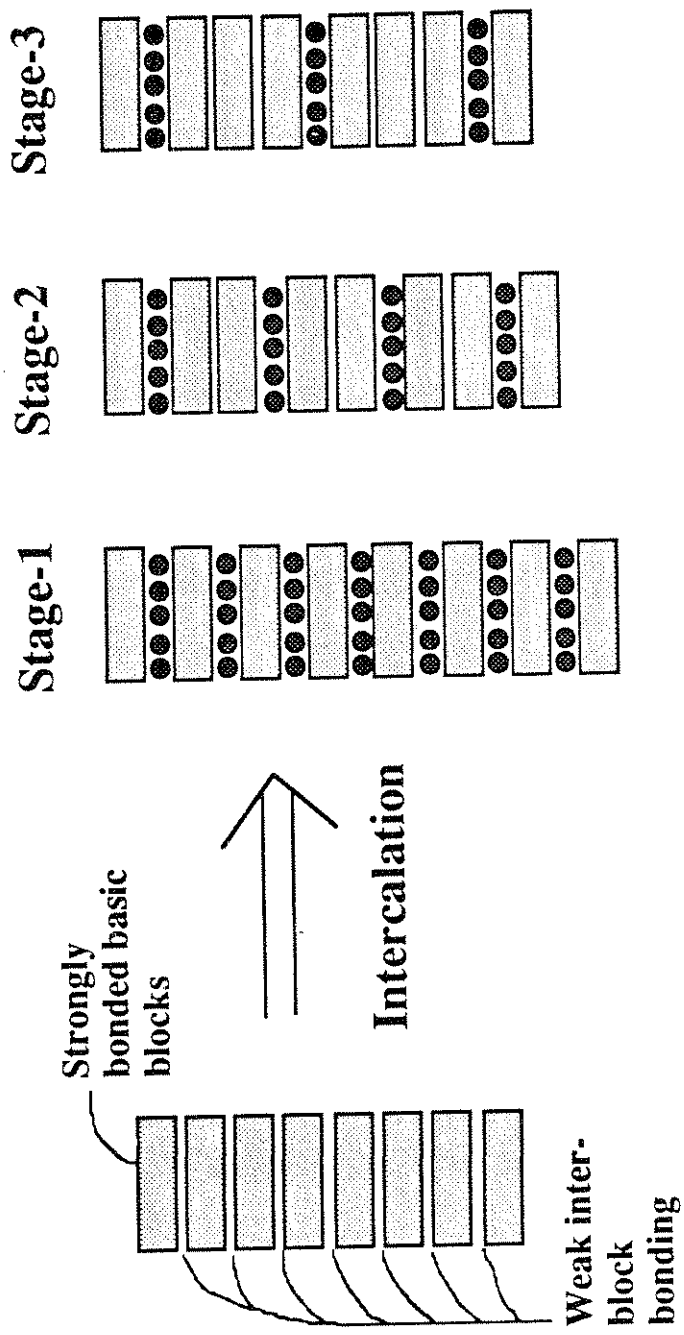

Figure 1.2 Schematic of the staging phenomena in intercalation compounds.

atoms in the same layer and between guest atoms and the adjacent host layers. By looking at different stages of the same intercalation compound one has a unique tool to systematically follow the evolution of the various parameters as the system moves from the pristine to the dilute intercalated state (high stage index) to the fully intercalated state (stage-1).

For a large number of intercalated materials, many of the effects associated with the staging process can not be explained by assuming uniformly intercalated layers like that shown schematically in Fig. 1.2. An alternate model proposed by Daumas and Hérold[14] considers the higher staged compounds to be composed of microscopic domains as shown in Fig. 1.3. Although each of the domains has the same stage index, the intercalant resides between different sets host layers for adjacent domains. A considerable increase in the entropy of the system is achieved by introducing the additional elastic deformation energy. By appropriate motion of the intercalate between domains the stage index can easily be changed from n to $n \pm 1$. This type of stage transformation does not require the intercalant to pass perpendicularly through the strongly bonded host layers or to exit the edge of the sample and then re-intercalate into nearby layers. This is consistent with several experiments[12] involving stage transformations and intercalation kinetics. In addition, this type of pleated-domain structure has been observed directly by Thomas *et al.*[15] in graphite-$FeCl_3$ using very high resolution transmission electron microscopy.

Finally, one additional point to be aware of is the interchangeable use of the words 'doped' and 'intercalated' in the literature. Provided the phenomenon being discussed is that described above, i.e., the insertion of a guest species into voids or weakly bonded regions of the host structure without significantly changing the major structural units of the host, then this interchangeability does not pose a problem. However, 'doped' often times refers to the *substitution* of one or more elements of the

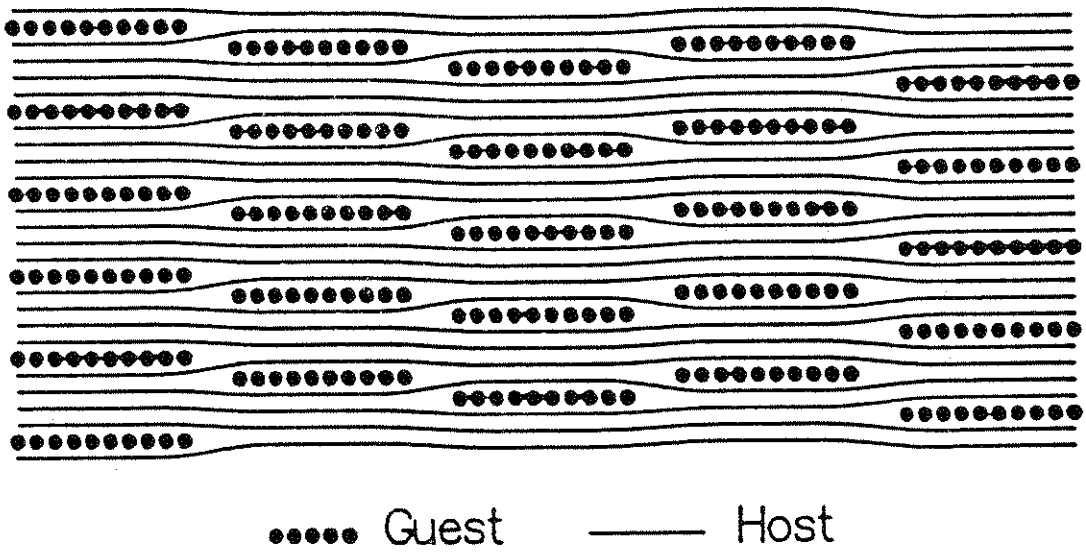

Figure 1.3 A stage-4 intercalated material in the pleated-layer model of Daumas-Hérold. The material segregates into several (5 shown here) domains each of which has same stage index but the guest atoms are located between different host layers in adjacent domains. From ref. [12].

host structure with foreign elements, e.g., doped semiconductors. Unfortunately, it is also not uncommon to find the word 'intercalated' inappropriately used to describe this substitutional effect. In the second portion of this thesis, which is concerned with the intercalation of alkali-metals into C_{60} structures, I will be using both terms interchangeably since there is no possibility for confusion and the literature on the subject typically uses the word 'doped'.

1.3 Intercalation techniques

Numerous techniques have been successfully employed to synthesize intercalated compounds including the two-zone vapor transport method, the liquid intercalation method, the electrochemical method and cointercalation techniques. Although more than one technique may be used to generate the same intercalation compound, generally the physical and chemical properties of the intercalant favor one method over the others. In addition to the intrinsic properties of the intercalant, the other significant parameters are the temperature and vapor pressure of the intercalant and the characteristics of the host material. Since the two-zone vapor transport method was the method used for virtually all of the intercalation I have done, I will briefly describe some of the generic details of this technique with a more extensive discussion given in the relevant chapters that follow. For completeness, I will then briefly describe the other techniques that can be used.

A two-zone vapor transport method of preparation is the most commonly used technique whenever the intercalant exhibits a high vapor pressure at moderate temperatures. It is also the most likely method[16] to yield well staged samples. A general schematic is shown in Fig. 1.4 along with a typical temperature profile. The zone containing the host material must be at a higher (or equal) temperature (T_h) than the zone containing the intercalant (T_i) to prevent significant condensation on the host. Generally, the reaction rate is controlled by T_h whereas the vapor pressure of the intercalate is

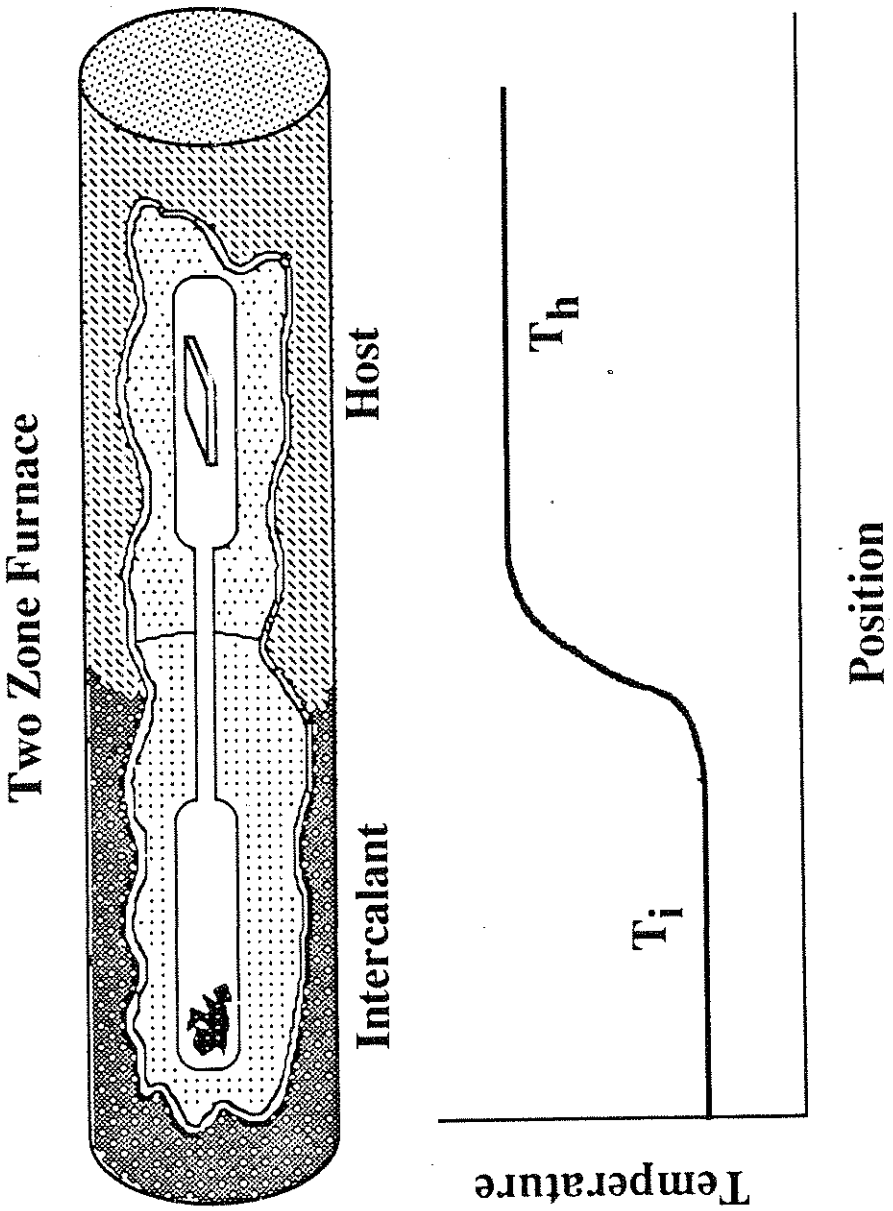

Figure 1.4 Two-zone vapor transport intercalation set-up. The intercalant is maintained at temperature T_i and the host is maintained at temperature T_h.

adjusted by T_i. By independently controlling T_h and T_i one can obtain intercalation compounds with different stages. Generally after one determines the T_i (i.e., the vapor pressure) necessary to obtain stage-1 intercalation then higher stages are produced by fixing T_i and increasing T_h. Although at first this may seem counter intuitive since increasing T_h should make it easier for the intercalant to get in, it is commonly found[17] that the rate of uptake actually decreases as the quantity $(T_h - T_i)$ increases and as a result higher stages are obtained for greater $(T_h - T_i)$. The region of stability for the formation of a given stage compound is also found to decrease with increasing stage index or equivalently $(T_h - T_i)$. A closely related technique is that of isothermal vapor transport where T_h and T_i are equal. Generally the parameter which controls the stage index is the exposure time. However, as in the case of stage-1 iodine intercalated $Bi_2Sr_2CaCu_2O_x$ discussed later, some systems may saturate at a given stage index using this technique. In addition, it is generally found that if the vapor transport method is used, the intercalation of small samples promotes the formation of a single stage over the sample volume.

Two variations of the liquid intercalation method are commonly used. If the intercalant is a liquid at the desired intercalation temperature then the host may simply be immersed in the liquid intercalant for the intercalation process to proceed. This method has been used to intercalate graphite with lithium[18] producing C_8Li. On the other hand, the liquid intercalation method can be used if a suitable solvent for the intercalant can be found. One can control the intercalation through the intercalant concentration, the liquid temperature and the immersion time. Unfortunately, this technique generally does not produce well staged samples. Also, one generally finds that some of the solvent as well as the desired intercalant may actually get into the host.

The electrochemical technique[19] consists of using the host material as one electrode in an electrolytic cell. The electrolyte must be a solvent for the intercalant,

which if it is a metal, may serve as the other electrode. With the electrochemical method both the rate and the total amount of intercalant can be precisely controlled, and de-intercalation can be achieved simply by biasing the cell with a field opposing the cell's EMF. This technique also provides an ideal way to study the thermodynamical changes accompanying a change in stage during the growth process.

In some cases[16] it is found that a given intercalant will not intercalate or will intercalate only at high stages if it is the only element present but it will go in easily if mixed with some other element or compound which also then may simultaneously intercalate the host. An example of this[16] is Na intercalating into graphite which only generates very high stages when Na alone is present but can readily be intercalated as an alloy with Cs or K. Finally, another technique related to cointercalation is that of sequential intercalation. In this method the host is first intercalated with one species (A) and then with a different species (B) which may result in a complete de-intercalation of (A) or coexistence of both (A) and (B) as intercalants.

Chapter 2

Introduction to High T_c Section

2.1 Historical review

The high T_c oxides are all layered compounds where each unit cell contains one or several parallel CuO_2 conducting planes. Each CuO_2 plane is built with one Cu atom bound with four O atoms. Generally the Cu atoms form a square lattice with the O atoms located midway between any two Cu's. Several materials like $YBa_2Cu_3O_{7-\delta}$ (YBCO) and $La_{2-x}Sr_xCuO_{4-\delta}$ undergo an orthorhombic distortion at low temperatures which distorts this somewhat. In addition to the O in the plane, one or two O atoms sit above and below the Cu atoms along a direction which is essentially normal to the CuO_2 planes. The Cu-O bond length to these out-of-plane O atoms is generally greater than those in the plane. The CuO_2 planes are separated from each other by one or more intervening atomic layers. For all the high T_c oxides, this layered nature also carries over to the transport and magnetic properties which display large anisotropies between the in-plane and out-of-plane directions. Experimental results and band theory calculations indicate that the charge carriers are much more mobile parallel to the CuO_2 planes (the **ab**-plane) than in the normal direction (**c**-axis). For example, at room temperature $\rho_{ab}/\rho_c \sim 30$ for YBCO[20] and up to $\sim 10^4$ for $Bi_2Sr_2CaCu_2O_x$ (BSCCO).

Because of the high T_c's which imply a large superconducting gap Δ, these compounds necessarily have short coherence lengths ξ. This can be seen, for example, from the BCS model which predicts

$$\xi_o = \frac{0.32\hbar v_F}{\Delta} \tag{2.1}$$

where v_F is the Fermi velocity and ξ_o is the clean limit coherence length. This, when

combined with the layered nature of these compounds, results in short coherence lengths which are nonetheless highly anisotropic. In YBCO the anisotropy is given by ξ_{ab}/ξ_c ~ 15Å / 2Å whereas for BSCCO the anisotropy is much higher with ξ_{ab}/ξ_c ~ 40Å / 1.6Å. These materials also have long magnetic penetration depths λ which are also anisotropic. Hence these materials are strongly type-II (see chapter 6) with $\lambda >> \xi$ and with anisotropies also observed in H_{c1} and H_{c2}.

It has been found that by varying the oxygen content in the high T_c materials, the superconducting transition temperature as well as the transport properties can be affected. In BSCCO, if the material is fully oxygenated by flowing pure oxygen over the sample as it is heated to 400-650°C it is found to have a superconducting transition temperature of ~ 85 K. As the oxygen is removed from the sample T_c first increases to about 91-93 K and then rapidly decreases eventually becoming non-superconducting. In general, this is believed to be caused by a charge doping effect in the CuO_2 layers with the insertion or removal of oxygen. Similar behavior can be seen if instead, one performs a substitutional doping on the constituents of some of the intervening layers. For example, again in BSCCO, if the trivalent Y is partially substituted[21] for the divalent Ca (which lies between the CuO_2 layers) there is little change in the crystal structure and yet one observes this same negative parabolic-like behavior in T_c vs. Y concentration. This question of charge doping into the CuO_2 layers will be addressed in more detail for the case of the iodine intercalated BSCCO in chapter 4.

Of all the high T_c oxides the BSCCO-family possesses the greatest degree of anisotropy. These compounds have a micaceous morphology cleaving easily between the BiO bilayers. Therefore, for the purposes of intercalation, BSCCO was chosen as the best host structure of the high T_c oxides.

2.2 $Bi_2Sr_2Ca_nCu_{(1+n)}O_{(6+2n-\delta)}$ (BSCCO)

The BSCCO-family of high T_c superconductor consists of three members with a stoichiometry given by $Bi_2Sr_2Ca_nCu_{(1+n)}O_{(6+2n-\delta)}$ with n = 1, 2, or 3. The δ is given to explicitly represent the variable oxygen content found in these materials. These compounds are commonly referred to as Bi-2201, Bi-2212, and Bi-2223 for n = 1, 2, and 3, respectively. Fig. 2.1 shows the crystal structures for these three compounds along with the associated T_c's. Table 2.1 also lists the crystals structures[22] using the standard Wyckoff notation. Refs. [22] and [23] are a good source for the crystal structures of all of the high T_c oxide compounds. Appendix A describes how to convert from the Wyckoff notation to the actual positions of the atoms. The unit cell consists of two identical perovskite-like blocks which have a shifted registry. Each block contains one, two, or three CuO_2 layers separated from each other by a Ca layer. These closely coupled CuO_2 planes are then sandwiched between a pair of SrO layers and finally two BiO layers. Therefore the bounding layers of these subunits or blocks are composed of BiO. When these blocks are stacked on top of each other there is a relative shift of $\frac{1}{2}$ **â** which results in the Bi atoms of one block being coordinated with the O atoms in the adjacent block's BiO bounding layer. Therefore the unit cell consists of two of these blocks. As is common in all high T_c's the Cu atoms are either 4-fold, 5-fold, or 6-fold coordinated with O atoms. Careful examination of the crystal structure[24] also shows that there is a superlattice modulation along the **a**-axis with a wavelength of ~ 26 Å. This modulation is believed to be mainly associated with the BiO bilayers.

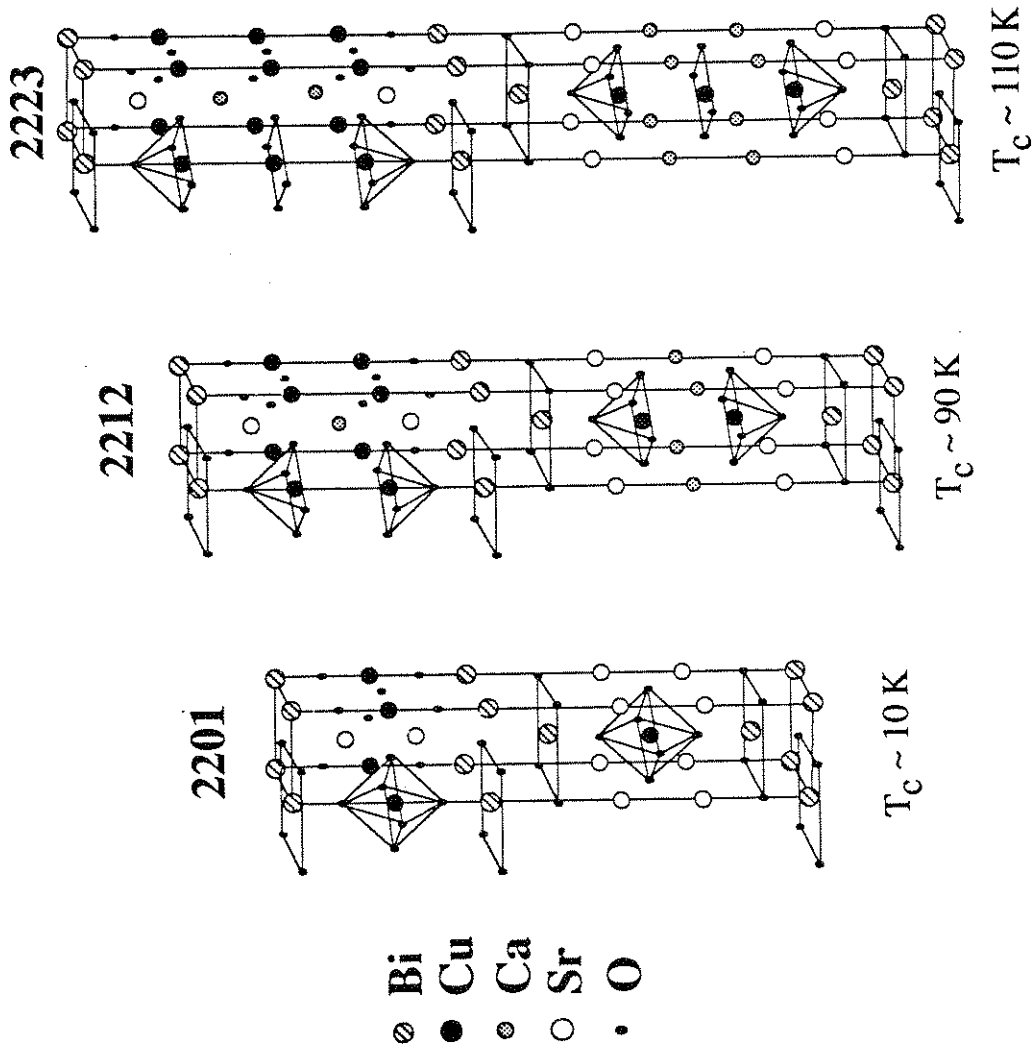

Figure 2.1 Crystal structures for the three members of the BSCCO family along with the associated superconducting transition temperatures.

$Bi_2Sr_2CuO_x$ A_{mma} [C_{ccm}, No. 66] a ≈ 5.36 Å b ≈ 5.37 Å c ≈ 24.62 Å

Atoms	Site	x	y	z
Bi	(8l)	0	0.2758	0.0660
Sr	(8l)	0.5	0.2479	0.1790
Cu	(4e)	0.5	0.75	0.25
O1	(8h)	0.75	0.5	0.246
O2	(8l)	0	0.226	0.145
O3	(8l)	0.5	0.334	0.064

$Bi_2Sr_2CaCu_2O_x$ F_{mmm} a ≈ b ≈ 5.4 Å c ≈ 30.9 Å

Atoms	Site	x	y	z
Bi	(8i)	0	0	0.20
Sr	(8i)	0	0.5	0.11
Ca	(4b)	0	0.5	0
Cu	(8i)	0	0	0.05
O1	(16j)	0.25	0.25	0.05
O2	(8i)	0	0.5	0.20
O3	(8i)	0	0	0.13

$Bi_2Sr_2Ca_2Cu_3O_x$ $I_{4/mmm}$ a ≈ b ≈ 0.38 Å c ≈ 37.1 Å

Atoms	Site	x	y	z
Bi	(4e)	0	0	0.21
Sr	(4e)	0.5	0.5	0.16
Ca	(4e)	0.5	0.5	0.05
Cu	(2a)	0	0	0
Cu	(4e)	0	0	0.11
O1	(4c)	0	0.5	0
O2	(8g)	0	0.5	0.11
O3	(4e)	0	0	0.16
O4	(4e)	0.5	0.5	0.21

Table 2.1 Crystal structure of the three members of the BSCCO family using the standard Wyckoff notation. Data obtain from ref. [22]

Large (1mm x 1mm x 0.01mm) single crystals of the Bi-2212 compound can easily be synthesized.[25] Unfortunately the idealized forms of Bi-2201 and Bi-2223 have not yet been isolated but can only be detected as constituent phases in a mixed phase compound. One can synthesize single phase polycrystalline samples by substitutionally doping La for Sr in Bi-2201 and (Pb, Sb) for Bi in Bi-2223.[26] The resulting superconducting transition temperature is unaffected for Bi-2223 but is increased in Bi-2201 from ~10 K for the ideal structure to ~24 K for the La doped single phase samples. For the intercalation studies on Bi-2201 and Bi-2223 we used these substitutionally doped compounds with nominal compositions $Bi_{2.1}Sr_{1.5}La_{0.4}CuO_x$ and $Bi_{1.58}Pb_{0.32}Sb_{0.1}Sr_{1.75}Ca_{1.8}Cu_{2.75}O_x$ for Bi-2201 and Bi-2223, respectively.[26] Note that throughout the text these two compounds will be referred to by their idealized stoichiometry.

Chapter 3

Iodine Intercalation of BSCCO

3.1 Preparation

One class of common intercalants for graphite and the dichalcogenides is the alkali-metal group.[9] Attempts to intercalate similar guest species into the oxide superconductors did not yield positive results. For example, "intercalation" of K and Na into Bi-2212 crystals results in a drastic decrease in T_c and color change of the crystals, but no significant change in the lattice parameters. This suggests that K and Na act as oxygen getters instead of intercalants. Similar results are obtained for attempted Cu and Ag intercalation.[27] On the other hand, we have been successful in intercalating iodine into the entire BSCCO family which results in a dramatic change in the c-axis lattice constant.[28,29] The stage-1 compounds are air stable with a measurable decrease in T_c. Stage-2 iodine intercalated Bi-2212 has also been produced and the effect on T_c determined.[30] The effects of intercalation on the superconducting transition temperature and the normal state transport properties have helped to clarify the picture of superconductivity in the high T_c oxides.[31]

The first step in manufacturing I-BSCCO is to properly prepare the pristine BSCCO samples for intercalation. If the samples are too thick then it is very difficult to obtain high quality single-phase samples. Typical sample thickness should be $\leq 0.2 - 0.3$ mm with the best results found for samples less than 0.2 mm thick. The next step is to prepare a Pyrex tube by necking down the tube in two places (A and B) and sealing one end, see Fig. 3.1(a). The inner neck diameter must remain large enough to allow the samples and the iodine to pass through. The BSCCO samples are placed in the end of tube along with the iodine (approximately 5 to 10 times the volume of the BSCCO) and the system is pumped out through a cold trap as shown in Fig. 3.2(b) to a pressure of less than 50 mTorr. Note that the cold trap is necessary to prevent the iodine from

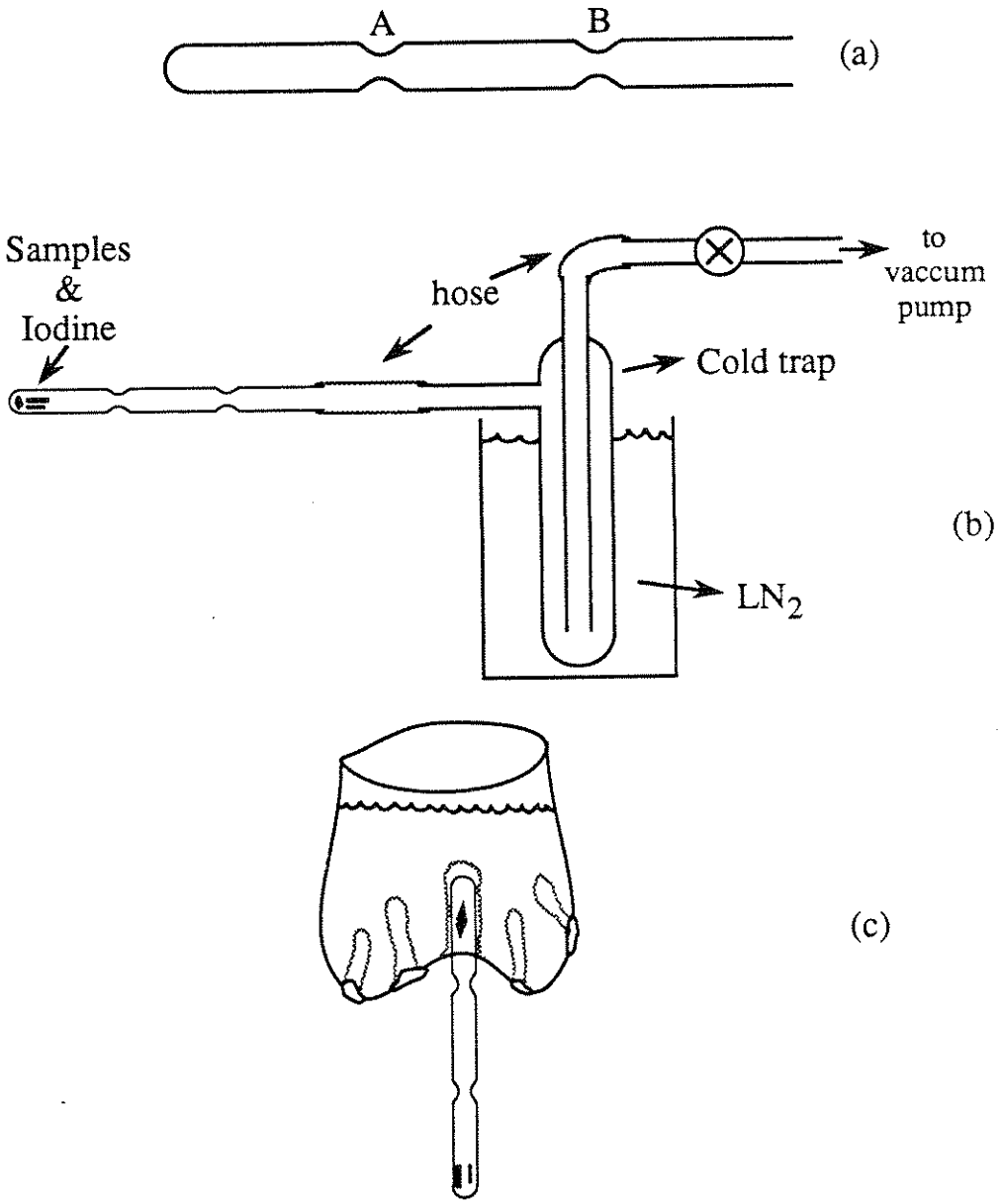

Figure 3:1 Apparatus required for intercalation of iodine into BSCCO. (a) Pyrex intercalation tube necked down at two places A and B. (b) Pumping configuration. (c) Inverted rubber glove filled with LN_2 used to separate iodine from samples.

reaching the pump and being dispersed into the air. At this point the tube is sealed at the second neck B.

To avoid having the samples immersed in the liquid iodine when the tube is heated it is necessary to separate the iodine to the other end of the tube. The easiest way to achieve this is to stand the tube on end as in Fig. 3.1(c) and place an inverted rubber glove over the top of the tube. Fill the glove with LN_2 and heat the other end of the tube. Using this technique all of the iodine can be condensed to the top end of the tube. Therefore, when the tube is placed in the furnace and heated (in a horizontal orientation) the majority of the excess iodine will liquefy on one side of the neck, A, and the samples, being on the other side of the neck, will be exposed mainly to iodine vapor.

For making the stage-1 compounds the tube should be placed in a uniform temperature oven with $T \approx 130$ °C for a period of 7 to 10 days. For temperatures less than 100 °C and times less than five days the resulting materials are mixtures of stage-1 and pristine materials. The limit of 10 days is not strict since samples which were intercalated over a period of 20 days show the same structure indicating that the resulting compound is a saturated phase. To produce majority phase stage-2 compounds one needs to use the true two-zone technique. The iodine side should be maintained at a temperature of $T \approx 130$-150°C while the sample end should be heated to $T \approx 300$-320 °C, for a period of 14 days. To remove the samples the iodine end of the tube is cooled with LN_2 (while the sample side remains in the furnace) to quickly condense the iodine away from the samples. The tube is then removed from the furnace and broken open and the samples removed. Unlike most graphite intercalation compounds, the iodine-intercalated oxide superconductors are stable in air, which greatly simplifies characterization of the physical properties.

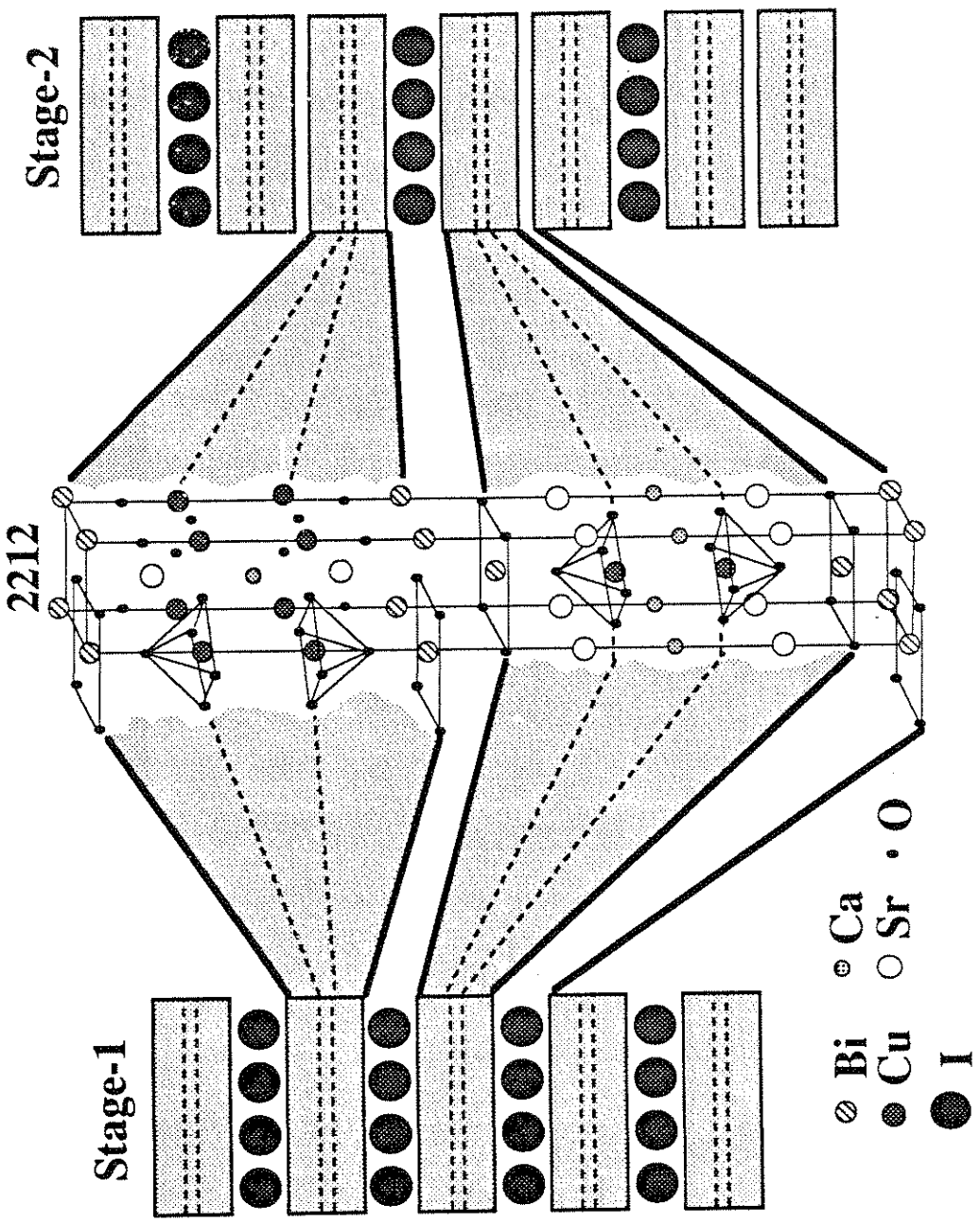

Figure 3.2 Schematic of the intercalation of Bi-2212 with iodine for both the stage-1 and the stage-2 compounds. The iodine intercalates between the weakly bonded BiO bilayers as shown. The shaded regions represent the strongly bonded main structural units of the host and the dashed lines represent the CuO_2 layers.

3.2 Structure

After intercalation, inspection of the samples shows three different looking surfaces. A few of the samples have surfaces which are dull in color which is assumed to be the result of iodine which has condensed and subsequently reacted with the air. Most samples, however, have shiny surfaces very similar to the original BSCCO. Careful inspection of these surfaces indicates that some of them have various striations of a purple or blue color. This is also believed to be iodine, however in much smaller and hence thinner quantities. Intercalated BSCCO retains the micaceous morphology found in the original pristine host indicating that the bonding between the iodine and the surrounding BiO bilayers is weaker that between any other layers. This is of course consistent with the structural analysis below which shows that the spacing between the iodine and the BiO layers is still quite large compared to any other lattice spacing.

Most of the detailed structural analysis has been performed on the intercalated Bi-2212 material; however powder x-ray diffraction patterns and some TEM work confirm essentially the identical results for the other members of the BSCCO family (Bi-2201 and Bi-2223). Therefore, the structural analysis that follows will deal primarily with IBi-2212 and differences in the other members will be addressed where necessary. Fig. 3.2 shows a schematic of the effect of intercalation on the Bi-2212 structure for both the stage-1 and stage-2 materials.

3.2.1 Stage-1

The stage-1 compound was the first to be produced as a single phase. The initial determination of iodine content was made using weight measurements and scanning-electron-microscope x-ray fluorescence indicating a 1:2 ratio of I : Bi. To determine if the incorporation of iodine was an "intercalation" process x-ray diffraction studies were performed.

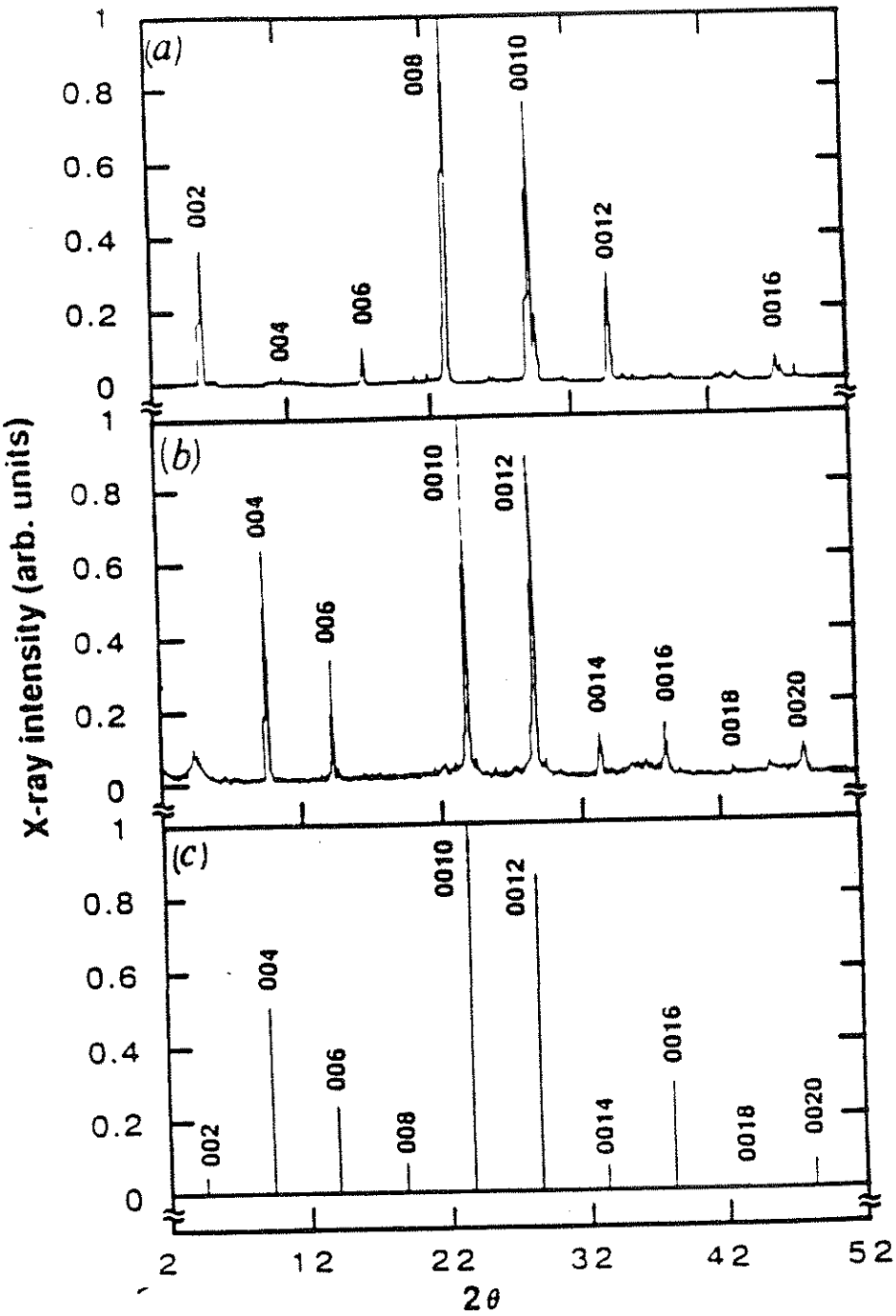

Figure 3.3 Highly oriented crystal x-ray diffraction patterns of (a) pristine $Bi_2Sr_2CaCu_2O_x$ and (b) $IBi_2Sr_2CaCu_2O_x$. (c) Predicted diffraction pattern of $IBi_2Sr_2CaCu_2O_x$ assuming that the iodine is intercalated between the BiO bilayers.

The x-ray diffraction patterns of highly oriented (along the c-axis) crystals of Bi-2212 and IBi-2212 are shown in Fig. 3.3 (a) and (b), respectively. The c-axis unit cell dimension for the pristine material is 30.65 Å, whereas that for IBi-2212 is 37.78 Å, corresponding to an increase of ~7.1 Å, or 23%. The IBi-2212 material is stage-1 and single phase to a resolution of better than 1% determined by the lack of pristine or other phase diffraction peaks.

In order to be able to analyze the observed x-ray diffraction patterns I wrote a computer program for the Macintosh computer which allows the user to enter an arbitrarily composed unit cell of a layered material and the program would utilize the known structure factors for the constituent elements and generate the expected x-ray diffraction pattern (either (00l) only or all (hkl) peaks). Although not as robust as doing a full Rietveld analysis, this program made it possible to quickly determine the expected x-ray diffraction patterns for a given structure. The program was tested by comparing the output with x-ray diffraction patterns of known materials like pristine BSCCO.

For each unit cell of host Bi-2212 there are two intercalated layers of iodine; each iodine layer expands the c-axis by ~3.6 Å. To determine whether the intercalated layer lies between the BiO planes or between the CuO_2 planes, we calculated the expected relative x-ray scattering intensities for both possibilities. We obtained good agreement between the predicted and experimental intensities by assuming that the iodine layer is between the weakly bound BiO bilayers. Fig. 3.3(c) shows the calculated intensity for this configuration; the results should be compared to the experimental data in Fig. 3.3(b). The small discrepancies can be accounted for by the fact that a somewhat idealized layered host structure was used, in particular, no fine tuning of the oxygen positions out of the layers or changes in the intra-host layer to layer separations were incorporated. Also, to insure that the intercalation was a true bulk effect an intercalated sample was multiply cleaved and each section was examined with an x-ray diffractometer. The data

for each section was consistent with the intercalated structure and showed no trace of the pristine phase.

In addition to the highly oriented configuration, x-ray diffraction patterns were also taken for powder samples which showed all (hkℓ) peaks. The stability of the positions of the (hk0) peaks upon intercalation indicates that the in-plane lattice spacing of the building blocks of the host structure is not disturbed by the intercalants. The (hkℓ) peaks can only be indexed if we assume the BiO layer stacking sequence of AB...BA...A in the pristine material is changed upon intercalation to a stacking sequence A/A...A/A...A. A and B refer to BiO layers with $\frac{1}{2}$ $\hat{\mathbf{a}}$ shift with respect to each other, the dotted line ... refers to the rest of the elements in the basic building block, and "/" refers to the iodine layer. This assumption is also consistent with x-ray diffraction computer simulations. A similar change in the stacking sequence is commonly observed in graphite and the dichalcogenide intercalation compounds. Because of preferred crystallite orientation in the diffraction specimens, enhancement of the (00ℓ) peaks with respect to the (hkℓ) peaks is observed in the powder diffraction patterns and therefore it is difficult to determine the exact position of iodine atoms in the **ab**-plane.

To unambiguously determine the locations of the "guest" iodine species in the intercalated structure, crystals of pristine Bi-2212 and intercalated IBi-2212 were ion milled and examined in the JEOL JEM ARM-1000 atomic resolution microscope using a through-focus series of phase contrast images.[32,33] This transmission electron microscopy method derives sufficient contrast to directly image the heavier cations, but not the lighter oxygen atoms. Fig. 3.4(a) shows the atomic resolution image of pristine Bi-2212, viewed along the [110] direction. Note that from this viewing angle, the Bi atoms in adjacent Bi-O layers (identified by horizontal arrows) are staggered. Fig. 3.4 (b) and (c) are the atomic resolution image of IBi-2212 viewed along the [110] and [100] directions, respectively. These images clearly show an expansion of the Bi-O bilayers

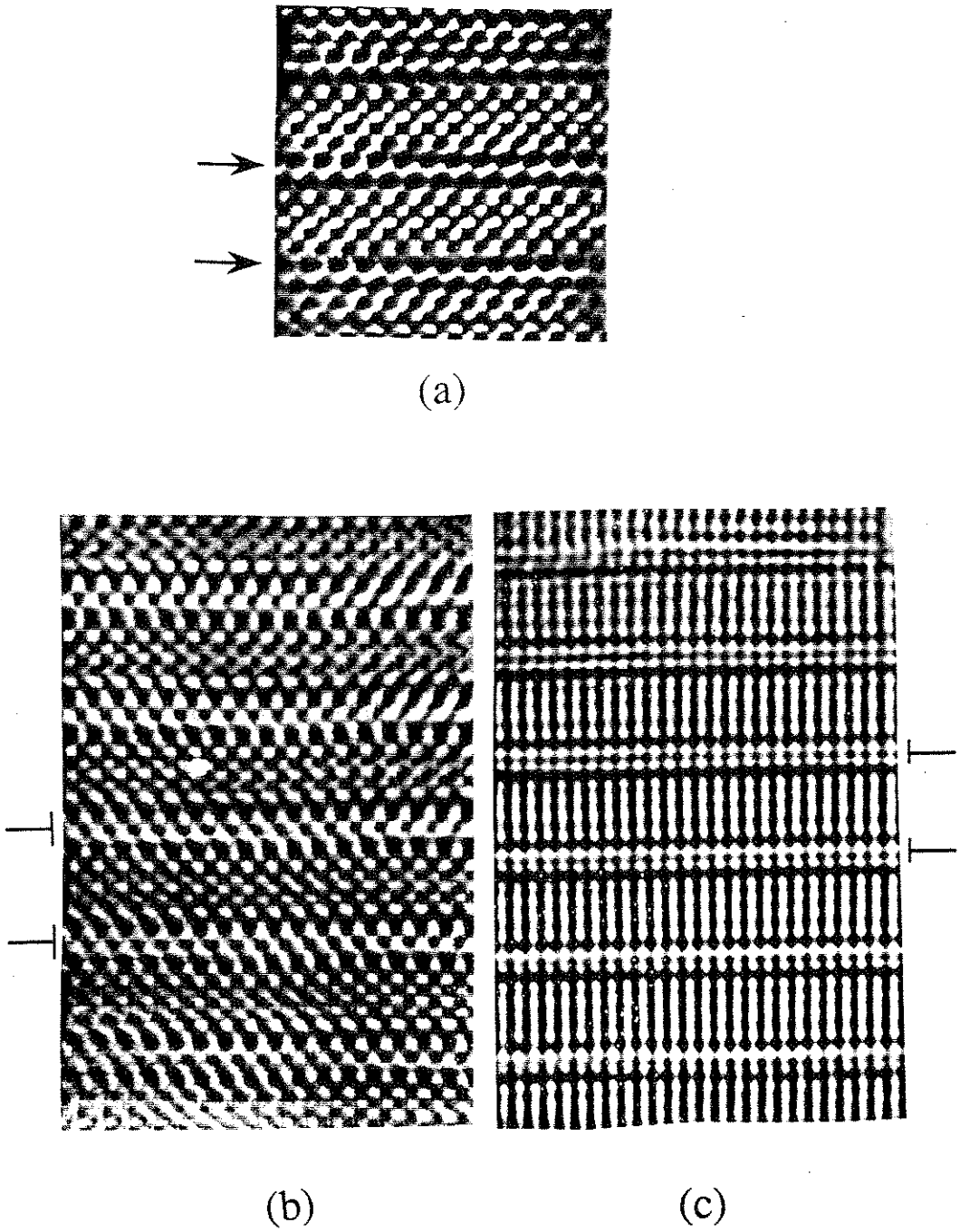

Figure 3.4 Processed phase contrast high-resolution electron microscope image of (a) pristine $Bi_2Sr_2CaCu_2O_x$ and (b) & (c) the stage-1 iodine-intercalated superconductor $IBi_2Sr_2CaCu_2O_x$. The incident electron beam is along the (a) [110], (b) [110] and (c) [010] directions. An arrow identifies a pristine BiO bilayer and a bar identifies an intercalated layer.

and the positions of the iodine atoms intercalated between the Bi-O bilayers (intercalated layers identified by bar). In addition, intercalation shifts adjacent CuO_2 plane-containing blocks into common registry, thereby removing the staggered Bi sequence observed in pristine Bi-2212. As a consequence, the stage-1 material has a c-axis lattice constant which is *smaller* than in pristine Bi-2212 since it requires only a single building block of the host structure in addition to the iodine layer to form a unit cell, whereas the pristine material requires two building blocks due to the staggering of the BiO bilayers. Comparison between images recorded under [010] and [100] directions demonstrate that the iodine is located between the oxygen atoms in the sandwiching layers; therefore, the iodine is epitaxially intercalated. Although only a few atomic layers are shown in Fig. 3.4(c), the actual micrographs cover much larger areas (>1000 Å), and confirm that long range iodine order persists, consistent with x-ray studies. These images also confirm that the intercalation of iodine does not alter intra-block lattice parameters nor does it affect the b*-axis lattice modulation observed in the pristine host material.[32]

3.2.2 Stage-2

Stage-2 iodine intercalated regions were indicated as a minority phase using x-ray diffraction on samples that had been intercalated in a *uniform* temperature oven with T ≈ 300 °C for 10 days. Subsequently this phase was isolated using the technique described in section 3.1 yielding samples which are nearly phase-pure stage-2 with minority phases of stage-3 and stage-4 also present. High resolution TEM images were obtain for this material, see Fig. 3.5, which clearly show the iodine epitaxially intercalated into every other BiO bilayer. Again the arrow identifies a pristine BiO bilayer and a bar identifies an intercalated layer. Each intercalated iodine layer expands the lattice by 3.6 Å as observed in the stage-1 material. Also, the presence of iodine again changes the stacking sequence (between adjacent BiO bilayers) to a commonly registered stacking sequence. In

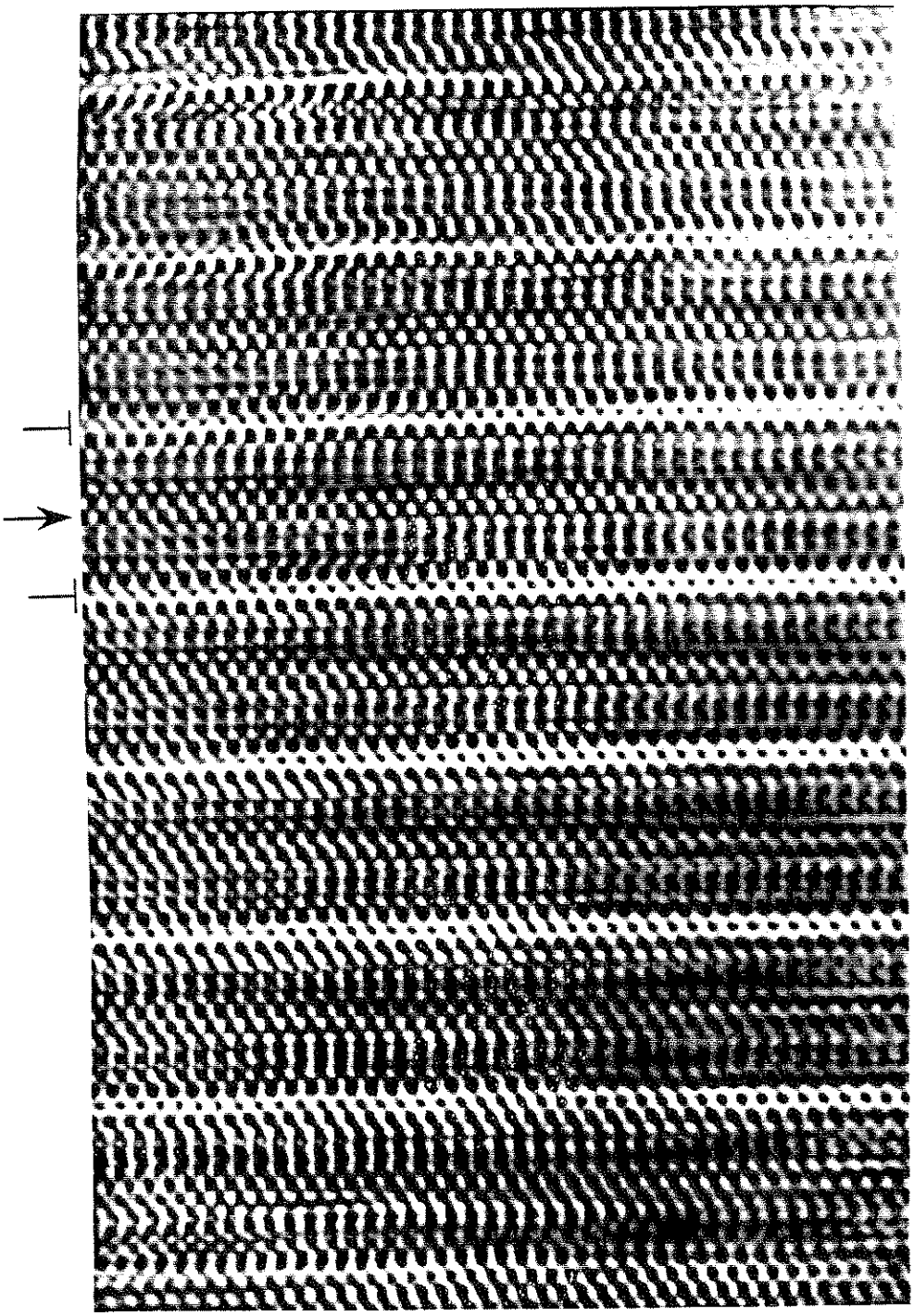

Figure 3.5 Processed phase contrast high-resolution electron microscope image of the stage-2 iodine-intercalated superconductor $IBi_4Sr_4Ca_2Cu_4O_x$. The arrow identifies a pristine BiO bilayer and a bar identifies an intercalated layer. Note the shifted registry in the unintercalated BiO bilayers.

particular, the stacking sequence AB...BA...AB relevant to pristine Bi-2212 changes in the stage-2 compound to AB...B/B...BA...A/A...AB. Here again, A and B represent BiO layers shifted by ½ **â** with respect to each other, the dotted lines represent the other elements inside the block, and the "/" represents the iodine intercalant. Note that this implies that the **c**-axis lattice parameter is significantly larger than in the pristine or stage-1 materials since it must include four building blocks of the pristine material in addition to the iodine layers to form the unit cell.

3.2.3 Higher stages

Higher stages have been identified (using high resolution TEM) as minority phases present in the predominately stage-2 materials.[34] A significant number (≥ 5) of repeated units of stage-3 have been observed, however regions with a stage index up to 20 have also been imaged. At present all attempts to isolate these higher stages as majority phases have not been successful.

Table 3.1 is a summary of the lattice constants (Å), space groups, and distances (Å) between the adjacent cation layers in the iodine intercalated BSCCO family. All of these data have been obtained using the results of the high resolution TEM work except for the case of Bi-2201. The results for Bi-2201 were obtained from powder x-ray diffraction studies only. Also recall that the identification of Bi-2201 and Bi-2223 is ideal since the actual material contains various dopants in order to isolate the desired host structure phase, (see section 2.2.1).

	Pristine $Bi_2Sr_2CaCu_2O_x$	Stage-I $IBi_2Sr_2CaCu_2O_x$	Stage-II $IBi_4Sr_4Ca_2Cu_4O_x$	Stage-III $IBi_6Sr_6Ca_3Cu_6O_x$	Stage-n $IBi_{2n}Sr_{2n}Ca_nCu_{2n}O_x$
a	5.4	5.4	5.4	5.4	5.4
b	5.4	5.4	5.4	5.4	5.4
c	30.6	18.9	68.5	49.4	$m(3.6 + 15.3n)$ $m = 1$ when n is even $m = 2$ when n is odd

Space group	B_{bmb}	P_{ma2}	B_{bmb}	P_{ma2}	P_{ma2} when n is odd B_{bmb} when n is even
I-Bi	-	3.31	3.40	3.40	3.40
Bi-(I)-Bi	3.24	6.62	6.80	6.80	6.80
Bi-Sr	2.70	2.80	2.70	2.70	2.70
Sr-Cu	1.70	1.70	1.70	1.70	1.70
Cu-Ca	1.65	1.65	1.65	1.65	1.65

	Pristine $Bi_2Sr_2CuO_x$	Stage-I $IBi_2Sr_2CuO_x$	Pristine $Bi_2Sr_2Ca_2Cu_3O_x$	Stage-I $IBi_2Sr_2Ca_2Cu_3O_x$
a	5.4	5.4	5.4	5.4
b	5.4	5.4	5.4	5.4
c	24.2	15.8	36.9	22.0

Table 3.1 Comparison of the lattice parameters (Å), space groups and distances (Å) between adjacent cation layers in the host superconducting BSCCO and the iodine-intercalated superconductors. The distances between the layers are defined using the **c** coordinates of the cations.

3.3 Current status

Since the discovery[28] that iodine could be successfully intercalated into the BSCCO host structure yielding high-quality phase-pure stage-1 compounds numerous groups have successfully repeated the intercalation process with iodine and have made some progress in intercalating other "guest" species into the oxide superconductors. This section is meant to be a brief overview of the current status of intercalants that have been tried and in some cases been successfully intercalated into the BSCCO structure. Several groups[35-38] have been pursuing electrochemical intercalation of the alkali-metals into BSCCO. One group also reported more work on electrochemical intercalation of Cu.[39,40] Grigoryan *et al.* have done a considerable amount of work[41-45] attempting to intercalate ring-shaped organic molecules like benzene and the metal-phthalocyanines into BSCCO but at present they have not been successful in obtaining uniform phase materials. Numerous groups have been pursuing other halogens besides iodine. Evidence has been reported[40,46,47] for the successful intercalation of Br into BSCCO but the resulting material is unstable in air and can not be made phase pure since the reactivity of Br makes the samples too fragile for concentrations $x \geq 0.3$, where x is defined by $Br_xBi_2Sr_2CaCu_2O_\delta$. Recently, Mochida *et al.* reported[39] the successful intercalation of the combination of IBr with a lattice constant expansion only slightly larger than that found for Br alone. And finally there is a report[48] on some very exciting work by Kumakura *et al.* where they show extremely clean x-ray diffraction data indicating the successful intercalation of AgI_2 into Bi-2212 with a resulting increase in the lattice constant of more than twice that found in the IBi-2212 system. The intercalated oxide superconductors have become a growing sub-field in high T_c research and it shows the promise of not only generating new novel materials but it also can shed some light on the poorly understood mechanism of superconductivity in these materials.

Chapter 4

Intercalation and T_c

4.1 Stage-1 I-BSCCO series

One of the goals of this project was to examine the changes in the physical properties of the oxide superconductors as the crystal structure is modified via intercalation. In particular, intercalation provides a controllable means of investigating the mechanism responsible for high-T_c superconductivity, in addition to the possibility of improving the superconducting properties of the pristine materials, and developing new high-T_c superconductors and superconducting devices. Therefore, one of the first studies performed on these new iodine intercalated BSCCO materials was the examination of T_c and its dependence on the intercalation process. This study naturally divides into two parts; How does T_c change for the different members of the BSCCO family on the intercalation of iodine and what effect does stage index have on the superconducting properties of a particular member of the family? The first of these questions will be addressed in this section and the second will be addressed in the following section.

The transition temperature was determined in these samples using one of three standard techniques. The first, and easiest and quickest by far, was to measure the ac susceptibility using a homemade rf resonant magnetometer described below. The second method employed was to measure the dc susceptibility using a Quantum Designs dc superconducting quantum interference device (SQUID) magnetometer. This method was particularly well suited for measuring the polycrystalline samples of the pristine and intercalated Bi-2201 and Bi-2223 materials. Finally, the temperature dependence of the resistivity of single crystals of Bi-2212 and IBi-2212 was also measured and is described in more detail in Chapter 5.

The basis of the determination of T_c for a superconductor using susceptibility measurements is either the Meissner effect or the shielding effect depending on the experimental arrangement. The shielding effect is typically measured by cooling the sample in zero magnetic field to well below the transition temperature and then turning on a small uniform dc magnetic field and measuring the magnetization while the sample is warmed back up through the transition temperature into the normal state. This is commonly referred to as a zero-field-cooled (ZFC) technique. From Maxwell's equations, the response to the magnetic field for a perfect conductor is given by

$$\nabla^2 \mathbf{B} = \frac{1}{\lambda_L} \dot{\mathbf{B}} \tag{4.1}$$

where λ_L is the London penetration depth. Therefore, since the initial flux was zero this implies that the system will generate shielding currents to prevent the flux from changing, i.e., as the flux will be **excluded** from the sample. On the other hand, the response to a magnetic field for a superconductor is determined from the "second London equation" which, in the London gauge, is given by[49]

$$\mathbf{J} = -\frac{c}{4\pi\lambda_L} \mathbf{A} \tag{4.2}$$

from which it follows that

$$\nabla^2 \mathbf{B} = \frac{1}{\lambda_L} \mathbf{B} \tag{4.3}$$

This equation accounts for the Meissner effect which states that for small magnetic fields no flux will penetrate into a superconductor beyond a skin-depth given by λ_L whether or not there was a field present before the sample became superconducting. In contrast to

the shielding effect, this corresponds to an **expulsion** of the flux from the sample. To measure the Meissner effect one first turns on a small uniform dc magnetic field when the sample is in the normal state well above the transition temperature, then the magnetization is measured as the sample is cooled down through the superconducting transition. This is commonly referred to as the field-cooled (FC) technique. For samples much larger that the penetration depth, the entire flux should be expelled and therefore the measured dc susceptibility should be $\chi_{ac} = \mathbf{M}_{fc}/\mathbf{H} = -1/4\pi$. It is useful to define the "Meissner fraction" as $-4\pi\mathbf{M}_{fc}/\mathbf{H}$, where **H** is the internal field (the applied field corrected for shape demagnetization[49]). It is worth emphasizing that the Meissner fraction and not the size of the ZFC susceptibility, or, by extension, of the ac susceptibility, is the better measure of the true volume fraction of superconducting material. The reason being that for the ZFC case only the surface of the sample need be superconducting in order for the flux to be excluded from the entire volume. On the other hand, the Meissner effect generally underestimates the actual volume fraction, especially in the high T_c oxides, because of the incomplete flux expulsion due to flux pinning.

Measurements of the ac susceptibility were performed using a homemade rf resonating magnetometer operating at ~10 MHz. A schematic of the resonating circuit and the electronics is shown in Fig. 4.1. The basic concept behind the device is as follows: Neglecting the resistance of the wires for now, the resonant frequency of a parallel inductor-capacitor circuit is given by $\omega^2 \approx 1/LC$, where L is the self-inductance of the coil and C is the capacitance of the parallel capacitor. The self-inductance is related to the amount of flux linkage through the inductor due to current flowing in the inductor. The sample is placed on top of the coil and is held in place with a small amount of mineral oil. The size of the sample must be comparable to the size of the coil. Well above the transition temperature the presence of the sample has little or no effect on the amount of flux linking the inductor and hence the resonant frequency is essentially independent of

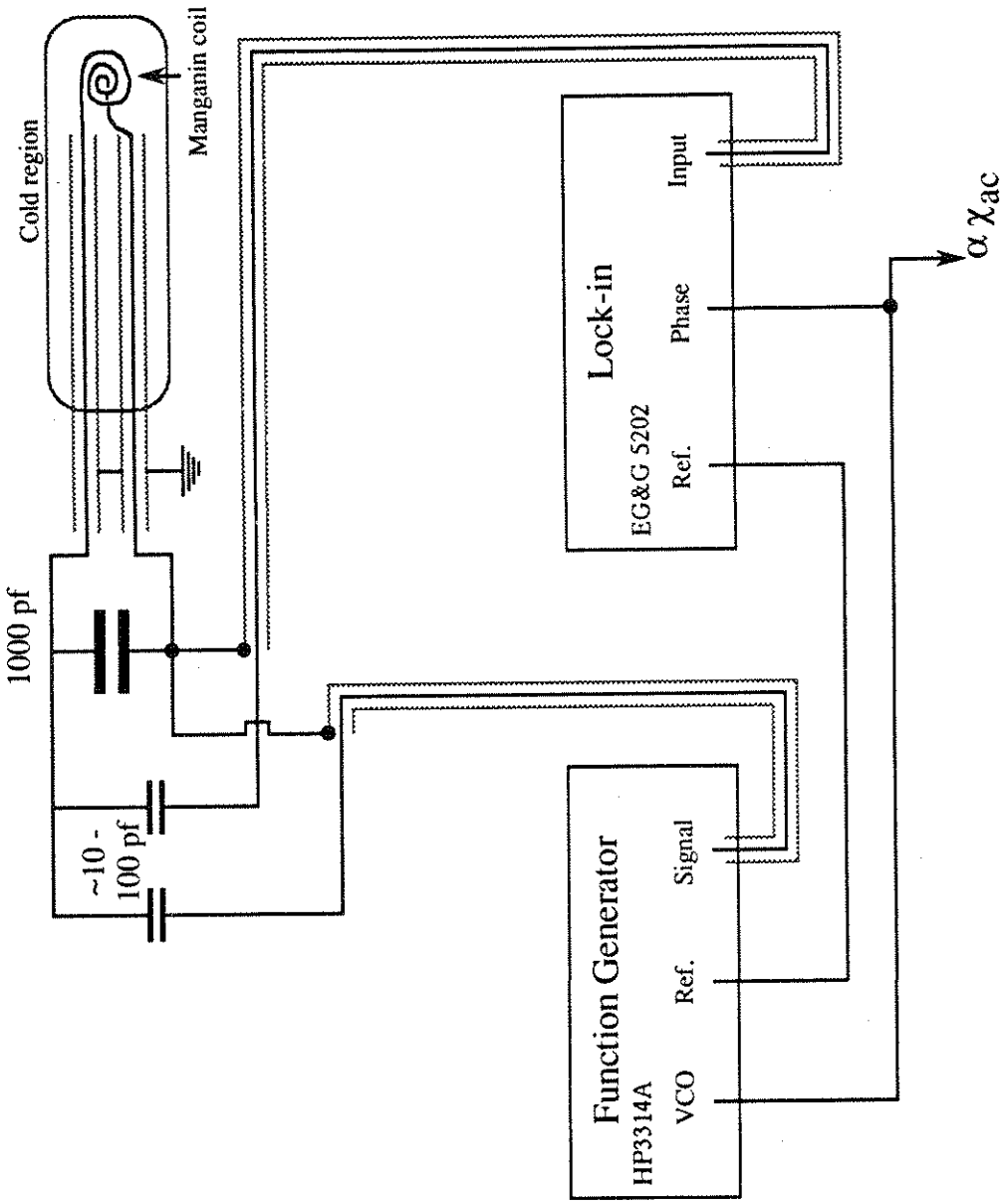

Figure 4.1 Schematic for the homemade rf resonant magnetometer used to determine the superconducting transition temperature. The capacitor values are shown. The sample is placed on top of the manganin coil. This feedback loop maintains the frequency at the resonance frequency as the inductance of the coil changes when the sample goes superconducting. The output of the lock-in is the measured signal.

temperature. When the sample goes superconducting it excludes the flux from penetrating it. Since the sample covers a reasonably large area of the coil and is sitting immediately on top of the coil, this flux exclusion will necessarily reduce the flux through the coil. Thus, the self-inductance of the coil changes which then is detectable as a change in the resonant frequency of the LC circuit. Since all changes are small (typical $\Delta f \approx 1\%$) the change in resonant frequency is roughly proportional to the ac susceptibility, χ_{ac}. Obviously, this technique can not yield the actual magnitude of χ_{ac}; however it works quite well in determining the transition temperature when compared to other techniques like using a dc SQUID magnetometer or measuring the resistive transition.

The details of the typical values used for the capacitors and inductor are shown in Fig. 4.1. The coil itself is wound from manganin wire (for reasons discussed below) and consists of 3-4 concentric turns in a planer geometry with the outer turn diameter ≈ 3 mm. A simple calculation of the self-inductance of this geometry yields $L \approx 1 \times 10^{-9}$ H which is consistent with the value of the resonant capacitor ≈ 1000 pF and a resonant frequency of about 10 MHz. Notice that the two 10~100 pF capacitors serve only as decoupling capacitors. A feedback loop using an EG&G 5202 lock-in amplifier (0.1 - 50 MHz) and an HP3314A Function Generator with a voltage-controlled-oscillator (VCO) input are used to track the resonant frequency. The tracking circuitry is based on the idea that when a resonant circuit is driven slightly off resonant the signal generated across the circuit will have a phase shift relative to the drive signal. That phase difference is detected by the lock-in which then outputs an amplified voltage proportional to the phase difference. This output is then fed into the VCO input of the frequency generator which adjusts the output frequency thereby completing the feedback loop. In principle the gain on the signal coming out of the lock-in should be as large as possible so as to keep the drive frequency nearly identical to the resonant frequency, however merely using the x10

gain available on the phase quadrature output on the EG&G lock-in proved sufficient for the feedback loop. Another factor affecting the sensitivity of the circuit to a changing resonant frequency is the Q of the circuit which is dependent on the resistive losses and is typically on the order of 10 ~ 20 for the set-up shown in Fig. 4.1. This dependence on the net resistance is the reason for using manganin wire for the inductor coil. First, manganin wire has a relatively high resistance compared to the copper wire used in the rest of the circuit and therefore the resistance of the coil dominates the resistance of the circuit. Second, the resistance of manganin is nearly independent of temperature so the Q of the circuit remains roughly constant from room temperature down to liquid helium temperatures.

This circuit was mounted on a probe which was designed to fit into a homemade helium gas-flow cryogenic system. Cold helium gas passes out of the dewer in a thermally insulated tube and flows over a copper head inside of which is mounted the inducting coil. Semi-rigid coaxial cables feed the signal out of cold region of the probe to a box (at room temperature) located about 10 inches away. Within this box are located the resonant and the decoupling capacitors shown in Fig. 4.1. With this system one can cool rapidly to just above T_c, wait several minutes for the system to thermally stabilize and then slowly change the temperature through the transition. Because of the small thermal masses involved it was possible to make several (> 5) measurements in a single day.

Fig. 4.2 shows the dc susceptibility (ZFC) of a pristine Bi-2201 specimen and the complementary stage-1 iodine intercalated sample as functions of temperature. The onset T_c of the intercalated compound is decreased by only 2 K with respect to T_c = 24 K for the (La doped) pristine material. Fig. 4.3(a) shows the ac susceptibility of a Bi-2212 single crystal before and after intercalation to stage-1. The onset T_c is 90 K for the pristine sample and 80 K for the sample after intercalation. The T_c of different pristine

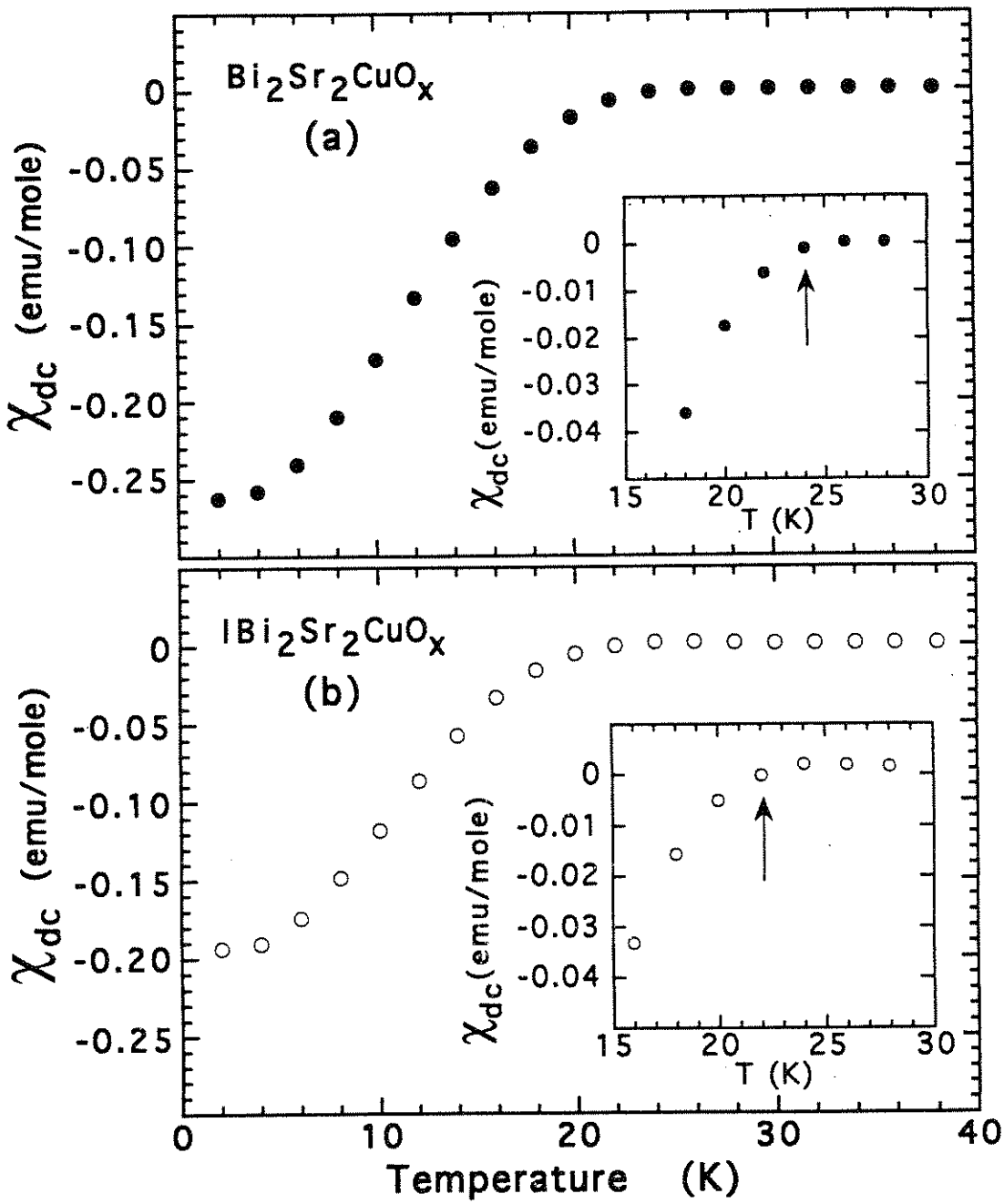

Figure 4.2 dc magnetic susceptibility (ZFC) of (a) pristine Bi-2201 and (b) intercalated IBi-2201 polycrystalline samples. The insets show detailed behavior near the onset critical temperature, identified by a vertical arrow.

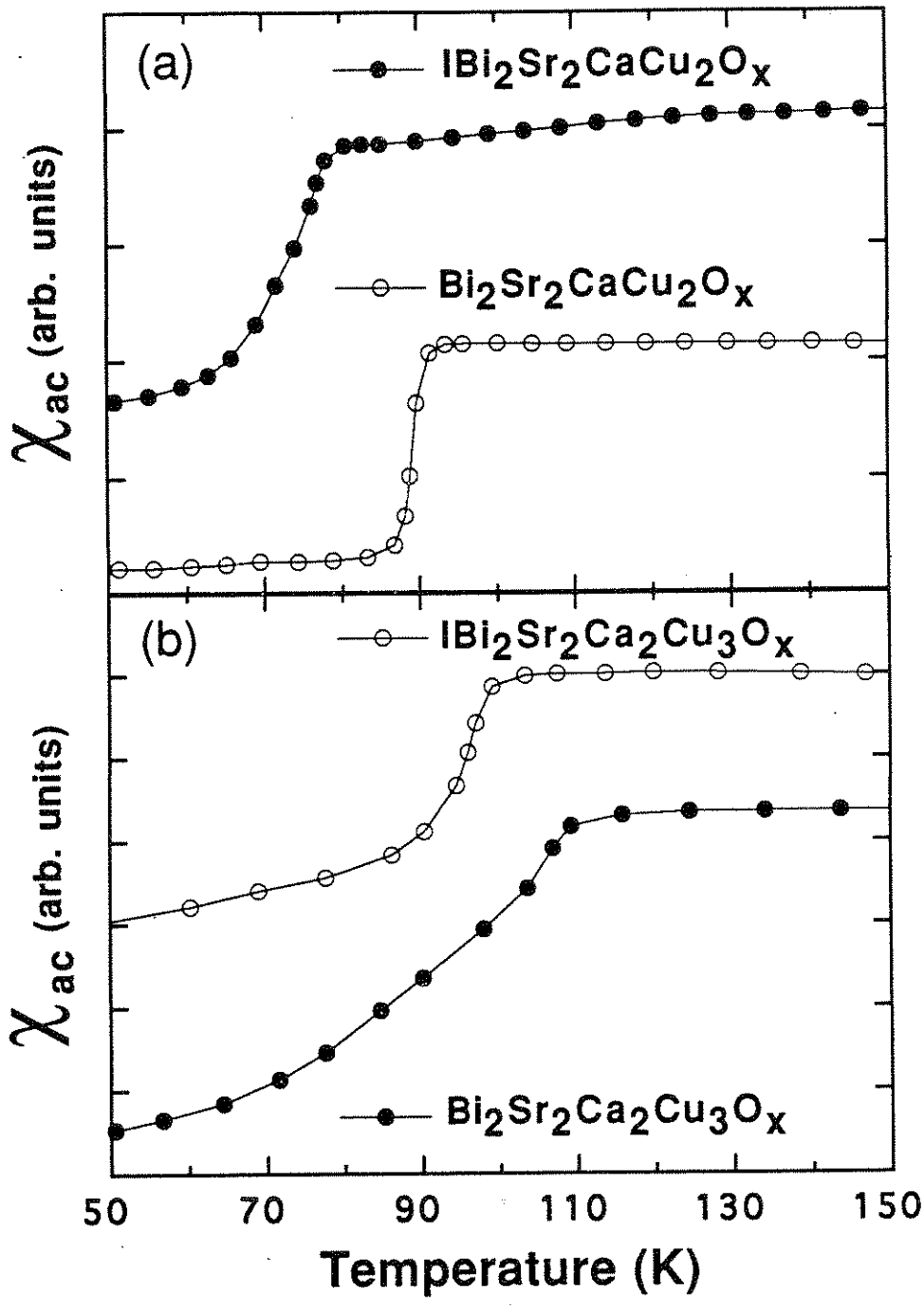

Figure 4.3 ac magnetic susceptibility of (a) pristine (open circles) and intercalated (solid circles) Bi-2212 single crystals; (b) pristine (open circles) and intercalated (solid circles) Bi-2223 polycrystalline samples.

Bi-2212 samples is somewhat dependent on the details of the crystal synthesis, ranging from 85 to 92 K. However the stage-1 intercalated IBi-2212 structure always has a T_c of 78 - 80 K. Fig. 4.3(b) shows the ac susceptibility of pristine Bi-2223 and a stage-1 intercalated polycrystalline IBi-2223 sample. The T_c of the intercalated sample is depressed by ~10 K with respect to T_c = 110 K for the pristine sample. In all cases there is clear evidence that all three intercalated compounds are bulk superconductors with a Meissner fraction similar to that of the corresponding pristine compounds.

Since this intercalation technique involves maintaining the samples at ≈130°C for a long period of time (≈ 10 days) there is some question as to whether the observed reduction in T_c is due to this "annealing" process. To insure that the long term low temperature annealing technique did not affect T_c independent of the presence of iodine, pristine samples were sealed in an evacuated tube without iodine and exposed to the same temperature cycle. The transition temperature of these samples showed no noticeable change.

The intercalation of iodine into the BSCCO structure may have two effects on the host structure, both of which could in principle affect the transition temperature. The first is a modification of the inter-layer coupling of the CuO_2 sheets from one block of the host structure to the next. Several models in the high T_c oxides incorporate this type of coupling and therefore must anticipate the observed changes in the transition temperature upon iodine intercalation. A detail discussion of these types of models is given later in this chapter and in chapter 5-Electrical transport. The second mechanism, which is common for intercalated compounds, is charge transfer. It is well known[50] that varying the concentration of holes in the CuO_2 layers significantly affects the observed transition temperature. Because of the electron negativity of iodine one would expect that the presence of iodine would increase the hole concentration in the host structure. There is clear evidence that there is some charge transfer between the iodine and the adjacent BiO

bilayers. First, there is a significant shift in the x-ray-absorption near-edge structure[51] for the Bi L_3-edge in the iodine intercalated compound compared to the pristine material. Second, there is a dramatic change in the temperature dependence of the **c**-axis resistivity upon intercalation, going from semiconductor-like to metallic-like, indicative of a change in the transport characteristics across these weakly bonded BiO bilayers. (This effect will be discussed further in chapter 5.) What is not clear, however, is whether there is any significant charge transfer from the iodine to the important $\mathbf{CuO_2}$ layers. The literature is presently filled[30,31,51-55] with conflicting reports as to what extent this charge transfer exists and consequently how important it is to the observed changes in the transition temperature. One measurement we performed[31] was to determine if any change occurred in the in-plane resistivity, ρ_{ab}, of a single sample by measuring it before and after intercalation. Since the in-plane transport is dominated by conduction along the CuO_2 planes, any change in the number density of carriers should show up as a change in ρ_{ab}. This type of change in the in-plane conductivity can clearly be observed in the intercalation compounds of graphite. Of course in this case the intercalant is located immediately adjacent to the conducting graphite sheets. This is in contrast to the intercalated BSCCO case where the iodine is located several atomic layers away from the CuO_2 layers. We detected no change in the resistivity per CuO_2 sheet to within the experimental accuracy of ~1%. This experiment is also discussed in more detail in chapter 5.

By measuring the x-ray-absorption near-edge structure corresponding to the Cu K-edge, Liang *et al.* determined[51] that there was only a very small (0.03 holes per Cu) increase in the hole concentration. More importantly, Fujiwara *et al.* measured[52] the effect of hole doping in the iodine intercalated system by using the host structures $Bi_2Sr_2Ca_{1-x}Y_xCu_2O_8$ with differing values of x. Since the Y concentration directly affects the hole density in the CuO_2 layer, they were able to directly measure the T_c vs.

hole doping curve by using host samples with different values of x. This study showed that there may be a charge doping of about 0.025 holes per Cu, however, it also explicitly separates the effects of charge transfer and inter-layer coupling since if the change in T_c is simply a charge doping effect then for some concentration of x the original T_c value should be obtained. The results indicate that the majority of the change in T_c upon intercalation is due to the modification of the inter-layer coupling and only a small amount is related to hole doping. In addition, comparison of ΔT_c for IBi-2212 and IBi-2223 indicates that they are virtually the same which is also not in agreement with the hole doping hypothesis for the following reason. First, we note that the amount of charge transfer from the iodine to the CuO_2 planes is the same in both cases. This assumption is based on the observation that the local environment of the iodine is the same in both systems and the x-ray and TEM studies show that the lattice expansion upon intercalation is also identical. If charge doping where the sole cause for the depression in T_c then one would expect that the IBi-2223 system would show a noticeably smaller change in T_c since the same amount of holes doped in must now be shared among three CuO_2 sheets whereas for IBi-2212 these extra holes would be distributed over only two CuO_2 sheets. Given the current level of understanding, it appears as though charge doping to the CuO_2 layers can not be ruled out as having some affect on the transition temperature but it is unlikely that it is the dominant cause of the observed depression in T_c in the intercalated oxide superconductors. Therefore throughout the rest of this thesis it is assumed that the most important mechanism responsible for the observed changes in T_c is related to the effect that intercalation has on the inter-block coupling of the CuO_2 planes.

4.2 Tuning T_c via multistage intercalation

As discussed previously, compounds with stage index $n = 2$ have been isolated as a majority phase. Therefore, the ability of produce largely homogeneous stage-1 and

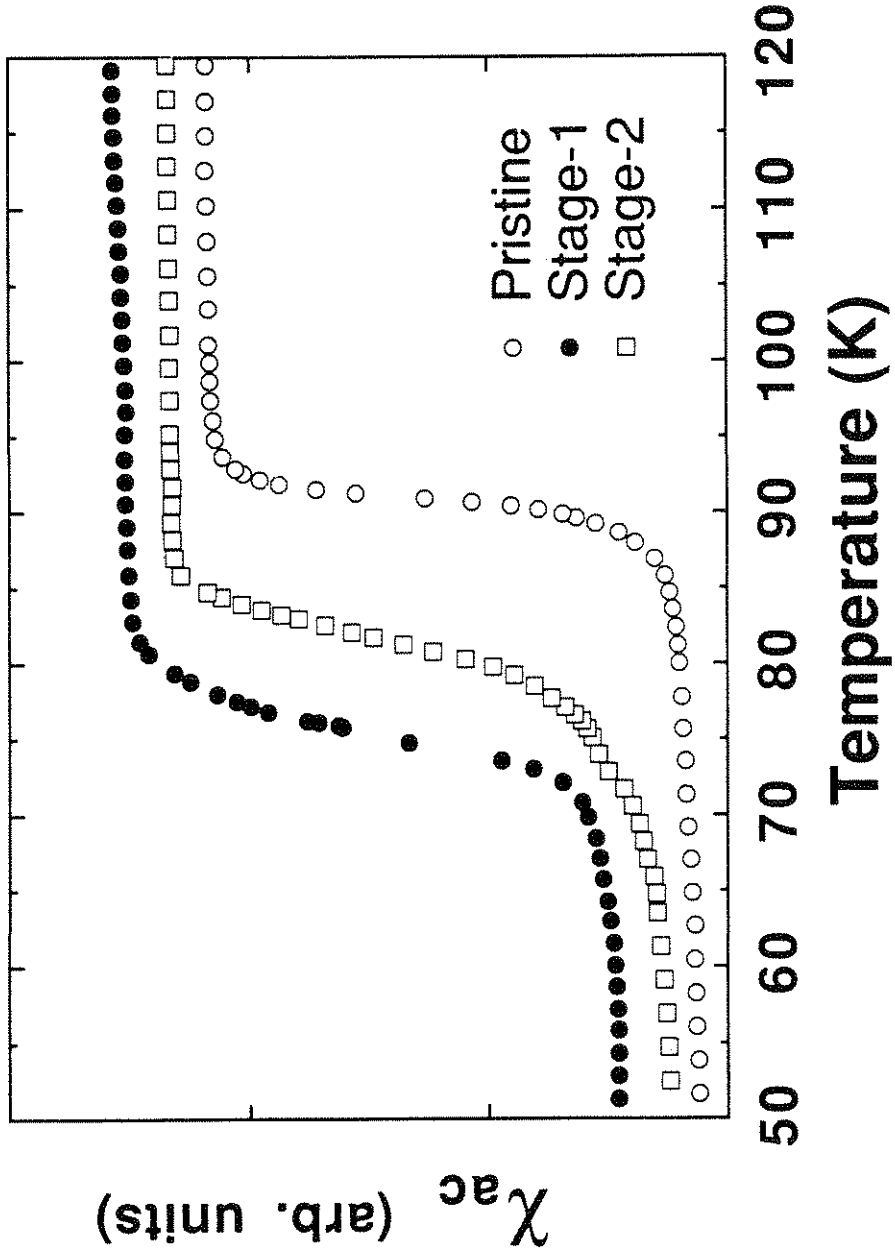

Figure 4.4 Plot of the ac magnetic susceptibility, χ_{ac}, of pristine (open circles), stage-1 (solid circles), and stage-2 (open squares) iodine-intercalated Bi-2212 as a function of temperature.

	Original T_c	Stage-1 T_c	ΔT_c	Stage-2 T_c	ΔT_c
2201	24	~22	~2	–	–
2212	~90	80	~10	85	~5
2223	~110	~100	~10	–	–

Table 4.1 Comparison of the superconducting transition temperatures (K) for all members of the BSCCO family as well as the stage-1 and stage-2 iodine intercalated BSCCO materials.

stage-2 compounds of I-BSCCO allows a direct comparison between structural and superconducting properties. Fig. 4.4 shows the ac susceptibility, χ_{ac}, as a function of temperature for pristine $Bi_2Sr_2CaCu_2O_x$, stage-1 $IBi_2Sr_2CaCu_2O_x$, and stage-2 $IBi_4Sr_4Ca_2Cu_4O_x$. Well-defined transitions to the superconducting state are clearly visible not only for the pristine and stage-1 material but also for the stage-2 compound. The T_c for the stage-2 $IBi_4Sr_4Ca_2Cu_4O_x$ is 85 K, corresponding to a ~5 K depression with respect to the pristine material.

Table 4.1 summarizes the effects of iodine intercalation on the BSCCO family. We see that the change in the transition temperature is dependent on both the member of the family involved, 2201, 2212, or 2223, and on the stage index with increasing stage index resulting in a smaller change. The shift in T_c for different intercalation stage structures can be used to estimate the size of the adjacent block coupling in pristine and intercalated BSCCO. We assume that intercalation reduces the interblock coupling due to an increase in the distance between the CuO_2-containing blocks. Stage-1 intercalation reduces the adjacent block coupling in both directions along the **c**-axis, while stage-2 intercalation preserves the original coupling in one direction for each block. Since ΔT_c for the stage-1 material is -10K while ΔT_c for the stage-2 material is only -5K, empirically it appears as if next-block coupling contributes about 5K to T_c for each neighboring block of pristine $Bi_2Sr_2CaCu_2O_x$. Here we examine two prototypical layering models, both of which are capable of explaining the behavior of T_c upon multi-stage intercalation. No specific microscopic mechanism is assumed, and the parameters in each model are determined here phenomenologically.

The simplest layer coupling model is one where T_c varies linearly with the interplane coupling. Each CuO_2 plane is coupled to its neighbors in the **c** direction, but intraplane coupling is neglected. Wheatley, Hsu and Anderson (WHA)[56] have used this type of model to discuss superconductivity due to spinon-holon scattering. Despite

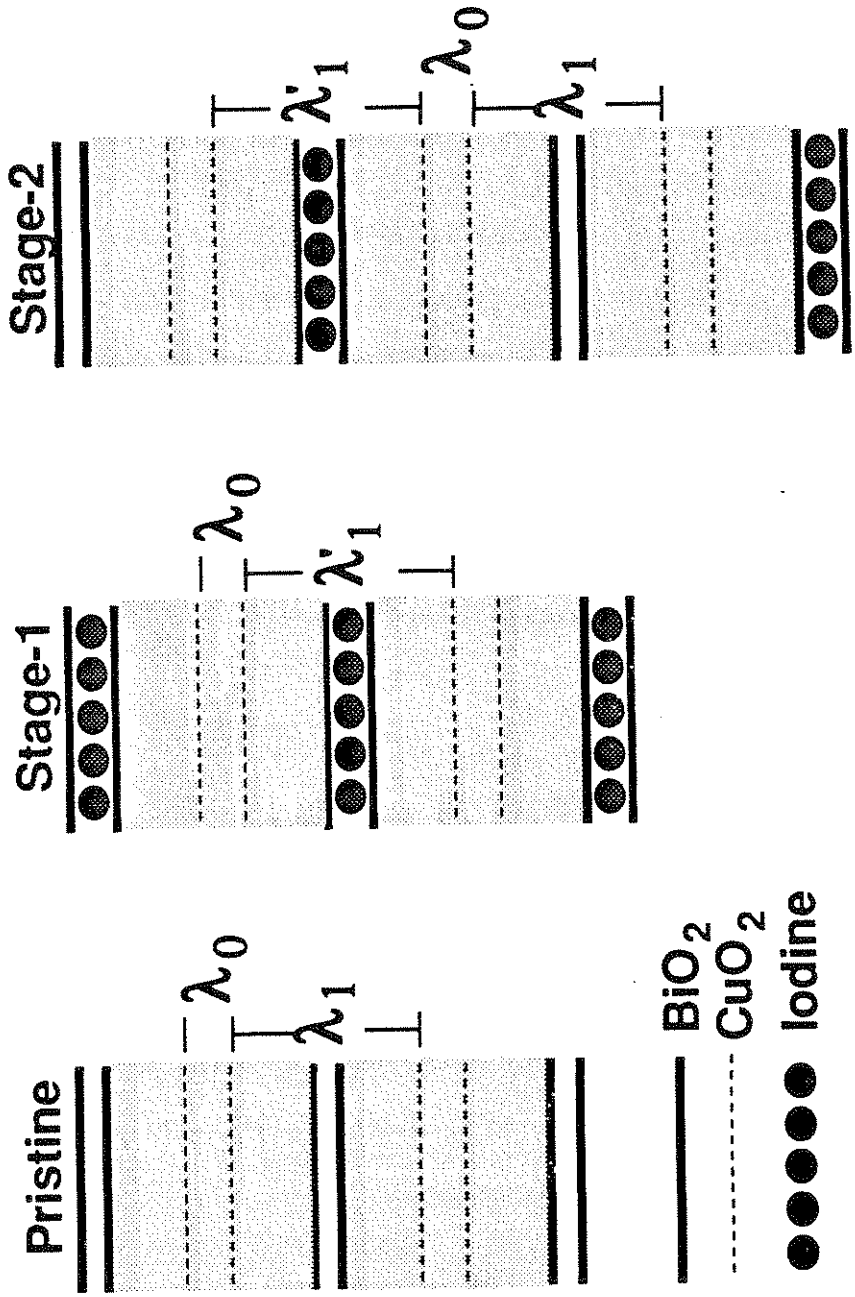

Figure 4.5 Schematic representation of the coupling parameters λ between the different CuO_2 layers in the pristine, stage-1, and stage-2 compounds. λ_o is the coupling parameter between CuO_2 layers within the same block, λ_1 (λ_1') is the coupling parameter between CuO_2 layers in adjacent blocks across a pristine (intercalated) BiO bilayer.

inconsistencies in the spinon-holon theory as a whole revealed by transport measurements (see chapter 5), the layering model used by WHA is non-mechanism specific. Here we apply the layering scheme to the present experiment to discuss the effects of intercalation and exhibit the merits of this approach.

In the linear layering model, the superconducting amplitude in plane i, η_i, depends on η_{i+1} and η_{i-1} and the couplings between the planes, $\lambda_{i,i+1}$ and $\lambda_{i,i-1}$. For $Bi_2Sr_2CaCu_2O_x$, there are two different couplings, λ_o and λ_1, (see Fig. 4.5.) for nearest and next-nearest planes respectively. The nearest planes are within a block whereas the next-nearest planes are in adjacent blocks. Since all the CuO_2 planes are equivalent, all the η's are equal and the eigenvalue equation for T_c, $(\lambda_o + \lambda_1)\,\eta = T_c\eta$, yields

$$T_c(\text{pristine}) = \lambda_o + \lambda_1. \tag{4.4}$$

For stage-1 $IBi_2Sr_2CaCu_2O_x$, the model is the same but with λ_1 replaced by λ_1' since the next-nearest plane coupling is assumed to be grossly affected by the intercalation, see Fig. 4.5. The predicted stage-1 T_c is then $\lambda_o + \lambda_1'$.

For stage-2 $IBi_4Sr_4Ca_2Cu_4O_x$, the CuO_2 planes are no longer equivalent; there are planes (a) coupled by λ_o and λ_1, and planes (b) coupled by λ_o and λ_1', see Fig. 4.5. The eigenvalue equation for T_c is then

$$T_c \begin{pmatrix} \eta_a \\ \eta_b \end{pmatrix} = \begin{bmatrix} \lambda_1 & \lambda_o \\ \lambda_o & \lambda_1' \end{bmatrix} \begin{pmatrix} \eta_a \\ \eta_b \end{pmatrix} \tag{4.5}$$

If we assume intercalation completely destroys the next-nearest plane coupling, then $\lambda_1' \rightarrow 0$, and the measured T_c(stage-1) yields $\lambda_o = 80$K. With T_c(stage-2) = 85K, $\lambda_o =$

Stage Index	Predicted T_c (K)
2	85
3	87
4	88
5	89

Table 4.2 The predicted superconducting transition temperatures for different stage indices based on a generic linear inter-layer coupling model.

80K, and $\lambda_1' = 0$K, we find $\lambda_1 = 9.7$ K. This is consistent with the results for the pristine material where T_c is typically 90K [$= (\lambda_o + \lambda_1)$].

It is possible to use the above analysis to predict the T_c's for higher stage compounds. Assuming $\lambda_o = 80$K, $\lambda_1 = 10$K and $\lambda_1' = 0$K, Table 4.2 shows the predicted T_c's for stages 2, 3, 4, 5, and 6 which rapidly approach the T_c for the pristine material as can be expected. Although we have demonstrated that stage-3 and stage-4 structures exist for iodine intercalated $Bi_2Sr_2CaCu_2O_x$, we have not been able to reliably determine the T_c's for these minority phases.

A second approach incorporates interplane interactions into a BCS-like framework. Such a model has been advanced by Ihm and Yu (IY)[57], although IY neglected interblock coupling. Since our experiments indicate that this coupling cannot be neglected, we incorporate such a coupling into a phenomenological model which is essentially an extension of the original IY work.

In the IY model the transition temperature is given by $kT_c = 1.14\hbar\omega \exp(-F)$ where $\hbar\omega$ is the range of the pairing mechanism and F is obtained by solving the following set of gap equations,

$$\Delta_\ell\left[1 - \lambda_a F(\Delta_\ell)\right] = \sum_{\ell'} \Delta_{\ell'}\lambda_{er} F(\Delta_{\ell'}) \tag{4.6}$$

$$F(\Delta_\ell) = \int_0^{\hbar\omega} d\varepsilon \frac{\tanh\left[\left(\varepsilon^2 + \Delta_\ell^2\right)^{1/2} / 2kT\right]}{\left(\varepsilon^2 + \Delta_\ell^2\right)^{1/2}} \tag{4.7}$$

where Δ_ℓ is the gap associated with a given layer ℓ, $F(\Delta_\ell)$ is the gap function, ε is energy, k is Bolzmann's constant, λ_a [λ_{er}] is $N(\varepsilon_f)V_a$ [$N(\varepsilon_f)V_{er}$], the intra-plane and nearest (within the same block) CuO_2 plane couplings, V is the strength of the interaction, and

$N(\varepsilon_f)$ is the density of states at the Fermi level and is assumed to be the same for all CuO_2 planes. The smallest positive F produces the lowest free energy and hence the highest T_c so the desired solution is this value of F.

We extend the IY model by including the effects of the next-nearest plane coupling into the calculation. This introduces an additional coupling constant, λ_n corresponding to the next-nearest plane coupling, i.e., the coupling between the CuO_2 planes in adjacent blocks. Just as in the linear coupling model discussed above, we assume that the effect of intercalation is to change $\lambda_n \rightarrow \lambda_n' \approx 0$. That is to say, the coupling across an intercalated layer has been reduced so far that it can be treated as zero. Given this assumption, we derive[30] the following results,

$$F(\text{pristine}) = \left(\frac{1}{\lambda_a + \lambda_{er} + \lambda_n}\right) \tag{4.8}$$

$$F(\text{stage-1}) = \left(\frac{1}{\lambda_a + \lambda_{er}}\right) \tag{4.9}$$

$$F(\text{stage-2}) \approx \left(\frac{1}{\lambda_a + \lambda_{er} + \frac{\lambda_n}{2}}\right) \tag{4.10}$$

$$F(\text{Bi-2223}) = \left(\frac{1}{\lambda_a + \sqrt{2}\lambda_{er} + \lambda_n}\right) \tag{4.11}$$

Notice that the results of our calculation for stage-1 agree with the IY results for pristine Bi-2212 as they should since in both cases the effects of inter-plane coupling are ignored. If we fit the coupling parameters λ_a, λ_{er}, and λ_n for $\hbar\omega = 0.1$ eV (from IY) to the experimentally determined T_c's of pristine Bi-2223 ($T_c = 110$ K) and the pristine Bi-2212

(T_c = 90 K) and stage-1 IBi-2212 (T_c = 80 K) compounds, we obtain λ_a = 0.2840, λ_{er} = 0.0725, and λ_n = 0.0156. Although λ_n is small (~5% of λ_a), it is over 20% of the size of λ_{er} and therefore not negligible. Inserting these parameters into Eq. (4.10), this model predicts the stage-2 T_c to be 84.9 K, in excellent agreement with the experimentally determined T_c = 85 K. Hence with the interblock coupling included, a BCS-like model accounts well for the intercalation-induced shift in T_c for the stage-2 material. The model can also be extended to predict the T_c's of higher stage compounds, although the dependence of F on the coupling is much more complex than for lower stages.

Therefore we conclude that the effects of interblock coupling are indeed important in determining the transition temperature in the BSCCO system. In addition, intercalation provides an excellent technique to extract the importance of this coupling because of the controlled fashion in which the crystal structure is modified. There are two important steps in this line of research which need further study. First. one would like to be able to compare and contrast the effects of intercalation on a host structure using two different intercalants to help isolate intrinsic effects. Until very recently no other intercalant has been incorporated into the BSCCO structure as uniformly and cleanly as iodine. Kumakura *et al.* appear to have intercalated AgI_2 into BSCCO[48] resulting in a very clean system with the lattice constant expansion of more than twice that found in the IBi-2212 system. We have tried to produce this intercalation compound without success. One difference is that their host structure is polycrystalline BSCCO crystals imbedded in Ag tape, whereas we have used high quality single crystals. Kumakura *et al.* report that the resulting change in T_c for this material is $\Delta T_c \approx$ -26 K, and at this point it is unclear if charge transfer effects are playing a role. The other line of research would be to examine the effects of intercalation on one of the other high T_c compounds. The first obvious choice would be the closely related Tl compounds. Unfortunately, the Tl-system differs from the BSCCO system in one important respect, the binding between the Tl bilayers is

considerably stronger than in BSCCO. One simple way to see this is to compare the lattice spacing of these layers, in pristine BSCCO the BiO-BiO separation distance is 3.24 Å whereas for the Tl compound the TlO-TlO separation distance is only ~2.0 Å which is comparable to all the other layer to layer spacings in this material. Therefore, the Tl compound does not have a micaceous morphology and is not a good candidate for intercalation. Of course, the other side of this is that if it could be intercalated there is no *a priori* reason for the intercalant to go between the TlO bilayer and it may in fact end up much closer to the important CuO_2 layers. As for other high T_c compounds, some claims of fluorine intercalation into $YBa_2Cu_3O_x$ were reported but subsequent studies showed that this was a substitutional effect where the apical oxygen atoms located above the Cu atoms in the BaO plane were being replace by fluorine. Therefore, to date no other high T_c compound has be successfully intercalated.

Chapter 5

Electrical Transport

5.1 Introduction

The unusual normal state properties of high T_c copper oxides have been the focus of many theoretical studies. It has been claimed[58] that clarifying the nature of the normal state could be the key to understanding the mechanism of high T_c superconductivity in these materials. Various theories[59] have been proposed which differ in their descriptions of the normal state and in particular the conduction mechanisms between and within the CuO_2 planes and their role in high T_c superconductivity.

In pristine Bi-2212, the normal state in-plane resistivity typically varies linearly with temperature, whereas the out-of-plane resistivity almost universally displays semiconductor-like behavior.[60] In addition, the ratio of the out-of-plane to in-plane resistivities can be as high as 10,000. An important issue is whether these anisotropies arise from the intrinsic nature of the CuO_2 network and are intimately related to T_c, or if they are just a consequence of the intermediate layer structure between the CuO_2 planes with no direct relation to the superconductivity mechanism.

Intercalation allows us to shed some light on these questions because one is able to modify the pre-existing structure in a very controlled way. Intercalating into the BSCCO structure between the BiO bilayers will physically increase the separation between the CuO_2 planes in adjacent blocks. However, the electronic coupling between the layers will depend critically on the intercalant. Studies on both the in-plane and out-of-plane resistivities in iodine intercalated Bi-2212 were performed.[31] In the normal state above T_c, intercalation is found to have no effect on the CuO_2 plane sheet resistance of the host Bi-2212 material, but it results in a "metallization" of the out-of-plane electrical conduction. These results are directly relevant to the issues of interplanar coupling and the superconductivity mechanism.

5.2 Contact application and geometries

Attaching contacts to the intercalated BSCCO samples proved to be fairly difficult. First we simply attempted using silver paint (Dupont, Conductor composition #4929N) as is done in the pristine material. One typically bakes on the contacts to the pristine material to get contact resistances of $< 1\ \Omega$. To avoid de-intercalation problems this baking proceedure was not done on the intercalation samples. Even without baking, the contact resistance to pristine BSCCO samples was typically 1- 10 Ω. For intercalated BSCCO the resulting contacts where unusable with a contact resistance of $>1000\ \Omega$. Believing that the problem was accumulated iodine on the surface, the samples were freshly cleaved and then the contacts where applied immediately. Although this improved the situation, the contact resistance was still too large, typically $\geq 300\ \Omega$. It appears that the iodine in the sample reacts with the silver forming AgI which is an insulator, hence yielding the large contact resistances. Several other types of contact paste where tried including Au and graphite, but these also did not work for unknown reasons. Silver epoxy was also tried without success. We then tried to sputter contacts onto the sample using a Hummer X sputtering machine. Samples were freshly cleaved and masked and placed in the sputtering machine. Attempts where made using Au, Ag, Au/Pd, Pd. All of the resulting contacts where not satisfactory. Next we tried evaporating contacts using gold or indium with similar poor results. The next attempt was to apply contacts to samples prior to intercalation and see if they survived the intercalation process. Several samples with virtually all of the different contact types previously applied were intercalated with iodine. None of the contacts survived. Finally, decent contacts where achieved using Pt paint (Englehard, #6926). This was missed the first time because the Pt paint itself will dry with a high resistance if the improper amount of thinner (Ethyl-Butyl Acetate — Kodak) is used.

The following procedure was employed to achieve good electrical contacts to the iodine intercalated samples. First the Pt paint was thinned with a small amount of EB Acetate. To check that the Pt paint had the appropriate amount of thinner, some paint was applied to a cover-glass slide which was then heated to ≈ 100 °C for about 30 - 60 seconds. If the resistance was too large the consistency of the paint was changed and the test repeated until the resistivity of the dried paint itself was less than a few mΩ-cm. At this point 1-mil annealed gold wires were attached to a freshly cleaved sample using the Pt paint mixture. If the sample is not freshly cleaved then one can not get low contact resistances. After attaching the wires with Pt paint, the sample was placed (in air) on a preheated hot-plate at a temperature of 100 - 120 °C for 15 - 45 seconds. If the temperature is significantly higher (> 200 °C) than this then evidence of escaping iodine can be detected around the sample. The best samples had contact resistances of less than 10 Ω but samples with contact resistances of up to 50 Ω where used successfully.

Unfortunately, if the samples are cooled to LN_2 temperatures with just the Pt paint to hold the wires on then the difference in thermal contraction between the sample and the Pt paint combined with the brittleness of the Pt-contacts results in the contacts popping off. To avoid this problem an additional material must be applied to provide mechanical support. Different electrically insulating materials like GE varnish and various epoxies were tried but all of them reacted with the Pt-contacts and destroyed them. Finally, what was used was partially thinned (EB Acetate) Ag paint applied over the Pt-contacts so that it made physical contact to the sample on either side of the Pt-paint contact. The Ag paint mixture was thick enough that it would not freely flow but thin enough so that it could be applied easily. The Ag paint provides the mechanical support and the Pt paint provides the electrical contact to the sample. Care was taken to avoid physical contact between the Ag paint from adjacent pads.

There were several different contact geometries employed. To measure only the **ab**-plane resistivity (ρ_{ab}), the in-line four probe configuration shown in Fig. 5.1(a) was used. If the **c**-axis resistivity (ρ_c) was required then one of two geometries were used. The first, shown in Fig. 5.1(b), consists of a four point geometry with large area current pads and small area voltage pads. For some samples, the current pads actually surrounded the voltage pads yielding a donut-like geometry. The problem with this configuration was that because of the additional Ag paint required for mechanical support the actual electrical contacts could not be brought very close together. This resulted in the **c**-axis measurement being contaminated by the **ab**-plane resistivity.

The most common method used was that of the Montgomery configuration[61,62] shown in Fig. 5.2. This method is ideally suited for measuring materials with an anisotropic resistivity. The only requirement for using this technique is that the sample geometry must be rectangular. The standard configuration, Fig. 5.2(a), consists of placing four small contact pads in the corners of one face of the sample. Two different resistances are measured, first current is applied to contacts A-B and voltage is measured across C-D yielding $R_{AB,CD}$ and second, current is applied to contacts A-C and voltage is measured across B-D yielding $R_{AC,BD}$. If the sample is thin and has an isotropic resistivity then it was shown by L. J. van der Pauw[63] that the resistivity is uniquely determined by these two resistances and is given by solving the equation,

$$\exp\left(\frac{-\pi R_{AB,CD}}{\rho}\right) + \exp\left(\frac{-\pi R_{AC,BD}}{\rho}\right) = 1 \qquad (5.1)$$

H. C. Montgomery extended this work to the case of a rectangular prism sample with edges in the principle crystal directions. With this configuration there are only the three diagonal components to the resistivity tensor, ρ_{11}, ρ_{22}, and ρ_{33}. The concept behind the Montgomery method is that an anisotropic sample with edge lengths, ℓ_1, ℓ_2, and ℓ_3, will

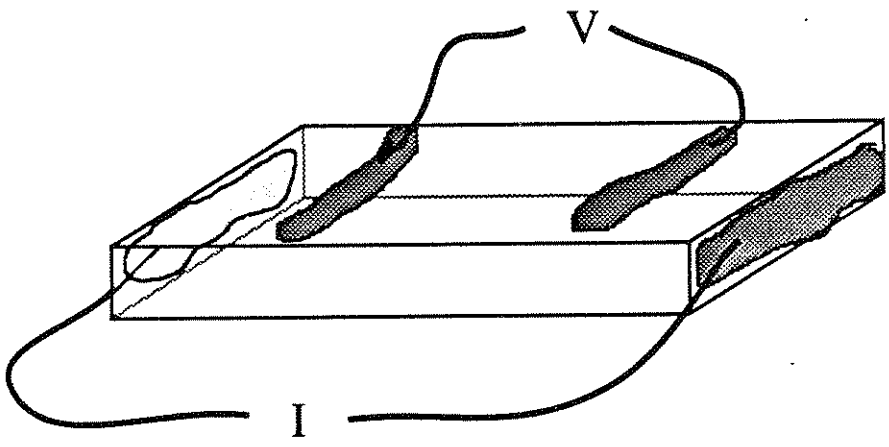

(a)

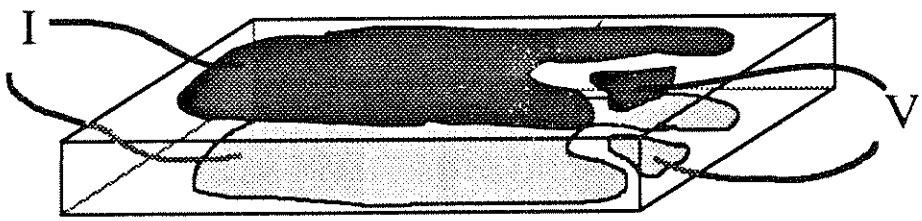

(b)

Figure 5.1 (a) Standard in-line 4-probe contact configuration. (b) Large I-small V 4-point contact configuration for measuring ρ_c.

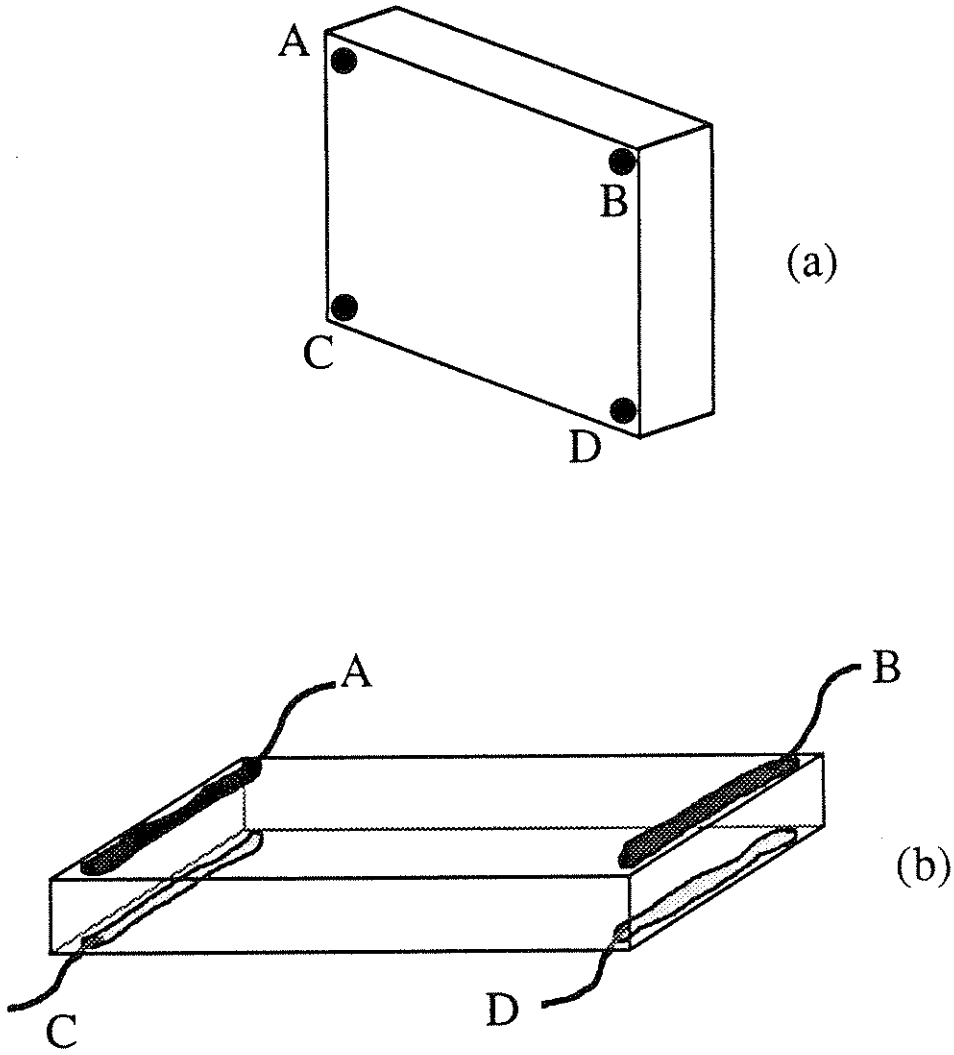

Figure 5.2 Contact configurations for the Montgomery method. (a) Standard configuration. (b) Stripe geometry to "short out" third dimension and put sample in "thin" limit.

behave the same as an isotropic sample with the edge lengths modified to compensate for the original differing resistivities. In other words, by just measuring resistances, you can not tell the difference between a sample 1mm long with a resistivity of 10 μΩ-cm and a sample 10mm long with a resistivity of 1 μΩ-cm. Once the appropriate edge length corrections are made then one needs to determine ρ. The form given in Eq. 5.1 is only valid for a thin sample, e.g., a thin film, however, Logan *et al.* have solved the problem for a sample of arbitrary thickness.[62] Therefore the Montgomery technique is to use the graphical solutions of Logan *et al.* to obtain ρ and then invert the process to obtain the two resistivity components in the plane of the original resistance measurement. If the third component of the resistivity tensor is required then an additional measurement using one of the other non-identical faces of the sample is required.

For the typical measurements on BSCCO and I-BSCCO, one of the sample edges corresponds to the **c**-axis and the other corresponds to a mixture of the **a**- and **b**-axes. Since the ρ_a and ρ_b are nearly the identical, especially when compared to ρ_c, this mixture does not affect the results. Given that the typical sample thickness in the **c** direction is ~10 - 30 μm it is not feasible to apply the point contacts directly to the face we wanted to measure, i.e., the thin edge. Instead, contact strips were painted down the edge on the **ab**-face of the sample as shown in Fig. 5.2(b). This effectively shorts out one of the sample directions (in the **ab**-plane) allowing us to us the "thin" sample approximation found in the Montgomery paper.[61] Comparisons of the accuracy of this method were obtained by adding two extra stripes on one of the **ab**-plane faces allowing the simultaneous measurement via both the Montgomery method and a standard in-line four probe geometry. Both techniques gave nearly identical results for the in-plane resistivity. Of course the advantage of the Montgomery method is that it also gives the **c**-axis resistivity.

5.3 Contactless resistivity measurement technique

It is very difficult to obtain a highly accurate measurement of the magnitude of the resistivity in the BSCCO and I-BSCCO systems because of the large uncertainty in determining the thickness of these thin sample (as large as 20%). Generally this is not that important since one often scales the resistivity to the magnitude at room temperature anyway. However, this is critically important if one is trying to determine the change in the resistivity as a result of intercalation. The problem is that in order to obtain good electrical contact to I-BSCCO it is necessary to cleave the sample after intercalation and therefore a before and after measurement of the resistivity is contaminated by the lack of accuracy in the determination of the thickness of the sample. To avoid this problem we chose to build a contactless resistance measurement system which would allow us to measure the identical sample before and after intercalation.

The experimental arrangement of the contactless method that we built was based on the work of Sakakibara *et al.*[64] and is shown in Fig. 5.3. The system consists of two small coils (A and B) wrapped on a machined sapphire rod. Sapphire is used to reduce the effects of thermal contraction when measurements to low temperatures are performed. Between the two coils is a thin slit in the sapphire rod into which the sample is placed. The transmitter coil (A) is connected to a frequency generator which produces a sinusoidal signal at a frequency of ~ 10-50 MHz. This signal induces eddy currents in the sample which then dissipate some of the energy. The sample must be thin enough to allow a measurable amount of the signal to pass through it and be picked up at the receiver coil (B). By measuring the signal at (B) with a high-frequency lock-in we can determine the percentage transmission through the sample and this value is directly related to the conductivity of the sample. In addition to avoiding the problems with contacts, this technique has the advantage that the measured resistivity is the bulk value and is not affected by poor surface quality.

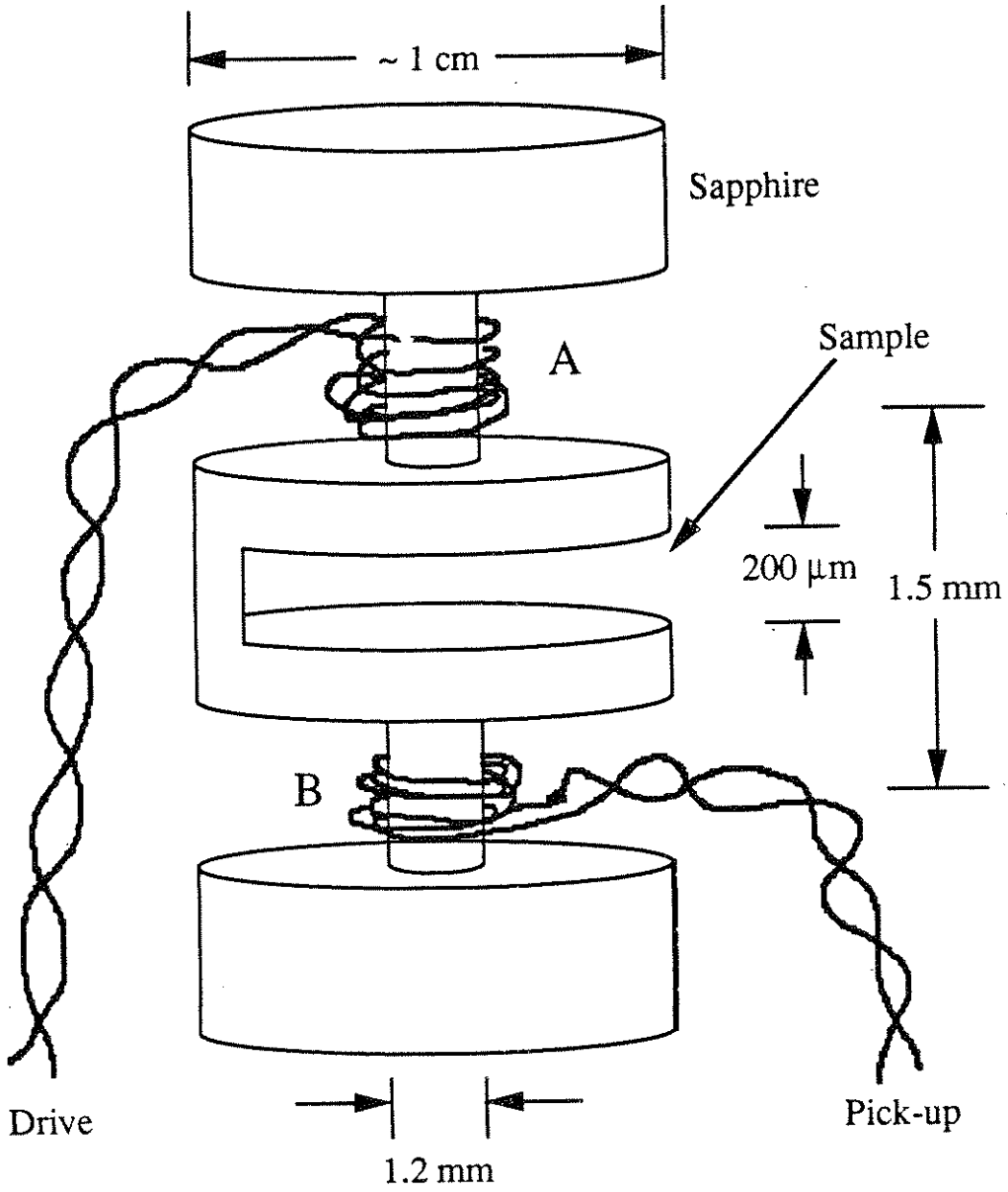

Figure 5.3 Schematic of contactless resistance measuring probe.

We need to use Maxwell's equations to address the problem of determining the relationship between the conductivity of the sample and the transmitted signal detected at coil B. In order to formulate and solve the boundary-value problem for the magnetic vector potential of the system it is necessary to make three simplifying assumptions. First, we assume that the winding extent of the coils is thin enough that each can be treated as a single-plane coil. Second, it is assumed that the conductivity in the plane of the eddy currents is a scalar real number. As stated above, the conductivities in the **a** and **b** directions are nearly identical. In addition, because of the huge anisotropy in this material, any small misalignment will not result in eddy currents flowing in the **c** direction. Therefore, above the superconducting temperature this assumption for the conductivity is valid. Below the transition temperature, however, the conductivity includes an imaginary term as a result of the presence of superconducting pairs. Using the two-fluid model of Gorter and Casmir we find that the conductivity is given by[65]

$$\sigma_{eff} = \frac{ne^2\tau}{m}\left(\frac{n_n}{n}\right) - i\left(\frac{c^2}{4\pi\omega\lambda^2}\right) \tag{5.2}$$

where n is the total density of conduction electrons, m is the mass of the electron, τ is the scattering time, n_n is the density of "normal" electrons, λ is the London penetration depth, and ω is the angular frequency of the electric field. Therefore, well below T_c the conductivity is pure imaginary, but, at these low frequencies we also expect that the sample should completely shield the flux from the pick-up coil.

Finally, and most importantly, the sample size is assumed to extend far enough beyond the diameter of the coils so that edge effects can be neglected. In practice, this is the most difficult restriction to obtain because the typical I-BSCCO sample is only a few mm^2. Therefore the coil diameters where made as small as possible, on the order of 1.2mm. Because there was no longer the need to cleave the sample after intercalation,

pristine samples where specifically prepared so as to make them as large area as possible while keeping the thickness to less than about 100 μm so that they would still fit within the thin slit and also intercalate uniformly. Even with the above precautions, the effects of the fringing fields could not be completely removed. This will be address in more detail below.

The full calculation of the form of the transmission is rather tedious and can be found in the paper by Sakakibara *et al.*[64] The final result is given by

$$\begin{aligned} T &= V_s/V_o \\ &= \int_0^\infty \frac{4kk' J_1^2(ka)e^{-k(l-t)}}{(k+k')^2e^{-k't} - (k-k')^2e^{-k't}}\,dk \\ &\quad X\left(\int_0^\infty J_1^2(ka)\, e^{-kl}\,dk\right)^{-1} \end{aligned} \tag{5.3}$$

where V_s (V_o) is the voltage induced on the pick-up coil with (without) the sample in place, 'a' is the radius of the coils, 'l' is the separation between the coils, 't' is the sample thickness, $J_1()$ is the first order Bessel function and $k'^2 = k^2 + i\omega\mu_o\sigma$. The magnitude of T tells us the magnitude of the signal at the pick-up coil or equivalently the percentage transmission. The phase of T is the phase of the pick-up voltage relative to the drive signal. This formula was integrated using Mathematica for several different values of the thickness using the same coil geometry as Sakakibara *et al.* and the results were in full agreement with those presented in their paper.

The first thing to note about Eq. (5.3) is that the conductivity always appears with the frequency as $\omega\sigma$ so it would be natural to plot this as |T| vs. ρ/f for different thicknesses, where ρ is the resistivity and f is the frequency. However, if we assume

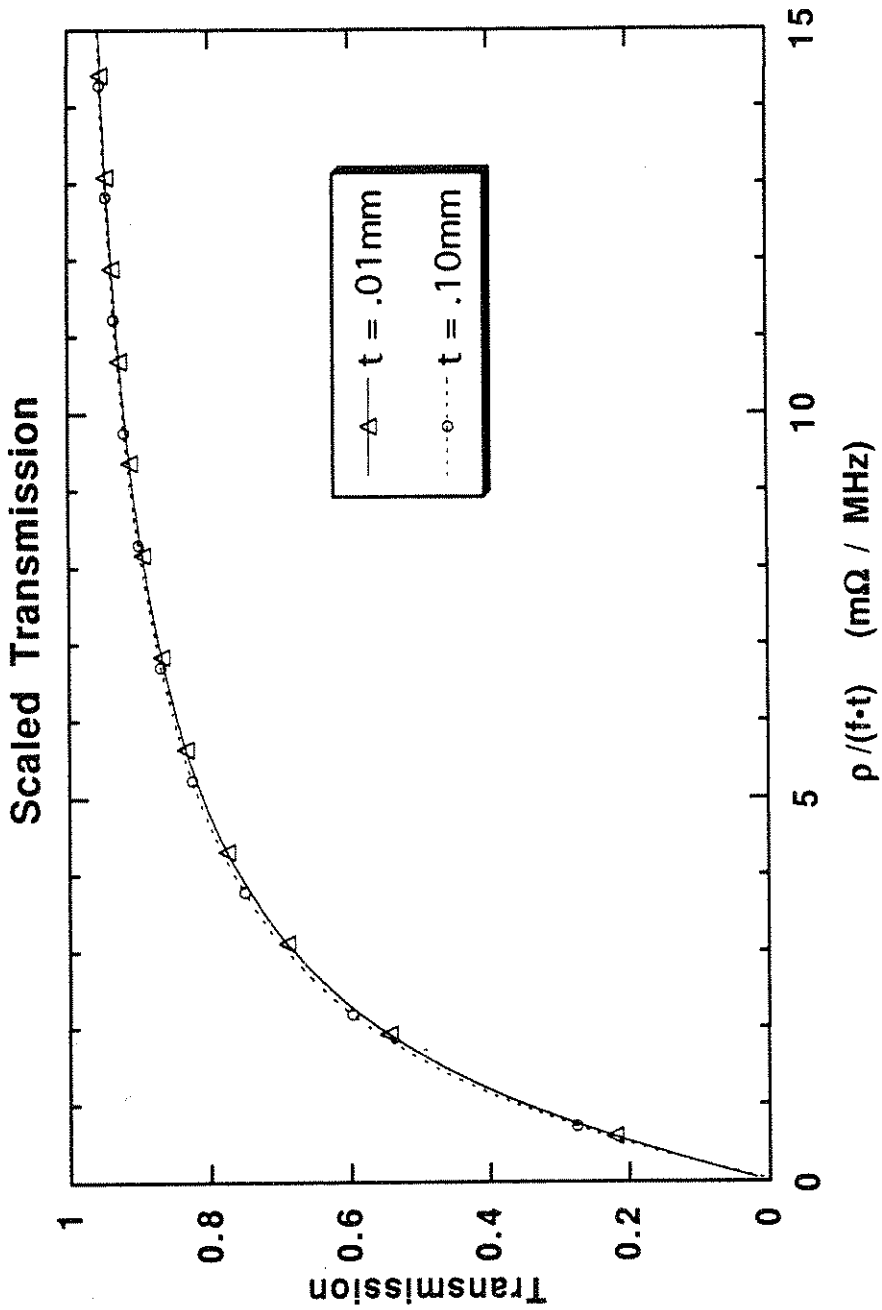

Figure 5.4 The percentage transmission as a function of $\rho/(f \cdot t)$ where ρ = resistivity, f = frequency, and t = sample thickness. The coil radius a = 0.6 mm, and the coil separation l = 1.5 mm. Two different thicknesses (t = 0.01 and 0.1 mm) differing by one order of magnitude yield essentially identical curves.

pho/(f•t)	Amplitude [t = .01mm]	Amplitude [t = .10mm]	pho/(f•t)	Amplitude [t = .01mm]	Amplitude [t = .10mm]	pho/(f•t)	Amplitude [t = .01mm]	Amplitude [t = .10mm]
0.05	0.019786	0.010832	5.104	0.81528	0.82132	10.158	0.9233	0.92573
0.183	0.072923	0.071105	5.237	0.82063	0.8265	10.291	0.9247	0.92708
0.316	0.12458	0.12783	5.37	0.82574	0.83145	10.424	0.92605	0.92839
0.449	0.17416	0.18075	5.503	0.83063	0.83618	10.557	0.92737	0.92967
0.582	0.22117	0.23013	5.636	0.83532	0.84071	10.69	0.92866	0.93091
0.715	0.26535	0.27599	5.769	0.8398	0.84505	10.828	0.9299	0.93211
0.848	0.30662	0.31842	5.902	0.8441	0.8492	10.956	0.93112	0.93329
0.981	0.34501	0.35756	6.035	0.84823	0.85319	11.089	0.9323	0.93443
1.114	0.38063	0.39365	6.168	0.85219	0.85702	11.222	0.93346	0.93555
1.247	0.41364	0.42689	6.301	0.85599	0.86069	11.355	0.93458	0.93663
1.38	0.44423	0.45755	6.434	0.85964	0.86422	11.488	0.93568	0.93769
1.513	0.47257	0.48583	6.567	0.86315	0.86762	11.621	0.93674	0.93872
1.646	0.49885	0.51195	6.7	0.86653	0.87088	11.754	0.93778	0.93973
1.779	0.52324	0.53612	6.833	0.86978	0.87402	11.887	0.9388	0.94071
1.912	0.5459	0.55851	6.966	0.87291	0.87705	12.02	0.93979	0.94166
2.045	0.56698	0.57929	7.099	0.87593	0.87996	12.153	0.94075	0.9426
2.178	0.58661	0.5986	7.232	0.87884	0.88277	12.286	0.94169	0.94351
2.311	0.60492	0.61658	7.365	0.88164	0.88548	12.419	0.94261	0.94439
2.444	0.62203	0.63334	7.498	0.88434	0.8881	12.552	0.94351	0.94526
2.577	0.63802	0.649	7.631	0.88696	0.89062	12.685	0.94438	0.94611
2.71	0.653	0.66364	7.764	0.88948	0.89305	12.818	0.94524	0.94693
2.843	0.66705	0.67735	7.897	0.89191	0.89541	12.951	0.94607	0.94774
2.976	0.68024	0.69022	8.03	0.89427	0.89768	13.084	0.94689	0.94853
3.109	0.69264	0.7023	8.163	0.89654	0.89988	13.217	0.94769	0.9493
3.242	0.70431	0.71367	8.296	0.89875	0.90201	13.35	0.94847	0.95005
3.375	0.71532	0.72438	8.429	0.90088	0.90407	13.483	0.94923	0.95079
3.508	0.7257	0.73447	8.562	0.90294	0.90606	13.616	0.94997	0.95151
3.641	0.73551	0.744	8.695	0.90494	0.90799	13.749	0.9507	0.95221
3.774	0.74479	0.75301	8.828	0.90687	0.90986	13.882	0.95141	0.9529
3.907	0.75357	0.76153	8.961	0.90875	0.91167	14.015	0.95211	0.95358
4.04	0.7619	0.76961	9.094	0.91057	0.91343	14.148	0.95279	0.95424
4.173	0.76979	0.77727	9.227	0.91233	0.91513	14.281	0.95346	0.95488
4.306	0.77729	0.78454	9.36	0.91404	0.91678	14.414	0.95411	0.95551
4.439	0.78442	0.79144	9.493	0.9157	0.91839	14.547	0.95475	0.95613
4.572	0.7912	0.79801	9.626	0.91731	0.91994	14.68	0.95537	0.95673
4.705	0.79766	0.80427	9.759	0.91887	0.92145	14.813	0.95598	0.95732
4.838	0.80381	0.81022	9.892	0.92039	0.92292	14.946	0.95658	0.9579
4.971	0.80968	0.8159	10.025	0.92187	0.92435	15.079	0.95717	0.95847

Table 5.1 Numerical data plotted in Fig. 5.4. See figure caption for details.

that the losses scale roughly linearly with sample thickness then we should be able to collapse all of results onto a single curve by plotting |T| vs. $\rho/(f \cdot t)$. Fig. 5.4 shows the data plotted in this form for different values of the thickness and one can see that both sets of data collapse quite closely to a single universal curve over the entire range. For the data shown in Fig. 5.4, the value of the coil radius, a, and separation, l, correspond to the values on the actual apparatus, a = 0.6 mm, l = 1.5 mm. Table 5.1 contains the numerical data plotted in Fig. 5.4. In addition to the nearly universal curve for the amplitude data, plots of the phase of T vs. $\rho/(f \cdot t)$ for different thicknesses also coincide for $\rho/(f \cdot t) \geq 3$ but for values less than this curves begin to separate. At the frequencies used in this experiment (~10-50 MHz) the phase measurements tended to be much more sensitive to the laboratory environment and the extracted resistivity values varied somewhat from measurement to measurement. On the other hand the amplitude measurement and the extracted resistivity was much more stable and repeatable and therefore we generally only used the resistivity extracted from the amplitude data.

Using Fig. 5.4 we can determine the effective range of resistivities that can be measured with this experimental set-up. If the percentage transmission becomes too small then noise and spurious coupling effects limit the accuracy of the measurement. In the other limit, for high |T| the system starts to become insensitive to small changes in the resistivity assuming f and t are fixed, (see Fig. 5.4). Therefore, the practical effective range of |T| is given by $0.1 \leq |T| \leq 0.8$. Assuming a broad availability of sample thicknesses from 5μm to 100 μm and a frequency range of 10-50 MHz this limits the range of measurable resistivities to $10\ \mu\Omega\text{-cm} \leq \rho \leq 1000\ \mu\Omega\text{-cm}$. Resistivities as low as 1 μΩ-cm may be obtainable by using a frequency of 1 MHz but the system has not been tested in that frequency range. For a given optimized frequency and thickness, a change in ρ by as much as a factor of 10-20 can be measured.

One effect of having a measurable fringing field is that there is a direct coupling of the drive and pick-up coil independent of the presence of the sample. In addition, if the sample becomes too small (≤ coil diameter) then the entire calculation is suspect and can not be applied. For sample sizes ≥ (2-3 x coil diameter) the fringing effect is small and can safely be ignored. For the measurements on the BSCCO and I-BSCCO compounds the typical sample size was very close to this limit and therefore some small evidence for fringing field effects was detectable. In particular, there persisted a transmitted signal even after the samples went superconducting which remained constant for all temperatures well below T_c. This signal was primarily do to a fringing-effect induced direct coupling of the drive and pick-up coils, and to first order can be considered to be a constant offset to the transmitted signal. Therefore, magnitude of the transmitted signal was corrected by subtracting off any small value of voltage detected well below T_c.

The system was first calibrated using $NbSe_2$ samples obtained from Brian Burk. For this material, it was easy to obtain high quality thin samples with size > (3 x coil diameter). Measurement of magnitude of the resistivity as well as its temperature dependence agreed to within a few percent of that found in the literature.[66] Following this, samples of pristine BSCCO were measured and the magnitude, temperature dependence and T_c agreed with samples measured from the same batch using standard in-line 4-probe techniques.

5.4 ab-plane resistivity

Measurements of the in-plane resistivity were made using the in-line 4-probe, Montgomery, and contactless techniques mentioned above. The in-plane resistivity is assumed to be dominated by conduction through the CuO_2 planes with essentially no contribution coming from conduction in the BiO and SrO planes. Therefore, since the intercalant (iodine) is located far from the conducting planes, it is not expected to modify

the temperature dependence of the resistivity. This should be contrasted to stage-1 intercalated graphite, for example, where the intercalant is immediately adjacent to the originally conducting graphite layers and the temperature dependence is affected.[67] As mentioned previously however, the presence of iodine could easily affect the magnitude of the resistivity through charge doping.[68] Since the resistivity is related to the carrier concentration, *n*, any change in *n* is expected to show up as a change in the magnitude of the resistivity.

Fig. 5.5 shows the in-plane resistivity, ρ_{ab}, for a given crystal before (Bi-2212) and after (IBi-2212) iodine intercalation, obtained using the contactless rf technique. For Bi-2212 (open circles), ρ_{ab} displays the roughly linear temperature dependence in the normal state above T_c, as observed in many previous studies. For the same sample after intercalation (solid diamonds), ρ_{ab} shows a qualitatively similar behavior, except that, compared to pristine Bi-2212, the magnitude of ρ_{ab} is slightly larger and T_c is somewhat depressed (consistent with magnetization studies). There also appears to be a slight change in slope in ρ_{ab} for IBi-2212 near T ~ 180K.

Since intercalation expands the **c**-axis of Bi-2212 by 23%, an increase in ρ_{ab} upon intercalation is expected even in the absence of any change in the conduction properties of the CuO_2 planes. This is a common problem[69] in intercalation compounds where conduction is predominately through the host structure. If we assume that conduction is still dominated by the CuO_2 planes then the appropriate quantity to look at is the crystal sheet resistance, $R_\square = \rho/t$, where t is the thickness of the sample. This sheet resistance effectively measures the conductivity per CuO_2 plane since intercalation only affects the spacing and not the number of planes. The inset to Fig. 5.5 shows for the same sample the crystal sheet resistance before and after intercalation. Over much of the normal state temperature range, $R_\square$ is nearly identical for Bi-2212 and IBi-2212.

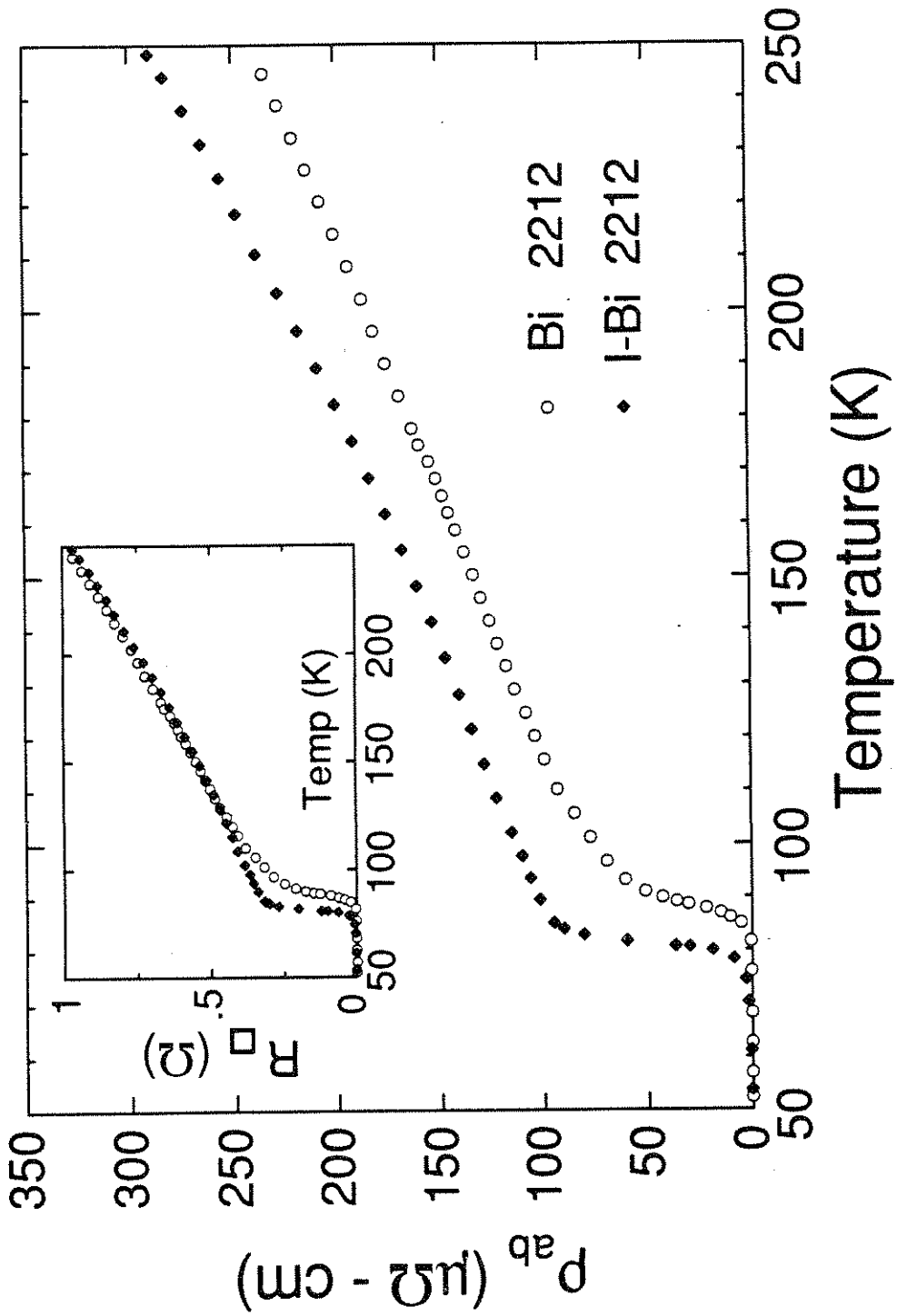

Figure 5.5: In-plane resistivity for the same crystal before (Bi-2212) and after (IBi-2212) intercalation. The inset shows the crystal sheet resistance $R_\square$ before and after intercalation.

Careful checks indicate that the magnitudes of $R_\square$ for Bi-2212 and IBi-2212 agree to within 1% at room temperature. Also, since the transmission intensity is a function of $\rho/(f \cdot t)$ the actual raw data measured give the sheet resistance and therefore the possible errors in measurement of the sample thickness do not affect this result. We thus conclude that the difference in **ab**-plane resistivity for Bi-2212 and IBi-2212 is a consequence only of the crystal expansion; *conduction along the CuO_2 planes is virtually unaffected by the intercalation*. On the other hand, as we show below, intercalation dramatically changes the out-of-plane conduction.

5.5 c-axis resistivity

Fig. 5.6 shows the **c**-axis resistivity, ρ_c, as a function of temperature for a pristine Bi-2212 crystal and an iodine intercalated IBi-2212 crystal. These data were obtained using the Montgomery method. Numerous pristine and intercalated specimens were measured with similar results. For pristine Bi-2212 (open circles), ρ_c shows the "semiconductor-like" temperature dependence characteristic[60] of out-of-plane transport for this and related materials. Although the increase in ρ_c with decreasing temperature has a complicated temperature dependence, it is often referred to as "1/T-like". Comparison of the 250K ρ_c value of Bi-2212 in Fig. 5.6 to ρ_{ab} at 250K for Bi-2212 in Fig. 5.5 demonstrates the extreme electrical anisotropy of this material, $\rho_{ab}/\rho_c = 1.6 \times 10^4$. The solid diamonds in Fig. 5.6 are for IBi-2212. In sharp contrast to the semiconductor-like temperature dependence observed in the pristine material, *ρ_c for the intercalated crystal shows an absolutely linear temperature dependence over the entire normal state range*. Hence, intercalation changes the semiconductor-like or 1/T-like behavior for ρ_c into metallic-like.

For any highly anisotropic material one must take precautions to insure that the properties measured are intrinsic and not due to a coupling in of the other components.

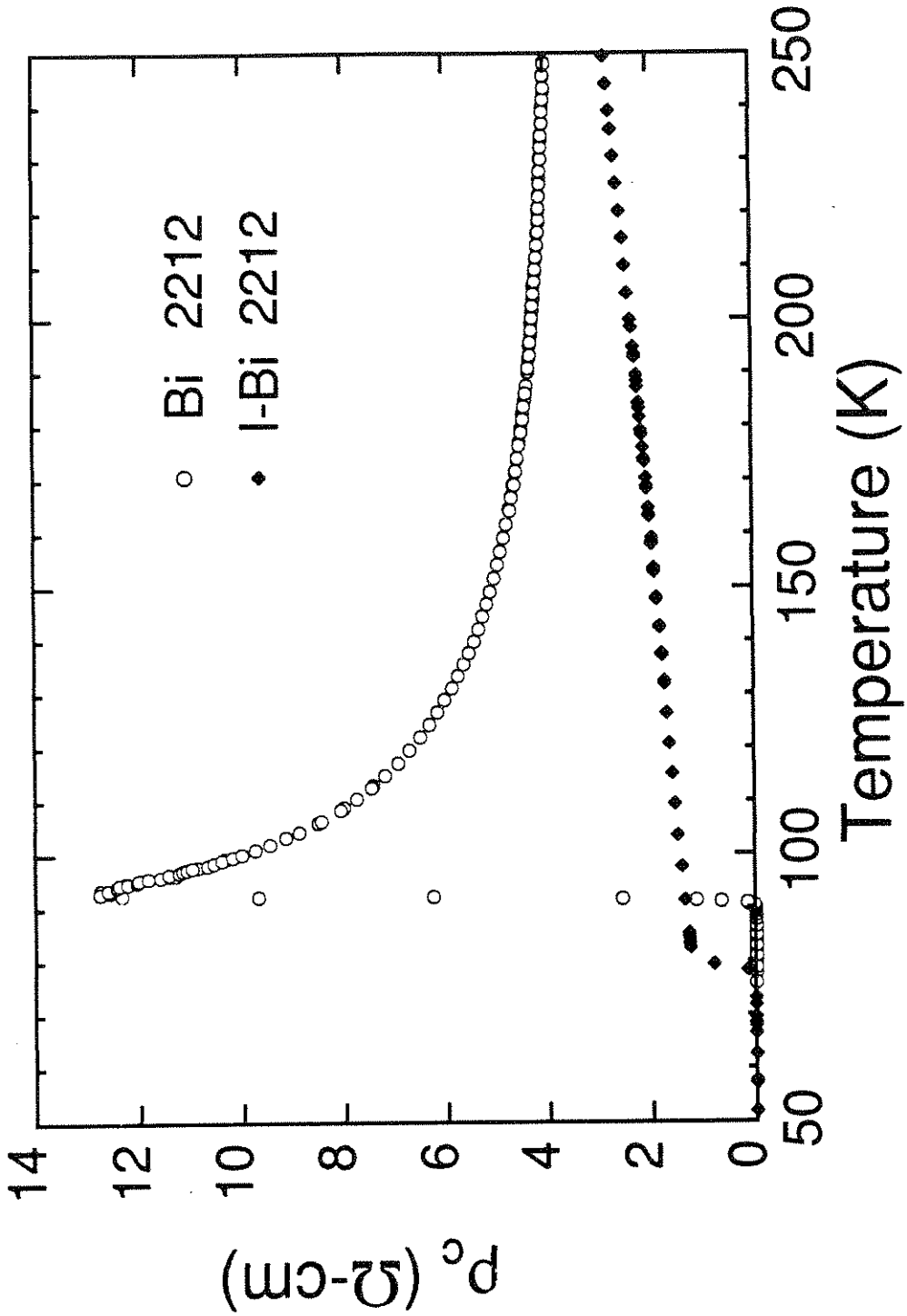

Figure 5.6: Out-of-plane resistivity vs. temperature for typical pristine (Bi-2212) and intercalated (IBi-2212) crystals.

In pristine Bi-2212, all evidence indicates that the measured **c**-axis conductivity is in fact intrinsic. Unlike highly oriented pyrolytic graphite (HOPG), which is composed of a mosaic of crystallites,[70] pristine Bi-2212 is a slowly grown high quality crystal. The crystals do not exhibit a sizable spread in the **c**-axis diffraction peaks as does HOPG and also BSCCO does not show a proclivity for screw dislocations, either of which could couple the **ab**-plane conductivity into the **c**-axis measurement.[71] In addition, the temperature dependencies of the σ_{ab} and σ_c are opposite with the former being metallic and the latter semiconductor-like. Therefore, the dramatic change in the **c**-axis conductivity of IBi-2212 must be either intrinsic or caused by an *intercalation induced* effect which couples in the **ab**-plane.

Unlike *intercalated* HOPG, where σ_{ab} increases by 10 - 100 times[16] thereby increasing its influence, in IBi-2212 the **ab**-plane conductivity remains unchanged. We conclude that the only way σ_{ab} could be coupled into the **c**-axis measurement is if the intercalation process itself induces defects which would *enhance* this effect.[16,71] The real-space TEM images with atomic resolution over regions >1000 Å show no defects in the planer structure. Defects involving breaking up and shifting of the structural units (Bi/Sr/Cu/Ca/Cu/Sr/Bi) seem unlikely at the intercalation temperatures employed (~130°C) considering the strength of the bonds that would have to be broken. Since the highly conducting CuO_2 planes are in the center of these units, several strong bonds would need to be broken to short out the **c**-axis conduction. Under an optical microscope the intercalated samples look similar to pristine Bi-2212 with smooth flat surfaces. X-ray and TEM electron diffraction patterns also show no significant disorder in the intercalated samples.

Defects like those expected in generating higher stages as in the Daumas-Hérold model[14] would not couple σ_{ab} into the **c**-axis measurement to give the effect seen since conduction from one set of CuO_2 planes to the next still requires **c**-axis conduction either

through the pristine-like interlayers or the intercalated regions. The former would lead to no change in the **c**-axis conductivity rather than making it metallic-like. Therefore, we find no evidence that the intercalation process couples σ_{ab} into the measurement of σ_c. Thus we conclude that the measured temperature dependence of σ_c *is intrinsic and has changed from semiconductor-like to metallic-like.*

Although the temperature dependence of the resistivity tensor in IBi-2212 is metallic-like for both in-plane and out-of-plane transport, it is important to note that the in-plane to out-of-plane conduction anisotropy remains extreme. Indeed, as Fig. 5.6 demonstrates, the rough order of magnitude of ρ_c well above T_c is quite comparable for pristine and intercalated specimens. Near T_c the anisotropy is reduced by about one order of magnitude but still remains quite large.

We now discuss the relevance of our findings to the mechanism of high temperature superconductivity. There have been several predictions of the normal and superconducting state behavior of the layered oxides by Wheatley, Hsu, and Anderson (WHA)[7,56] and by Anderson and Zou (AZ)[72], all based on a model derived from the resonating-valence-bond (RVB) theory. The experimental studies presented here can be used to examine these predictions and to provide information about microscopic interactions in these systems. Any viable model must account for both the small shift in T_c and the dramatic change in the out-of-plane conduction induced by intercalation.

The observed change in T_c with intercalation is consistent with the WHA model of layered systems[56] if we assume that the next-nearest CuO_2 plane coupling (Λ_m) is essentially eliminated by iodine intercalation while the nearest-plane coupling (Λ_o) in the intercalated material is the same as in the pristine material since these planes are within a single block. The couplings, Λ, have the form,

$$\Lambda_{o,m} \sim \frac{|T_{\perp o,m}|^2}{J} \tag{5.4}$$

where $|T_\perp|$ is the interlayer hopping matrix element for nearest-neighbor planes (o) and next nearest-neighbor planes (m), and J is the spinon bandwidth. If $\Lambda_m \rightarrow 0$, then either $T_{\perp m} \rightarrow 0$ or $J \rightarrow \infty$. The spinon bandwidth, J, depends only on the structure of the spinon energy spectrum which in turn is determined solely by the CuO_2 planes. The condition $J \rightarrow \infty$ is not physical nor is it reasonable as will be shown in the discussion of ρ_{ab} below. Thus, we are left with the conclusion that $T_{\perp m} \rightarrow 0$ or at least is greatly reduced.

We now examine the anisotropic electrical resistivity. In the AZ calculation, the resistivity in the **ab**-plane[72] is caused by the scattering of holons by spinons. Thus, ρ_{ab} is a probe of the in-plane interaction and the densities of states of the spinons and holons. Specifically,

$$\rho_{ab} = \left(\frac{m_B}{ne^2}\right)\left(\frac{2\pi}{\hbar}\right) t^2 g_s g_b T \tag{5.5}$$

where m_B is the effective mass of the holons, n is the holon density, t is the in-plane scattering matrix element between holons and spinons, and g_s (g_b) is the spinon (holon) density of states. The value of ρ_{ab} for the intercalated samples demonstrates that the resistance of the CuO_2 planes is unchanged by the intercalation. Furthermore, the values of t, g_s, g_b, and J depend only on the spinon-holon local environment *in the CuO_2 planes*, and would remain constant unless the intercalation affected the structure of the material in those planes. The near-plane interlayer hopping matrix element ($T_{\perp o}$) also only depends on the local environment of the closest spaced CuO_2 planes. Thus, we can

assume that t, J, g_s, g_b, and $T_{\perp o}$ are not affected by the intercalation. This supports the proposition that Λ_o is not altered by the intercalation, and that the observed depression in T_c is due to a reduction in Λ_m through a decrease in $|T_{\perp m}|$.

The out-of-plane resistivity ρ_c, however, poses a problem to an interpretation based on the AZ calculation. Intercalated samples display a metallic ρ_c down to T_c. The AZ calculation for ρ_c in a single-plane system,[72] following a similar development as for ρ_{ab}, gives

$$\rho_c = \left(\frac{\hbar}{2\pi e^2}\right)\left(\frac{ab}{c}\right)\left(\frac{1}{|T_\perp|^2 g_s g_b^2 T}\right) \tag{5.6}$$

where $T_\perp$ is the interlayer matrix element for the scattering of spinons and holons, ab is the area of the Cu-Cu square in the **ab**-plane, and c is the interlayer distance. Since in this interpretation Bi-2212 should have two types of **c**-direction tunneling -- from nearest neighbor planes and next nearest neighbor planes -- Eq. (5.6) is logically extended to give

$$\rho_c \sim \frac{1}{\alpha \Lambda_o T} + \frac{1}{\beta \Lambda_m T} \tag{5.7}$$

where α and β include factors of the densities of states, J, and the different **c**-axis spacings for next nearest neighbor and nearest neighbor CuO_2 planes.

In view of the T_c and ρ_{ab} measurements, if Λ_m decreases we would expect ρ_c for intercalated IBi-2212 to have a dramatically *increased* 1/T-like behavior, whereas experiment shows no evidence for *any* 1/T-like behavior (see Fig. 5.6). In addition, the T_c measurements indicate (see section 4.2) that $\Lambda_o \approx 9\Lambda_m$. Assuming the Λ_m term has been replaced by some other mechanism with the appropriate temperature dependence,

one would *still* expect to see a small 1/T contribution to the resistivity from the Λ_0 term near T_c. However, this is not observed experimentally.

In light of this inconsistency, the previously proposed model does not adequately explain the resulting ρ_c of the iodine-intercalated Bi-2212 material. In this theory, the description of the **c**-axis conductivity mechanism and the pairing interaction for the superconducting state (i.e. $T_\perp$) are intimately related, and the small change in T_c and the large effect on ρ_c cannot be self-consistently accounted for.

In conclusion, epitaxial iodine intercalation in Bi-2212 changes not only the superconducting transition temperature, but has a profound effect on the resistivity tensor. While the magnitude and temperature dependence of the CuO_2 plane resistance is relatively unaffected by intercalation, the **c**-axis resistivity is modified from semiconductor-like to metallic-like. These results appear inconsistent with an analysis confined within the WHA and AZ theoretical description for these systems.

Chapter 6

Magneto-transport

6.1 Introduction

For small magnetic fields all superconductors exhibit the so called Meissner effect whereby the magnetic flux is expelled from the material when it becomes superconducting. For larger magnetic fields the picture becomes more complicated and one finds that there are two classes of superconductors imaginatively named type-I and type-II. For type-I materials there is only one characteristic field defined as $H_c(T)$ which is the temperature dependent field above which the material will be driven into the normal state and below which all flux is expelled. For type-II materials there are two measurable characteristic fields, $H_{c1}(T)$ and $H_{c2}(T)$, and one thermodynamically defined field, $H_c(T)$. $H_c(T)$ is defined through the difference in the Gibbs free energy between the normal and superconducting states. H_{c1} defines the field below which the material behaves as a type-I-like superconductor and exhibits a complete Meissner effect, i.e., all flux is expelled from the material. On the other hand, H_{c2} defines the field above which the material will be driven into the normal state. For fields H such that $H_{c1} < H < H_{c2}$ the material is in the so called mixed state. Universally, the materials with the highest transition temperatures are type-II superconductors, including all the oxide superconductors.

The properties of the mixed state were first addressed in detail by Abrikosov using the macroscopic mean field Ginzburg-Landau theory[49] (GL). The GL equations describe the degree of superconducting order through a spatially varying complex order parameter $\Psi(\mathbf{r})$ in which $|\Psi(\mathbf{r})|^2$ was to represent the local density of superconducting electrons $n_s(\mathbf{r})$. Later Gor'kov showed[73] $\Psi(\mathbf{r})$ was proportional to the gap function $\Delta(\mathbf{r})$ provided the temperature is near T_c and the spatial variations of Ψ and the vector potential $\mathbf{A}$ are not too rapid. In the mixed state the energy of the system is lowered by allowing

flux to penetrate in quantized bundles called fluxons or vortices. Each vortex consists of a normal core region where the value of the superconducting order parameter, $\Psi(\mathbf{r})$, decays to zero. The radius of the core is ξ, the Ginzburg-Landau coherence length. The flux penetrates through the center of the core and decays away within a charateristic length λ, the magnetic penetration depth. The ratio $\kappa = \lambda(T)/\xi(T)$ determines if the material is type-I or type-II as can be seen by the following simplistic argument. The penetration of the magnetic field H_c into the superconductor lowers the free energy at the boundary layer by roughly $1/2\mu_o(H_c)^2\lambda$ whereas the presence of the normal core raises the free energy by $1/2\mu_o(H_c)^2\xi$, i.e. the loss of condensation energy. Hence the presence of a boundary interface will lower the free energy of the system if $\xi < \lambda$. The Ginzburg-Landau theory formalizes this argument and shows that the separation between type-I and type-II occurs for $\kappa = 1/\sqrt{2}$.

The properties of a superconductor in the mixed state can be profoundly different than in the state where no flux penetrates. The vortices have an effective interaction energy which cause them to form a lattice called an Abrikosov flux lattice with a separation of normal cores given by $(\Phi_o/H)^{0.5}$ where Φ_o is the flux density of a single quantized vortex. In addition, if current is passed through a superconductor in the mixed state then the vortices feel a Lorentz force proportional to $\mathbf{J}\mathbf{x}\mathbf{H}$. This Lorentz force can result in the dissipation of energy by the vortices if they are allowed to move in the sample even though the sample is still a *superconductor*. In real materials the vortices are subjected to pinning forces and the strength and distribution of that pinning dictates the nature of the dissipation. If the pinning is very weak then the vortices will flow freely in the material due to the Lorentz force giving rise to "flux flow" dissipation. According to the model of Bardeen and Stephen[74] dissipation occurs as a result of the transport current passing through the normal cores resulting in the superconductor manifesting a longitudinal resistivity given by,

$$\rho_f = \rho_n (H/H_{c2}) \tag{6.1}$$

where ρ_n is the normal state resistivity. In the other extreme, the case of strong pinning was addressed by Anderson[75] and Kim[76] where the motion of the flux lines is dependent upon an activation behavior. In this "flux creep" model, the Lorentz force is smaller than the pinning force but the presence of thermal activation frees some of vortices allowing them to dissipate energy through the Lorentz force. This activated flux motion gives rise to a resistivity given by

$$\rho_f \propto \exp(-U_{pin}/kT) \tag{6.2}$$

where U_{pin} is the pinning potential. Numerous studies have shown evidence for both types of dissipation in the high T_c oxides for some orientations of field and current. This dissipation manifests itself as an anomalously broadened resistive transition for samples in a magnetic field. An example of a broadened resistive transition[77] for Bi-2212 for magnetic fields parallel and perpendicular to the **ab**-plane is shown in Fig. 6.1.

One distinguishing characteristic of the oxide superconductors is their two-dimensional nature. In YBCO this anisotropy, though large, is not so great as to invalidate the three dimensional mean field treatment of the Ginzburg-Landau theory provided one is close to T_c. To accommodate this anisotropy, one replaces the original scalar effective mass m^* in the GL theory with an effective mass tensor $\tilde{\mathbf{m}}$. This results in an anisotropic penetration depth and coherence length thereby distorting the Abrikosov flux lattice. In YBCO the measured anisotropy in the coherence length is $\xi_c(0) \sim 2$ Å and $\xi_{ab}(0) \sim 12$ Å. Therefore, since the separation between the important CuO_2 layers is ~ 4.2 Å in the **c** direction, this approximation is only marginally justified except near T_c,

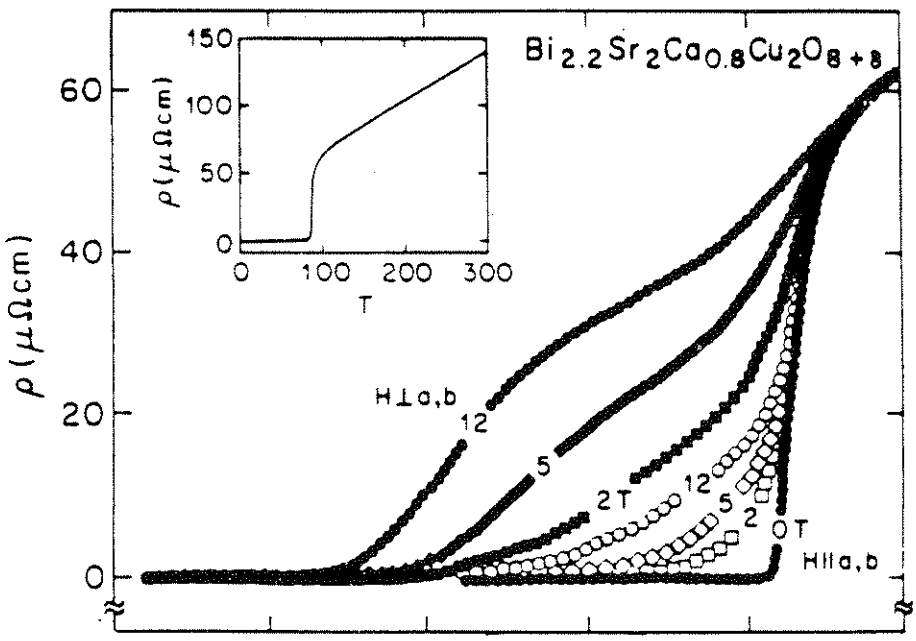

Figure 6.1 Temperature dependence of the **ab**-plane resistivity in Bi-2212 in three selected magnetic fields, 2, 5, 12 T, oriented parallel (open symbols) and perpendicular (filled symbols) to the **ab**-plane. Fig. is from ref. [77]

where ξ diverges as $(1-t)^{-0.5}$, with $t \equiv T/T_c$. For BSCCO the anisotropy is so extreme that "the three dimensional continuum picture is not a good approximation at all."[78] In fact, if we define the cross-over temperature, T_{co}, as the temperature at which $\xi_c(T)$ is equal to the separation between CuO_2 planes in adjacent blocks then one finds[79] that $T_c - T_{co} \approx 0.3$ K.

Rather than consider BSCCO as a three dimensional system, one may be justified in treating it as a series of two dimensional superconductors coupled together via weak Josephson coupling. This is the approach put forth in the Lawrence-Doniach (LD) model.[80] In this model the layers are in the **ab**-plane and the weak Josephson coupling occurs along the **c** direction. If the coherence length ξ_c perpendicular to the layers is greater than the separation of the layers *d*, this model essentially reproduces the results of the anisotropic GL model. If, however, $\xi_c \leq d$ then the results of this model differ significantly from the GL three-dimensional mean field approach.

One important prediction of the LD model is the possible coexistence of two different types of flux lattices.[81] For the field component along **c** the flux lattice is the standard Abrikosov lattice, however, for the field component along the planes there exists a Josephson vortex lattice. These Josephson vortices lie in the space between the superconducting sheets and have a width = $\Phi_o/H_{||}d$ where $H_{||}$ is the component of **H** along the planes and *d* is the separation between the superconducting planes. A Josephson vortex is uniquely different from an Abrikosov vortex in that the former does not have a normal core. Recently, evidence for these Josephson vortices has been observed in the **c**-axis I-V's for pristine Bi-2212.[82] In addition, Clem has proposed[83] that if the field is aligned at some angle out of the **ab**-plane then the vortices must cut through the planes at some point producing "pancake vortices" in the CuO_2 planes.

If one accepts that the excess field-induced dissipation arises from flux motion induce by a Lorentz force **JxH**, then one would anticipate that the resistivity would vary

as $\sin^2\Theta$, where Θ is the angle between the current **J** and the field **H**. Surprisingly, Iye *et al.*[84] and others have clearly shown that the dissipation in BSCCO is completely independent of Θ when **H** and **J** are both perpendicular to the **c**-axis. In contrast to this,[78] YBCO shows a small $\sin^2\Theta$ dependence and standard conventional flux flow superconductors show essentially a complete $\sin^2\Theta$ angular dependence. This would imply that the source of this discrepancy is coupled to the strong layered nature of YBCO and the *extreme* layered nature of BSCCO. To account for this behavior, Kes *et al.* have proposed[85] that the observed dissipation is due to an angular misalignment of less than 1° which would produce many "pancake vortices". These vortices then interact with the transport current to yield the Θ independent dissipation. Iye *et al.* argue that even without misalignment, there may be enough thermally activated pancake vortices to account for the dissipation. Finally, Kim *et al.* at Argonne have proposed an alternate explanation.[86] In their model the dissipation is not due to fluxon motion, but instead it is the result of the reduction in the Josephson critical current between the layers cause by the field-induced depression of the order parameter in the grains. This reduced critical current then causes an increase in the dissipation. Therefore, one must conclude that there is no true consensus on the physical cause of the field-induce dissipation (for all orientations of current and field) in the BSCCO system, and by analogy all of the oxide superconductors.

Clearly, however, the picture of dissipation in the BSCCO system is critically related to the two-dimensionality of the system and in particular, to the large separation of the CuO_2 layers. One is naturally led to the question of how the dissipation mechanism in BSCCO might be affected by increasing this separation via intercalation. By further decoupling the superconducting CuO_2 planes one may affect both the field penetration and dynamics. To examine the effect of intercalation we measured several iodine intercalated samples with various field and current orientations. The measurements

where made in an American Magnetics superconducting solenoid capable of producing dc magnetic fields up to 8 T.

6.2 **ab**-plane magneto-resistance

As mentioned previously, the **ab**-plane resistivity, ρ_{ab}, is essentially identical in the pristine Bi-2212 and the IBi-2212 compounds (for H = 0) other than a shift in the T_c of ~ -10 K. For this study, ρ_{ab} was measured using a standard in-line 4-probe contact configuration on samples with a typical trapezoidal geometry of 1mm x .3mm x 15μm. The samples were oriented with respect to the probe which was then placed in the bore of the solenoid magnet. The accuracy of the alignment of the sample with respect to the field was estimated to be < 1-2°.

Fig. 6.2 (a) shows the **ab**-plane resistivity of an iodine intercalated IBi-2212 sample for magnetic fields 0T, 1T, 2T, 4T and 7T. The field is oriented perpendicular to the **c**-axis (i.e. in the **ab** plane) and also perpendicular to the transport current density **J**. Fig. 6.2 (b) shows the another sample for the same set of magnetic field intensities. However for these data the magnetic field is oriented parallel to the transport current (still in the **ab** plane). Comparing these data to the corresponding data in Fig. 6.1 (open circles) for pristine BSCCO shows that there appears to be some change in the onset behavior but this is most likely do to oxygen content[87] or sample quality. If one focuses on the broadening of the transition defined here somewhat generally by looking at the 5% points of the magneto-resistance curves for the different fields compared to the 5% point for the zero field case, it is clear that the extent of the broadening has not been noticeably affected by the intercalation process. This would imply that the mechanism responsible for the anomalous resistive broadening is not closely coupled to the details of the spacer layers between the CuO_2 layers. This does not appear consistent with the model of Kim *et al.*[86] where the dissipation is due to changes in the Josephson critical current density

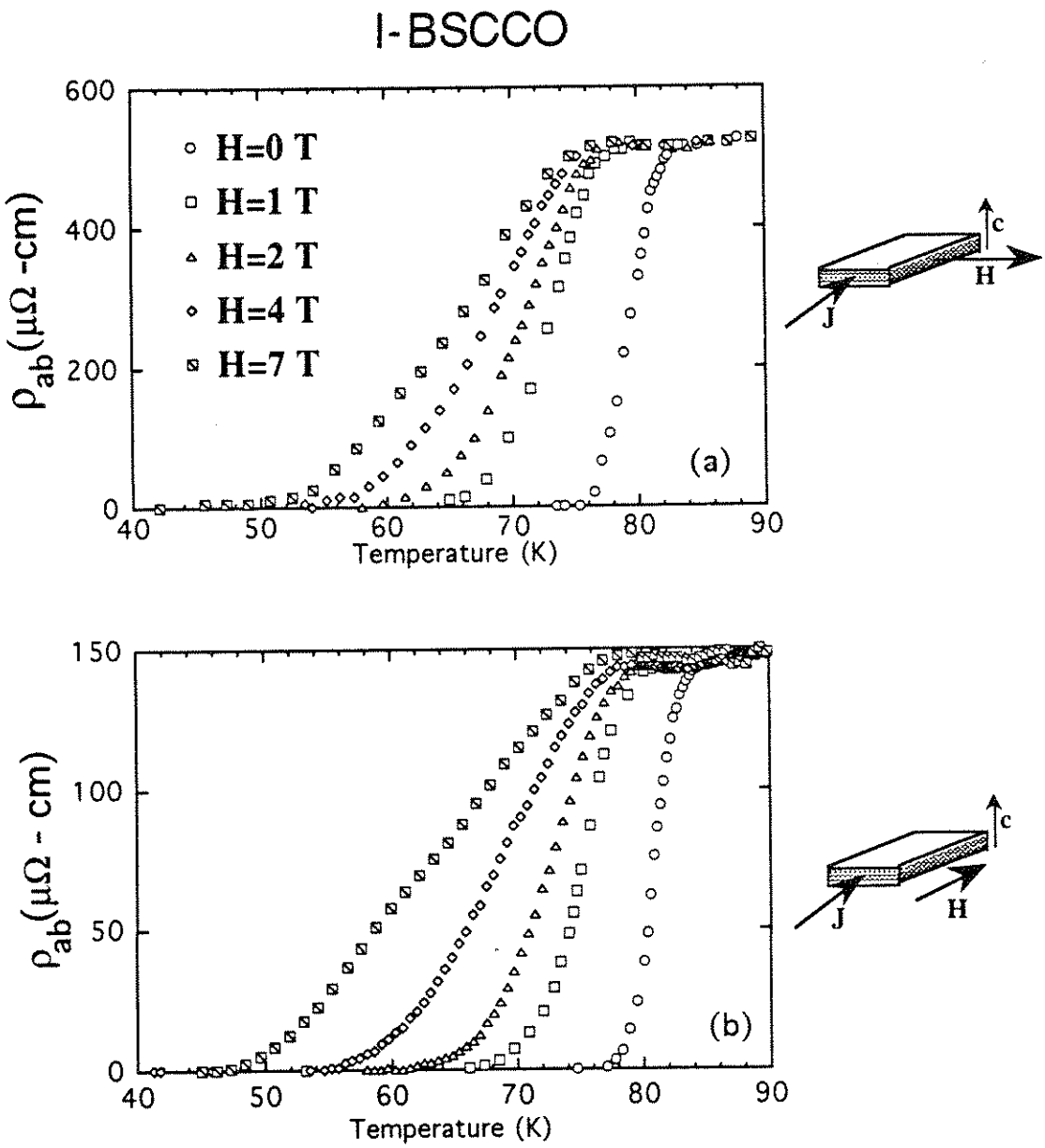

Figure 6.2 Temperature dependence of the in-plane resistivity ρ_{ab} in IBi-2212 for magnetic fields **H** of 0, 1, 2, 4, and 7 T oriented in the **ab**-plane. (a) has **H** perpendicular to the current **J**, (b) has **H** parallel to **J**.

between the CuO_2 layers and one would expect that the insertion of iodine between the BiO bilayers would modify this coupling. In addition, it has already been shown that the **c**-axis resistivity has been changed from a semiconducting-like to a metallic-like temperature dependence which also would also imply that a change in the dissipation behavior through this mechanism should be observed. On the other hand, these results are consistent with the models of Kes and Iye mentioned above since the dissipation in these models is due to pancake vortices in the CuO_2 layers and they are not expected to be significantly affected by the intercalation process.

Comparing Fig. 6.2 (a) where the field geometry is such that there exists a macroscopic Lorentz force and Fig. 6.2 (b) where there is no macroscopic Lorentz force, it is clear that the resistive broadening is still Lorentz force independent. This is consistent with the picture that the insensitivity to the angle Θ between the current density **J** and the field **H** is correlated with the two-dimensionality in this system. As mentioned before, the anisotropy in the resistivity ρ_{ab}/ρ_c is still on the order of 1000 at T_c and the transition temperature itself is still roughly comparable to that in the pristine Bi-2212, both of which when combined with the observation that IBSCCO still has a micaceous morphology strongly indicates that this material is still extremely two-dimensional.

Therefore, intercalating iodine into the BSCCO structure does not appear to significantly alter the extent to which the transition is broaden due to a magnetic field. In particular, it does not alter the angular independence of the dissipation for **H** and **J** in the **ab**-plane. This independence puts constraints on any theory that attempts to explain the anomalous magneto-resistance in the high T_c compound by forcing it to be insensitive to the physical spacing between the CuO_2 planes and to the magnitude and temperature dependence of the **c**-axis conductivity.

6.3 c-axis magneto-resistance

In addition to measuring the **ab**-plane magneto-resistance for **H** in the **ab**-plane, we also measured the **c**-axis magneto-resistance. To determine ρ_c we used the Montgomery method[61] contact configuration discussed in chapter 5. One potential problem with this technique is that the current paths are clearly non-ideal (i.e., current flows not only along the **c**-axis but also in the **ab**-plane) and therefore it is not immediately obvious that the Montgomery method analysis will properly separated the **ab**-plane magneto-resistance from the **c**-axis magneto-resistance. To determine whether this technique is valid or not, Briceño *et al.* measured[82] ρ_c in pristine Bi-2212 using the Montgomery method and compared the results to those obtained by using a symmetrical 4-probe "donut" geometry which insures that the transport current is parallel to the **c**-axis. They found that the Montgomery method does appear to properly separate the **c**-axis and **ab**-plane magneto-resistance. Hence, we have assumed that the Montgomery method is valid in the IBi-2212 compounds in the mixed state since it has been shown to be valid in the pristine material. Because of the added complexity of attaching contacts to the IBi-2212 samples (see chapter 5) we where not able to successfully produce the donut contact configuration in the IBi-2212 samples to test this directly. The main problem is that the added requirement of the additional Ag paint needed to insure mechanical rigidity of the contacts resulted in a relatively large separation between the "small" central voltage pad and the surrounding "large" current pad. As a result, even with no field one could see strong evidence for the contamination of the **c**-axis resistivity by that of the **ab**-plane for this "donut" geometry.

Fig. 6.3 (a) shows the **c**-axis resistivity of a pristine Bi-2212 sample for magnetic fields 0T, 0.5T, 3.5T, and 7T. Fig. 6.3 (b) shows the **c**-axis resistivity of an intercalated IBi-2212 sample for the same set of magnetic field intensities. For both sets of data the magnetic field is parallel to the **ab**-plane. Comparing Fig. 6.3(a) and 6.3(b) it

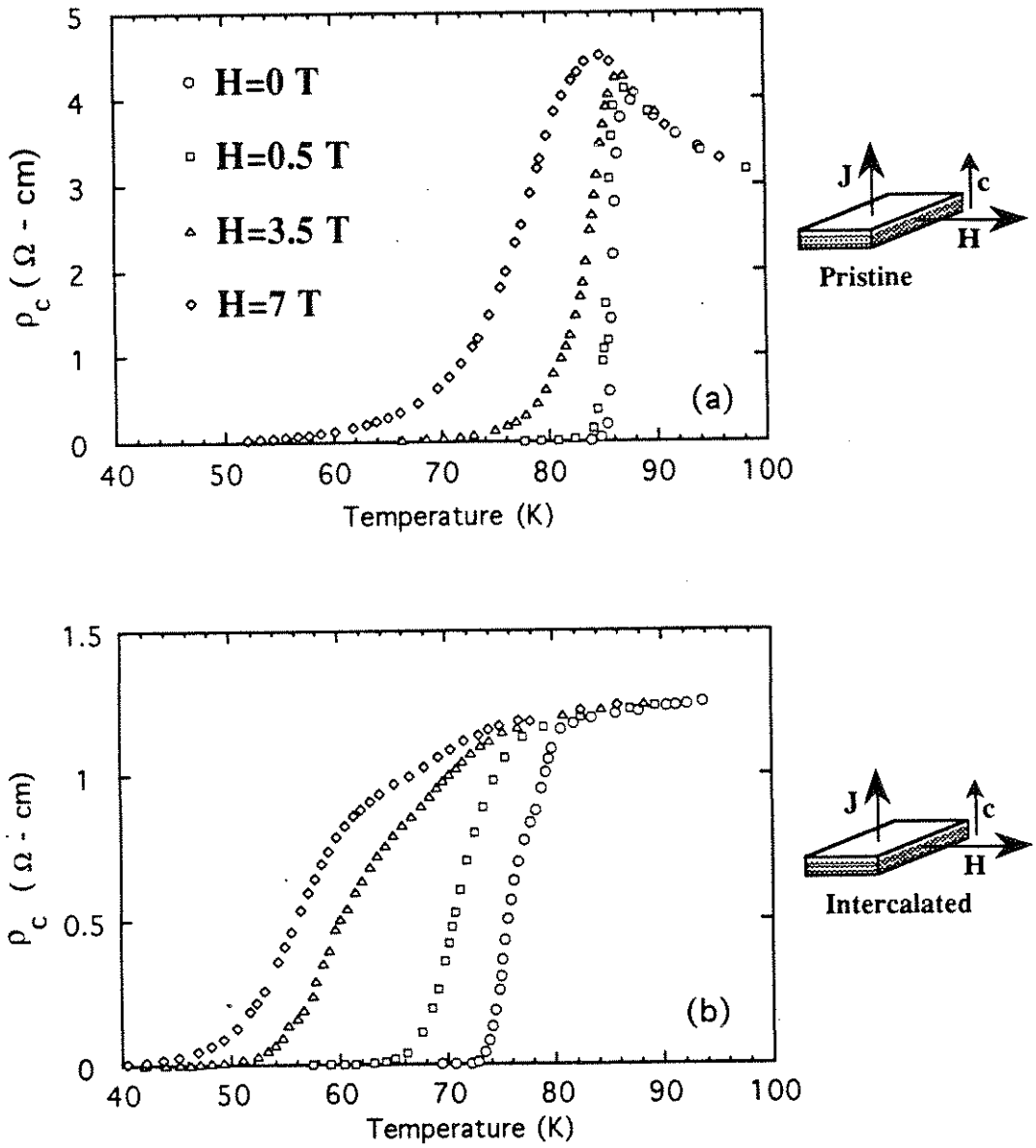

Figure 6.3 Temperature dependence of the out-of-plane resistivity ρ_c in (a) pristine Bi-2212 and (b) IBi-2212 for magnetic fields **H** of 0, 0.5, 3.5, and 7 T oriented in the **ab**-plane.

is clear that there is a significant difference between the pristine and intercalated samples for fields ≤ 3.5 T. In the pristine Bi-2212 data the curve for H = 0.5 T is essentially identical with that for H = 0 T. If we again compare the points at which the resistance has fallen to ~5% of the value at the onset of the transition, then the difference in temperature of these 5% points for H = 0T vs. H = 0.5 T is $\Delta T_{5\%} < 0.5$ K. In contrast to this, the IBi-2212 data show that the H = 0.5 T is significantly different from the zero field case with a difference in the 5% points of approximately $\Delta T_{5\%} \approx 5$ K. Therefore, one sees and increase in the width of the transition for H = 0.5 T of more than one order of magnitude when compared to the pristine material. For H = 3.5 T the intercalated sample still shows a significantly broader transition but the difference in the 5% points between the pristine and intercalated samples is now somewhat less than one order of magnitude. When the field is increased still further this difference essentially disappears with both materials showing a $\Delta T_{5\%} \approx$ 20-25 K for H = 7.0 T. This also may imply a very real difference in the field dependence at high fields (H > 7 T) in that for the pristine material the broadening is rapidly increasing with field whereas for the intercalated material it appears to be saturating. It is not clear, however, if for much larger fields the two sets of data would coalesce or if the pristine material would start to have broader transitions. One problem with interpreting the measured high field data is that the pristine material continues to show this normal-state-like upturn below the zero field onset temperature for these large fields. Since this tends to "pull" the whole curve up, it is not clear whether it is relevant to continue to look at the width as defined by the 5% points of the onset temperature or instead one should look at the 5% points of the maximum resistivity value. One fact is clear, however, and that is that the low field (H ≤ 3.5 T) behavior is significantly affected by the intercalation of iodine into the structure.

It has been proposed[88] that the dissipation in ρ_c for $\mathbf{H} \perp \mathbf{c}$ is due to the sliding of Josephson vortices along the **ab**-plane. In this picture each coreless Josephson vortex has

a width = $\Phi_o/H_{||}d$, where d is the distance between the superconducting layers and $H_{||}$ is the component of **H** parallel to the **ab**-plane. The model interprets the threshold behavior seen in the I-V curves[88] as being due to the Josephson vortices remaining fixed for low currents because of a pinning potential. As the current is increased one reaches the point where the Lorentz force on the vortex overcomes the defect pinning force and the vortices slide in the direction of the Lorentz force, i.e., in the **ab**-plane. Using this model one would conclude that one affect of the intercalation of iodine into BSCCO would be to decrease the width of the Josephson vortices by ~23% since the separation of the CuO_2 planes is increased by this amount. In addition the character of the Josephson vortex may be change because of a change in the Josephson coupling between the CuO_2 planes. Finally, the iodine may modify the distribution of pinning forces, especially in the neighborhood of the BiO bilayers. At present, this model is not developed enough to be able to determine whether the pronounced increase in the low field resistive broadening in IBi-2212 is consistently explained. However, these data do provide an additional constraint for future developments of this model.

Chapter 7

Introduction to Fullerene Section

7.1 Historical overview

In the spring of 1991 two pivotal papers[8,89] by Hebard *et al.* ignited research into an entire new class of superconductors based on the exotic form of carbon known as Buckminsterfullerene. Given that these materials have a high transition temperature of nearly 20 K and a host structure with extremely exotic properties, the Zettl group decided to dedicate a significant effort to explore these new intercalation compounds. In this historical overview I will describe some of the basic properties of the pristine and doped fullerenes which are directly relevant to the sections and chapters that follow.

Buckminsterfullerene (or bucky balls for short) were first produced by Kroto *et al.* in 1985.[90] Although several different allotropes exist, I will only be concerned with the most common form consisting of 60 carbon atoms in a soccer ball like structure. Fig. 7.1 shows the closed icosahedral cage of a C_{60} molecule which has a radius of approximately 3.55 Å. The structure consists of 12 pentagons and 20 hexagons with the carbons at the vertices and each carbon site being equivalent. Contrary to graphite which has only one type of in-plane bond, there are two types of C-C bonds on the surface of the ball corresponding to either double or single bonds.[91] The two bond lengths are nearly identical and both are comparable to the in-plane bond length in graphite. The single bonds form the perimeter of the pentagon faces whereas the perimeter of the hexagon faces consists of alternating single and double bonds.

At room temperature, pure C_{60} forms a face-centered-cubic (fcc) solid[92,93] with a cubic lattice constant of 14.2 Å. This puts the center-to-center nearest neighbor distance at ~ 10 Å and hence the rough C-C interball distance is ~ 3 Å. This large separation is comparable to the **c**-axis lattice constant in graphite thereby indicating that C_{60} is a true three dimensional van der Waals solid at room temperature and atmospheric pressure, the

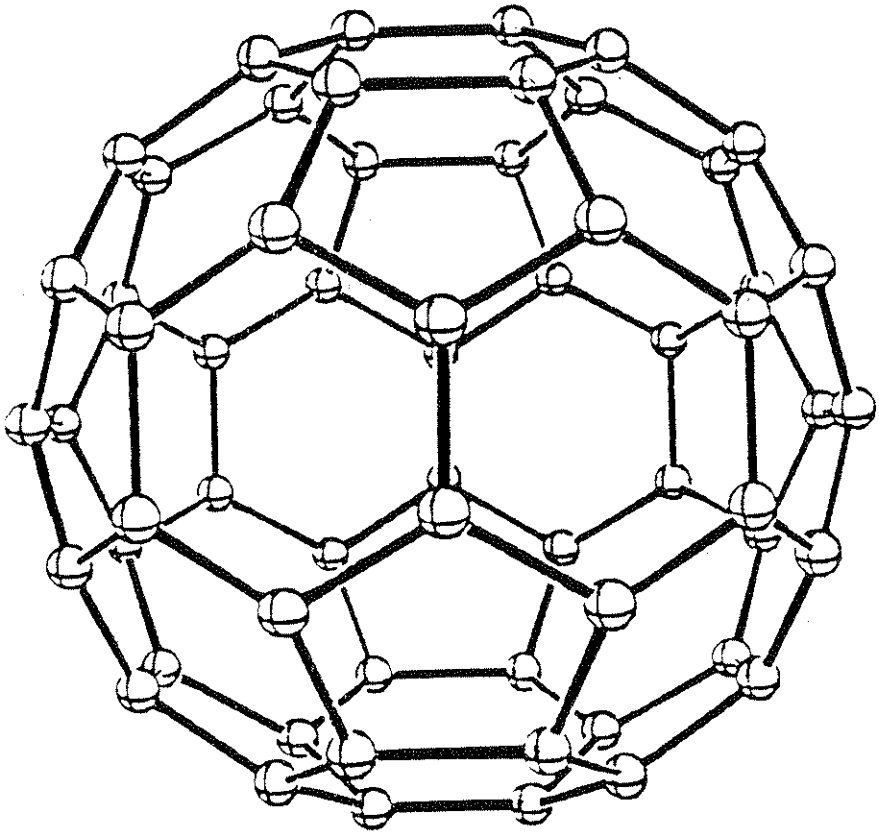

Figure 7.1 The icosahedral cage like structure of C_{60}.

only one known to exist under these conditions. Given the ease with which graphite intercalates this also suggests that solid C_{60} is an ideal 3-d intercalation host structure.

Nuclear magnetic resonance (NMR) measurements clearly indicate[94] that at T ≈ 260 K there is an abrupt decrease in the amount of dynamical disorder in solid C_{60}. Further studies have shown that there is a first order rotational ordering transition (ROT) which occurs at this temperature. For T > 260 K the balls freely rotate with a frequency of greater than 100 MHz. At T ≈ 250 K the balls lock into a nearly static rotationally ordered structure. This first order transition also results in a reduction of the lattice constant[92,95] of approximately 0.05 Å. This ordering transition is believed to be due to the presence of the two different types of C-C bonds on the C_{60} molecule. Since the single bonds, which make up the pentagonal faces, have a deficiency of electrons compared to the double bonds there is a net short-ranged intermolecular Coulomb interaction between the face of one ball and the double bonds on an adjacent ball. The theoretical[91] lowest energy configuration consists of the pentagon faces of any one ball facing only double bonds on all the nearest neighbor balls. There are, however, other configurations close in energy, e.g., hexagons facing double bonds, and therefore, below T ≈ 260 K, the balls actually ratchet between these different orientation. As the temperature is further lowered the balls begin to lock into a fixed orientation giving rise to a glassy transition which we have observed by looking at the elastic properties of a C_{60} crystal.[96]

In order for the balls to have nearest neighbor double bonds facing the pentagonal faces one finds that all the bucky balls are no longer orientationally equivalent. This results in a change in the crystal symmetry from fcc to simple-cubic (sc) because the basis has gone from a single ball to four balls with different distinguishable orientations.[91,97]

In an fcc close-packed structure there are three interstitial sites or voids; one octahedral and two tetrahedral. Using the diameter of the C_{60} molecule, 7.1 Å, one finds

that the radius of the larger octahedral site is $r_o \approx 2.06$ Å and that of the tetrahedral sites is $r_t \approx 1.12$ Å. It is within these sites the that intercalating alkali-metal resides resulting in the A_3C_{60} compounds (A = K, Rb, Cs, and mixtures of these). One problem with generating clean uniform samples of A_3C_{60} is that this is not the end phase of the intercalation process. If one intercalates with an alkali-metal to saturation then the resulting phase is A_6C_{60} which is an insulator with a body-centered-cubic (bcc) structure. The doping technique used to generate samples for this work will be given later.

The presence of the alkali-metal in the interstitial sites prevents the C_{60} molecules from freely rotating. In addition, since the C_{60} molecule does not possess the full cubic symmetry one finds that there are two inequivalent orientations for C_{60} which are presumably occupied with equal probability. Therefore the A_3C_{60} compounds are expected to posses a considerable amount of rotational disorder. The dynamical nature of this disorder has been studied by NMR[98] which indicates that in the K_3C_{60} system at room temperature the C_{60} molecules also ratchet back and forth between these two orientations. In addition, evidence for some smaller angle ratcheting is observed but this is not yet fully understood.

7.2 Materials techniques

7.2.1 Preparation

The production of pure C_{60} has increased dramatically since Kratschmer *et al.* first discovered[99] a method for producing and isolating macroscopic quantities of this exotic form of carbon. The C_{60} used in the experiments that follow was either isolated and purified by us or purchased as 99.9% pure C_{60} from Texas Fullerenes. The production and purification technique consisted of first producing the soot by burning a graphite rod in a carbon arc with an ambient atmosphere of 150-300 Torr of He. The soot was collected and dissolved in benzene or toluene which then formed a wine-red

solution. Only the fullerenes are soluble which allows the amorphous graphite also present to be removed by filtering the solution. This solution contains not only C_{60} but also C_{70} (~ 10%) and higher fullerenes (~ few %). A liquid chromatography technique[99] was employed to separate the C_{60} from the rest of the allotropes. The resulting pure C_{60} solution has a magenta color. If the solution is simply dried at ambient pressure then the resulting C_{60} powder also contains trapped solvents. To remove the solvents the residue is placed in a glass tube and heated to ~ 250 °C while being pumped on with a mechanical pump (~ few mTorr) for 15-20 hours.

7.2.2 Crystal growth

Crystals of solid C_{60} where produced via two different techniques. The first method discovered by Roman Mostovoy consists of re-solvenating the C_{60} in a mixture of 80% toluene and 20% hexane. This solution is then put into a glass flask and evacuated to a pressure of a few hundred Torr. The solution was then allowed to slowly evaporate over the period of approximately 24 hours. Crystals are formed at the boundary layer of the solvent and are left on the walls of the glass container as the solvent evaporates away.

One problem with the this crystal growth method is that toluene is found to be incorporated into the interstitial sites.[100] This problem of solvents trapped in the C_{60} compound has also been observed when crystals are grown using different solvents.[101,102] The presence of this intercalant makes it difficult to determine what properties are intrinsic to C_{60} and what properties are affected by the solvent. In order to produce crystals with a higher purity we developed a second method of crystal growth using vapor transport techniques.

For this technique, purified C_{60} powder was placed in a gold boat which was then placed in a Pyrex tube. Two different systems of vapor transport were used, a closed system

and an open system with Argon flow. In the closed system, Fig. 7.2(a), the Pyrex tube was flushed with Argon and then partially evacuated to about 100 Torr and sealed. In the open system, Fig. 7.2(b), there was a continuous flow of Argon across the C_{60} powder at a rate of about 0.01 liters per minute. In both cases the tubes were placed in a two-zone furnace with the powder side at T ≈ 650 °C and the other end of the tube at T ≈ 500 °C. Crystal growth took place over a period of several days. Two different crystal morphologies were obtained, block-like crystals with roughly equal lengths in all three dimensions, and plate-like crystals which were flat thin samples often in the shape of an equilateral triangle. The crystal structure of the block-like crystals was determined to be fcc with the proper lattice constant of 14.2 Å. The plate like structures had numerous stacking faults resulting in a staggering of fcc and hexagonal closed packed (hcp) regions. For the fcc regions the normal to the plate surface was the [111] direction whereas for the hcp regions this was the [001] direction using the standard basis for these two symmetries. Only the Argon flow method consistently produced samples large enough (≥ 0.5 mm on a side) to be used and of those only the block-like morphologies with the fcc structure were used in the transport measurements described below. Primarily these crystals were grown by Mike Fuhrer.

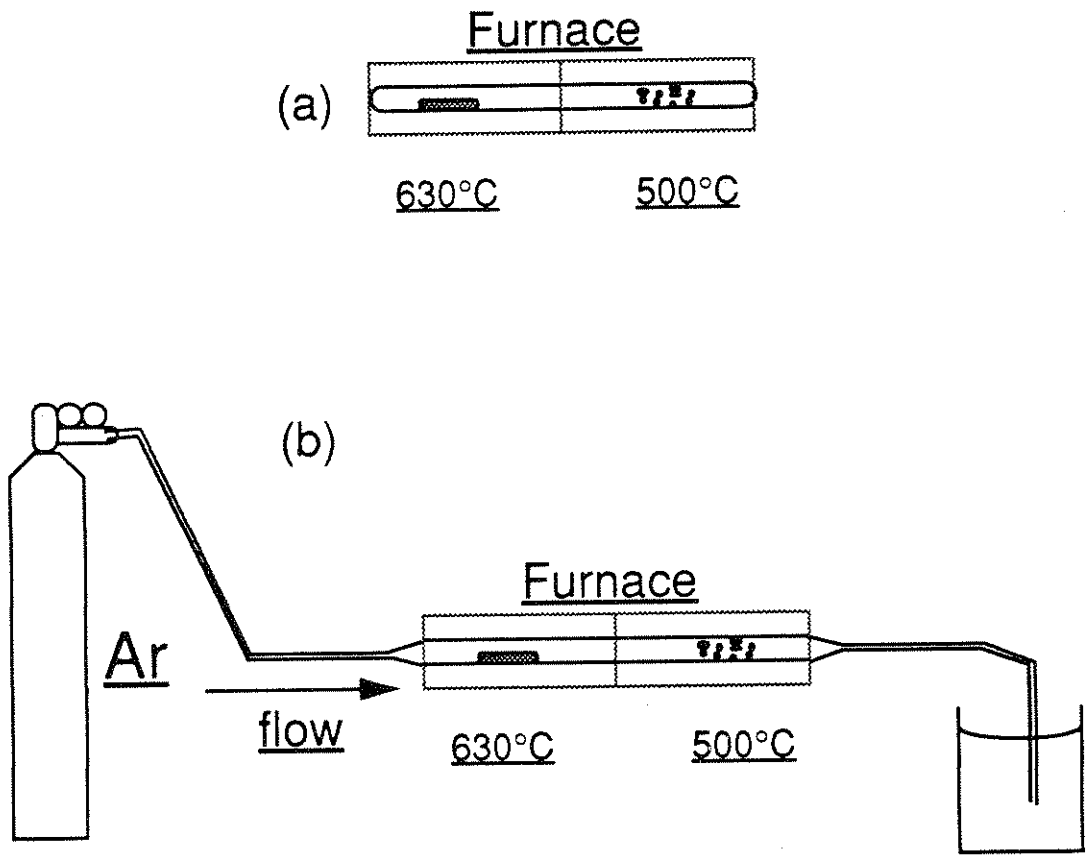

Figure 7.2 Schematic of two techniques used to grow C_{60} crystals. Both methods use a two-zone vapor transport. C_{60} powder is placed in the hot (~630°C) region and the crystals grow in the cooler region. (a) closed system, (b) open system with slow Ar gas flow to assist transport.

Chapter 8

Electrical Transport

8.1 Doping techniques

In the initial work done on the alkali-metal intercalated C_{60} compounds there were several techniques employed to obtain the properly doped superconducting phase of A_3C_{60}. There were two major challenges that had to be overcome: First, because the alkali-metals are so air sensitive, it was necessary to dope the samples in an inert atmosphere or a vacuum and then either remount the sample in an inert atmosphere glove-box for measurement or design the doping chamber such that the measurements could be performed *in situ*. If, after doping, the sample was exposed to air even for a few seconds it was usually destroyed due to the rapid oxidation of the alkali-metal. The second challenge was to determine a way to halt the doping when the superconducting A_3C_{60} phase was obtained. If allowed to continue unchecked, the doping would proceed past the A_3C_{60} phase to the A_6C_{60} insulating phase. Some of the first measurements[103,104] solved this problem by using stoichiometric amounts of alkali-metal and C_{60}. This, however, is very difficult since only small amounts of C_{60} were available and therefore extremely small amounts of alkali-metal had to be measured out, moreover the doping chamber had to be extremely clean since one did not want any of the metal to react with residual contaminants. A simpler method, and in fact the first method used,[8,89] was to monitor *in situ* the conductivity of a thin film sample and stop the doping when the conductivity reached a minimum. Since the only conducting phase found for the A_xC_{60} compound was for $x = 3$, one simply doped until a minimum in the resistivity was observed. The doping chamber consisted of a glass tube with wire feedthroughs. In addition, a temperature sensor was usually included so that the temperature dependence of the resistivity and the resistive superconducting transition could be measured. The main problem with this technique[105] was the poor quality of the films. The grain size

was only on the order of 60-80 Å which is only ~10 bucky balls between grain boundaries. Clearly the sample quality had to be improved before clean intrinsic parameters could be determined via transport measurements.

The method opted for by us was to dedicate our effort toward single crystals with the anticipation that these systems provide a much better chance of yielding unambiguous results. As mentioned previously, we found that it was possible to grow single crystals directly from solution if the solution was evaporated slowly enough under the proper conditions. Following this, much higher quality crystals were grown using the vapor transport technique. The doping chambers and techniques have evolved considerably since the those first used to dope the solution grown crystals. Hence I will restrict the discussion to the current apparatus and techniques used since these result in the best quality doped samples.

Fig. 8.1 shows the various elements of the doping chamber. The doping head is made from the nut of a Swageloc connector. Two holes are drilled through the nut as shown in Fig. 8.1(a). A copper sample-mounting-head shown in Fig. 8.1(b) is hard soldered into the end of a stainless steel (3/16" outer diameter (OD)) tube approximately 5" long. The sample-mounting-head is treaded nearly all the way through to allow a temperature sensing diode on a copper screw to be turned in so that good thermal contact can be made with the top surface where the sample is mounted. The stainless steel tube is placed through the large hole of the nut with approximately 2" sticking out the back. Through the small hole is placed a thin-walled 15 Ga. stainless steel micro-tube (McMaster-Carr) as shown in Fig. 8.1(c), the length dimensions are not critical. These two tubes are then hard-soldered in place. The entire head is sandblasted (if desired) and ultrasonically cleaned in acetone. If sandblasted, care must be taken to avoid damaging the sealing surface the of Swageloc nut which can not withstand an extended amount of exposure. The next step is to twist together four one-foot long insulated copper wires

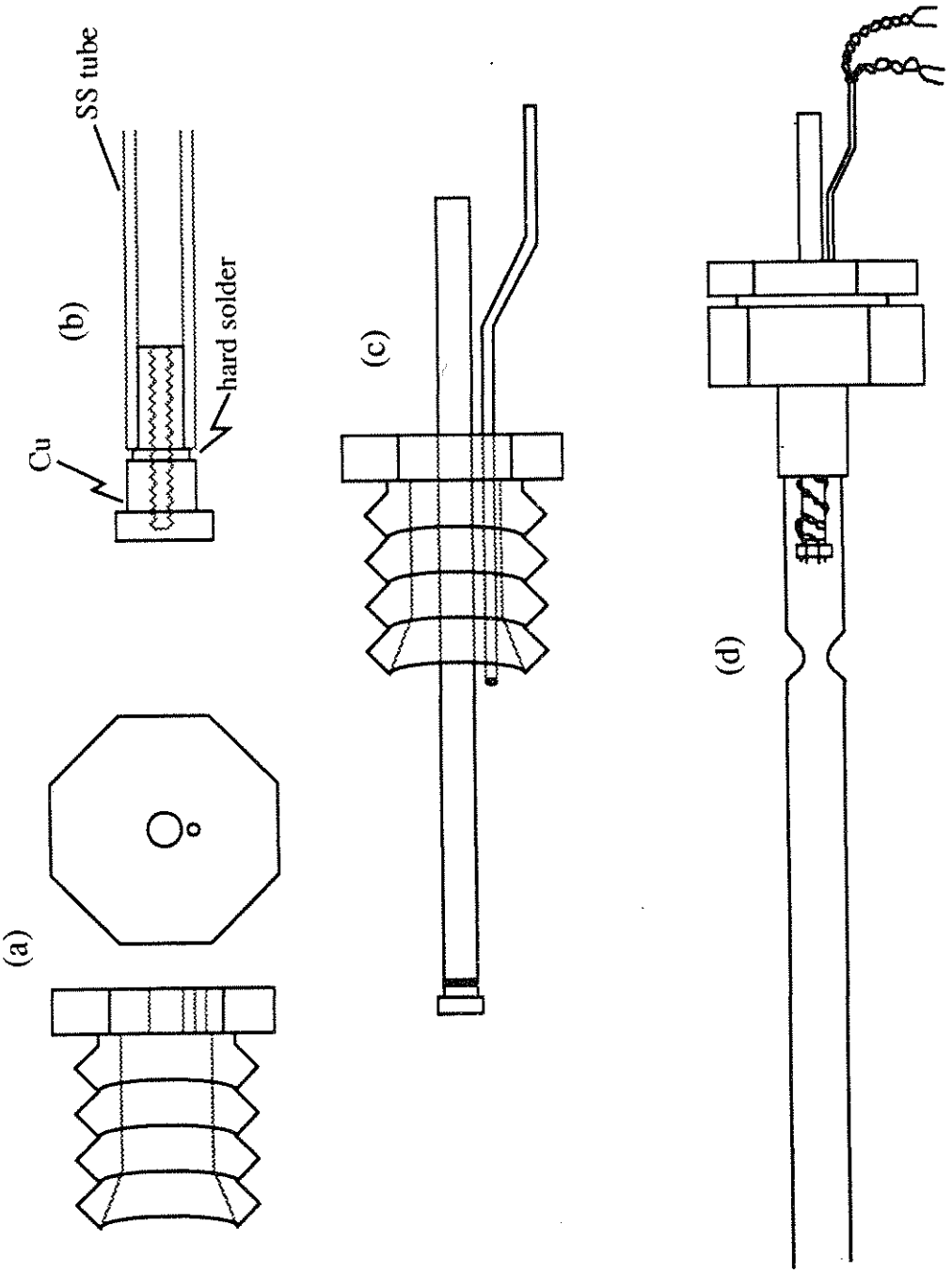

Figure 8.1 Various components used to make the doping chamber for intercalating A_3C_{60} samples. (a) Swageloc nut with feedthrough holes, (b) Copper sample mounting head, (c) main head of the doping apparatus with thin tube for electrical feedthroughs, (d) completed doping chamber including the necked down Pyrex tube with glass-to-stainless seal.

and feed them through the small tube. The outer part of this tube is then sealed with Torr Seal (Varian) to provide a good vacuum seal. Note that this end is kept several cm away from the nut since the nut will be heated to ~250 - 300 °C during the doping procedure and the Torr Seal must be cool so that it does not outgas into the tube. Wind the copper wires around the large stainless tube and either tie them off at the sample mounting head or bond them in place with Insulate Ceramic Paste (Sauereisen). The very ends of these wires have the insulation removed so that jumper wires can easily be attached from them to the sample. A 12mm outer diameter Pyrex tube with a glass-to-stainless joint and a 1/2" OD stainless tube section make up the other end of the doping chamber. The Pyrex tube should be necked down to an inner diameter of a little less than 3/16" a distance of 1/2" - 3/4" down from where the sample will sit when the Swageloc seal to the stainless steel section is made. Fig. 8.1 (d) shows what the finished doping chamber should look like. The Pyrex tube needs to extend at least 5" beyond the point at which it is necked down.

The next step is to attach 4 annealed gold wires to the C_{60} crystal using silver epoxy (Epo-tek H20E, Epoxy technology). The sample must be heated to ~150 °C for a minute or two so that the Ag epoxy hardens enough to support the sample. It was found that Ag epoxy works better for electrical contact than Ag paint, so don't use Ag paint to attach to the sample unless there is a specific reason. It is easiest to use Ag paint for attaching the wires that come from the sample to a Sapphire substrate and then from the substrate to the four feedthrough wires on the sample mounting head. The sapphire substrate should be bonded to the sample mounting head with either Ag paint or Ag epoxy, with Ag paint being easier since it will dry at room temperature. The reason this is desirable is that C_{60} is known[106-110] to absorb O_2 into the interstitial sites when exposed to air. This process is essentially reversible provided the sample is not

maintained for long periods at elevated temperatures in the presence of oxygen. Therefore, as a precaution one should try to avoid heating the sample in air.

With the sample mounted and the Swageloc seal made to the stainless/glass tube, the next step is to pump out the tube with a good pump ($<1x10^{-6}$ Torr). A turbo-pump works best since there is no oil to worry about but a diffusion pump will also work provided a cold trap is used. You do not want any oil on the surface of the sample which would impede the intercalation into the C_{60}. After you are sure the Swageloc is making a good seal then wrap the glass tube and nut (but not the small wire feedthrough tube) with heater tape (Briskheat Co.) and heat to ~150-200°C and continue to pump for 2-10 hrs. Then cool and vent the tube and place it in the inert atmosphere glove-box with a plastic tube and a simple teflon valve. Take a small 3/16" OD glass tube with an etched mark ~ 1 cm from the end and press it into the alkali-metal to fill approximately 0.5 cm with metal. Place this in the end of the doping tube and snap it off at the etch mark. The neck in the doping tube will prevent it from sliding all the way down and hitting the sample. Place the plastic tube and closed value on the doping tube and remove from the glove-box. Attach it to a pump and evacuate and seal the tube. Once it's sealed you can heat the alkali-metal gently to react away any contaminants in the tube. The sample is now ready for intercalation.

The intercalation process consists of a repetitive dope and anneal cycle. Using two separate heater tapes, heat the sample to ~ 220-260°C and then monitor the resistivity while increasing the temperature of the alkali-metal zone. Typical values for the metal zone temperature are 150-200°C. When the resistance reaches a minimum, typically 1/2 - 1 1/2 hours, cool the metal zone and anneal the sample for 4-10 hrs. Then increase the temperature of the metal zone back to the original doping temperature and dope again until a new minimum in the resistivity is reached. Cool the alkali-metal zone and anneal the sample again. Repeat this procedure until the resistivity can no longer be reduced. After

the final anneal, cool the sample back to room temperature slowly (1-2 hours). This is especially important for the K_3C_{60} material since this compound is believed[111] to phase separate at T_{ps} ~100-150°C. Above T_{ps} for $x < 3$, A_xC_{60} is believed to be composed of both K_1C_{60} and K_3C_{60} phases, whereas below T_{ps} it phase separates into αC_{60} and K_3C_{60} where αC_{60} is pure C_{60} with less that 1% potassium. On cooling the sample, this phase separation results in anomalous resistivity readings which can either become very noisy or show discontinuities in this temperature range. Slow cooling prevents this phenomenon from permanently degrading the sample. For Rb doped C_{60} this phase separation is not believed to exist (at these temperatures); however, it was also found that if the sample is cooled too quickly the temperature dependence of the resistivity can also be degraded. Therefore, these samples are also cooled slowly from the doping temperature to room temperature.

8.2 Temperature dependent resistivity

The very first measurements[8,89,105,112] on the resistivity and its temperature dependence for the doped fullerenes were performed on thin films of K_3C_{60}. With the film samples the lowest value obtained for the room temperature resistivity was ~2.2 mΩ-cm. This relatively large resistivity has been interpreted[105,112,113] as being due to the granular nature of the material in these film samples. This granularity also manifests itself strongly in the measured[105] temperature dependence of the resistivity shown in Fig. 8.2 (a). The data show an anomalous temperature behavior with a semiconducting-like upturn for low temperatures. Palstra *et al.* show through a series of experiments that this upturn is most likely due to granularity effects. A significant effort was put in by several other groups to try to grow films epitaxially so that high quality, large grain size films could be produced, intercalated, and examined. This has proven very difficult and has only been somewhat successful very recently.[114] Rather than use films, the obvious

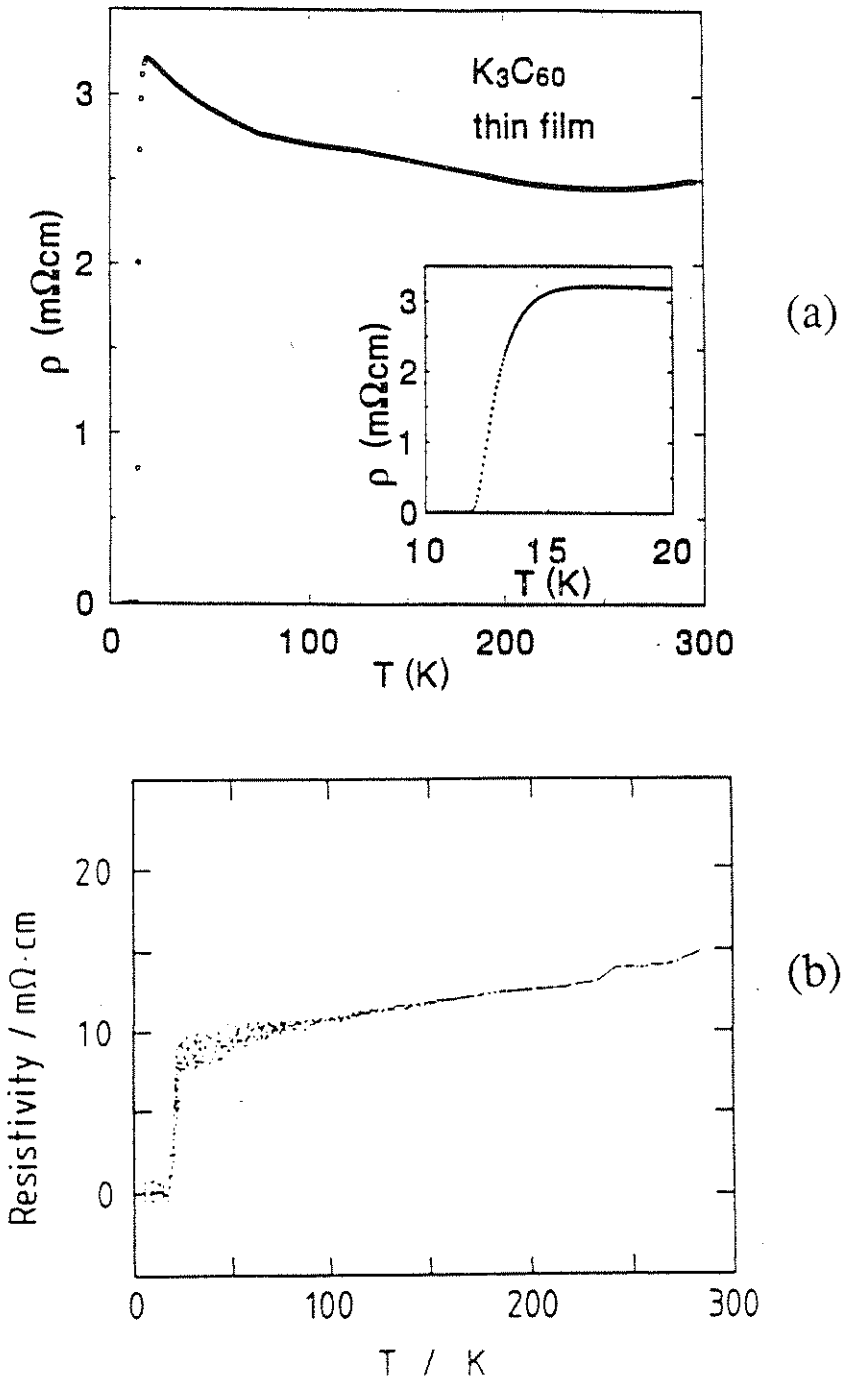

Figure 8.2 Temperature dependence of the electrical resistivity in K_3C_{60} samples. (a) from ref. [105] using C_{60} thin films, (b) from ref. [115] using C_{60} crystals grown in a CS_2 solution.

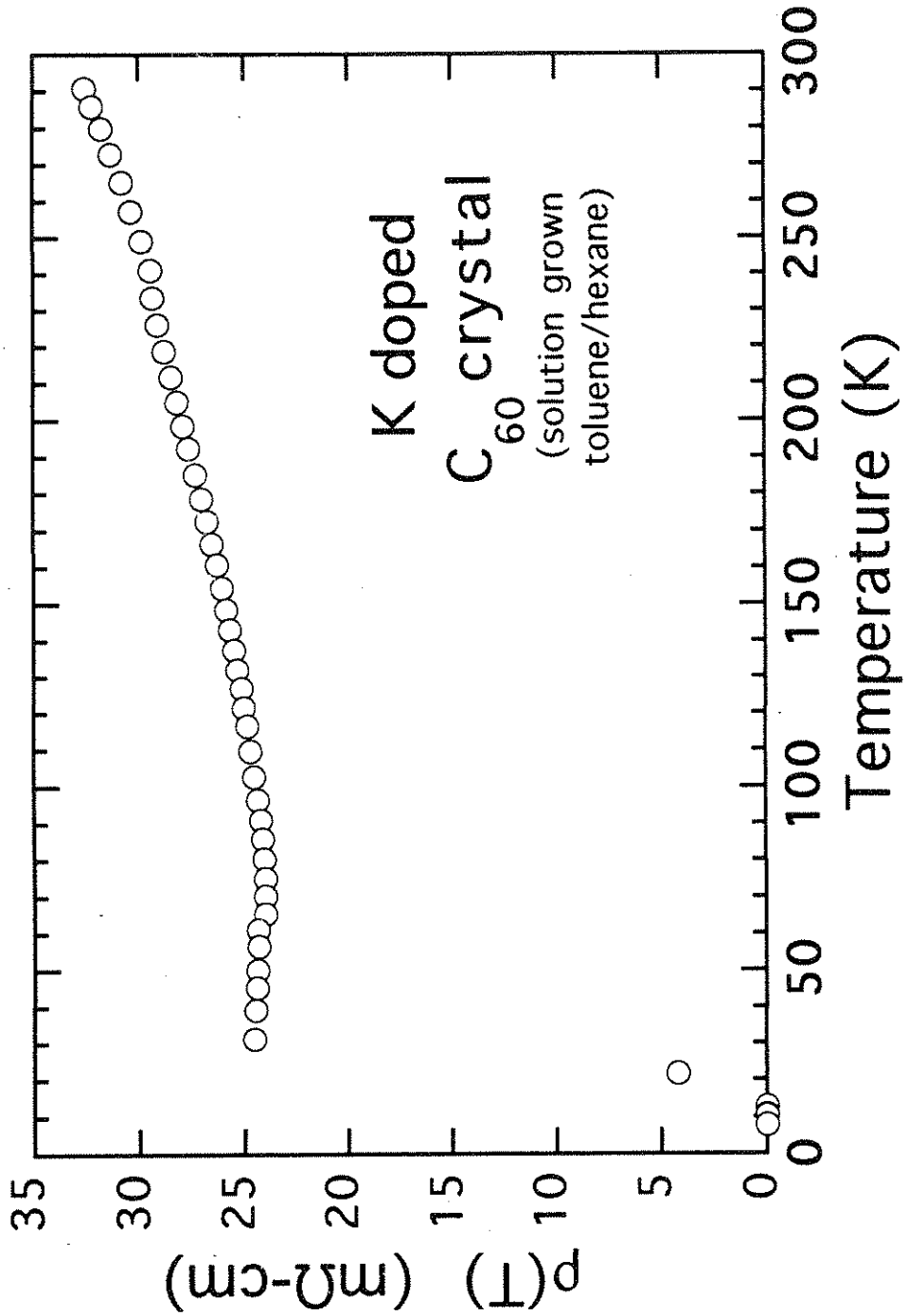

Figure 8.3 Temperature dependence of the electrical resistivity in a K_3C_{60} sample where the original C_{60} crystal was grown from a solution of toluene and hexane. The original crystal is known to have solvents incorporated into the interstitial sites.

other choice was to try to intercalate crystals of C_{60}. Maruyama *et al.* conducted resistivity measurements[115,116] on C_{60} samples that where originally grown from a solution of CS_2 and then intercalated with potassium. Their results are shown in Fig. 8.2 (b). Although these data are at least starting to show a metallic-like behavior, the temperature dependence still remains anomalous. In addition, structural studies on the starting crystals showed that they were not fcc as in pure C_{60}, but instead they had an orthorhombic structure. It was subsequently shown[117,118] that this was due to the incorporation of CS_2 into the interstitial sites.

The results of Maruyama *et al.* are somewhat similar to the results we obtained for crystals that were grown in a toluene/hexane solution. Fig. 8.3 shows the temperature dependence of the resistivity for a solution grown C_{60} crystal doped with potassium. As with the Maruyama *et al.* data, the rough behavior is metallic-like with a positive $d\rho/dT$. The room temperature resistivity is approximately one order of magnitude greater than the best film samples and the ratio of the residual value to room temperature value the is very large, ~ 0.75. Unfortunately, starting crystals grown by this technique also incorporate significant amounts of solvents (mainly toluene) into the interstitial sites. It is interesting to note our work and the work of Maruyama *et al.* show that even with the solvents initially present, these crystals can still be successfully intercalated with alkali-metals to become superconductors. On the other hand, it is also clear that the presence of the solvents in the original C_{60} crystal makes it nearly impossible to separate the intrinsic properties from those which have been modified by the solvents.

To clarify this picture, single C_{60} crystals grown by vapor transport were also doped with potassium and rubidium. For the best of these samples, the magnitude of the room temperature resistivity is comparable to the best values obtain in thin films. Fig. 8.4 shows the temperature dependence of the normalized resistivity for a K_3C_{60} sample. There are two important observations to make about these data: First, the width of the

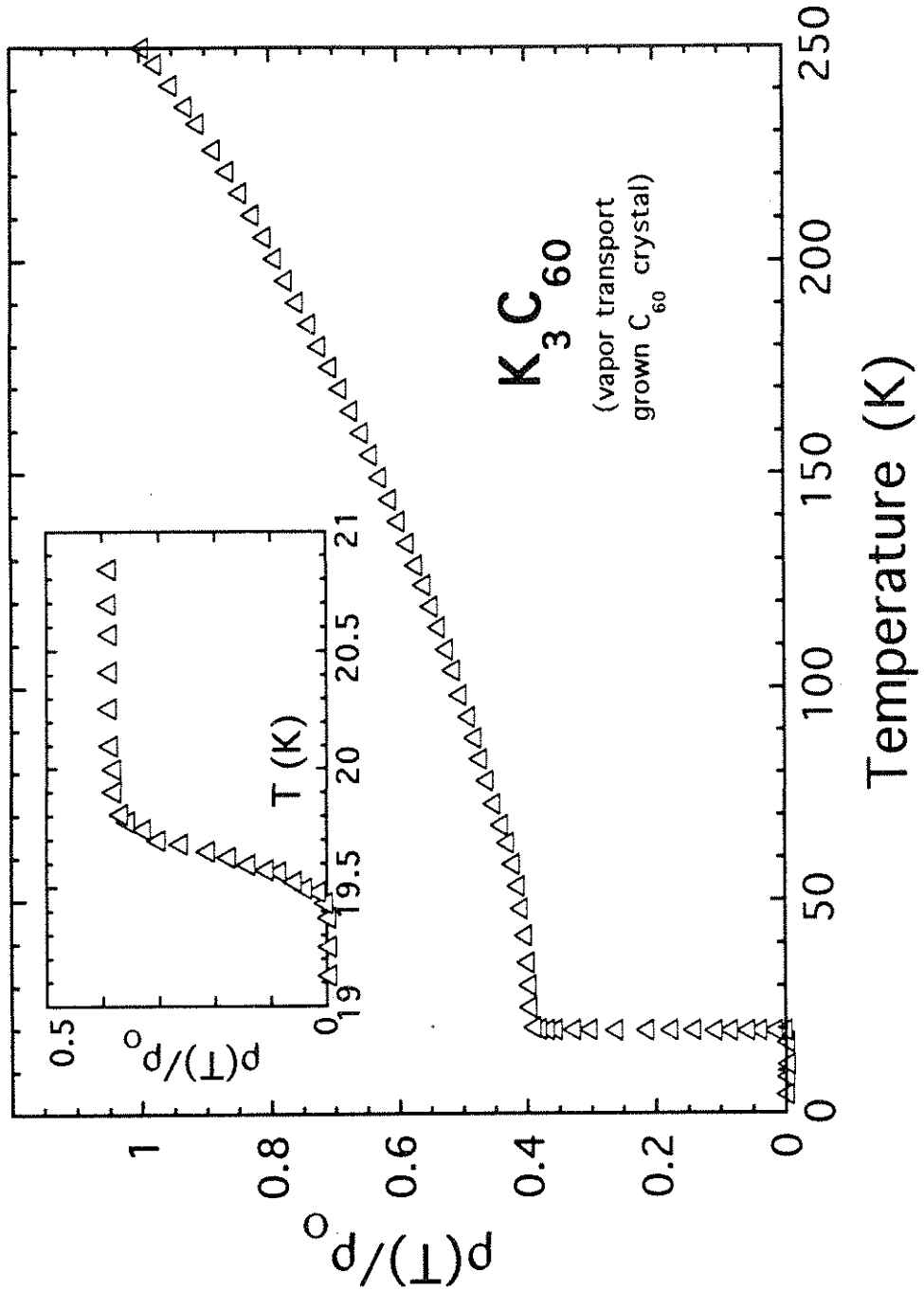

Figure 8.4 Normalized dc electrical resistivity of single crystal K_3C_{60}. The ρ_o is the resistivity at T = 250 K. The inset shows the $\rho(T)$ behavior near the superconducting transition temperature T_c = 19.8 K.

superconducting transition is very narrow, on the order of $\Delta T_c \approx 0.2$ K, which is significantly better than what had previously been obtained on solution grown crystals ($\Delta T_c \approx 2$ - 5 K) or films ($\Delta T_c > 10$ K). Second, the value of the "residual" resistivity is still quite large, on the order of 1/2 the value at $T \approx 250$ K. This large residual resistivity has been found in all samples of both Rb and K doped C_{60} provided they are somewhat near optimal doping. Samples which differ in $\rho(T \approx 250\ K)$ by more than a factor of 5 still have residual resistivities which are given by $\rho(0) \approx 0.5 * \rho(250K)$. This anomalously large and sample independent residual resistivity behavior will be addressed further in the next chapter.

Now that samples with sharp superconducting transitions and more smoothly varying $\rho(T)$ have been obtained, the obvious question is whether the true intrinsic temperature dependence of the resistivity has been reached. To test this, we first consider Mattheissen's rule which states that given several different scattering mechanisms, the measured resistivity is simply the sum of the resistivities one would have from each individual mechanism. This rule is based on the relaxation-time approximation with the added restrictions[119] that the scattering time τ be independent of $\mathbf{k}$ and the scattering mechanisms do not significantly influence each other. Since we are only concerned with the temperature dependent part we formulate Mattheissen's rule as

$$\rho_{measured} = \rho_o + \rho_{intrinsic}(T) \qquad (8.1)$$

The value of ρ_o is obtained by using a linear extrapolation to zero temperature of the data above the superconducting transition temperature. In addition, because of difficulties in determining the exact magnitude of the resistivity due to non-ideal geometries we use the normalized resistivity data. Fig. 8.5 shows the temperature dependence of $\rho_{intrinsic}$ defined by Eq. (8.1) for several samples of both (a) K doped and (b) Rb doped C_{60}. For

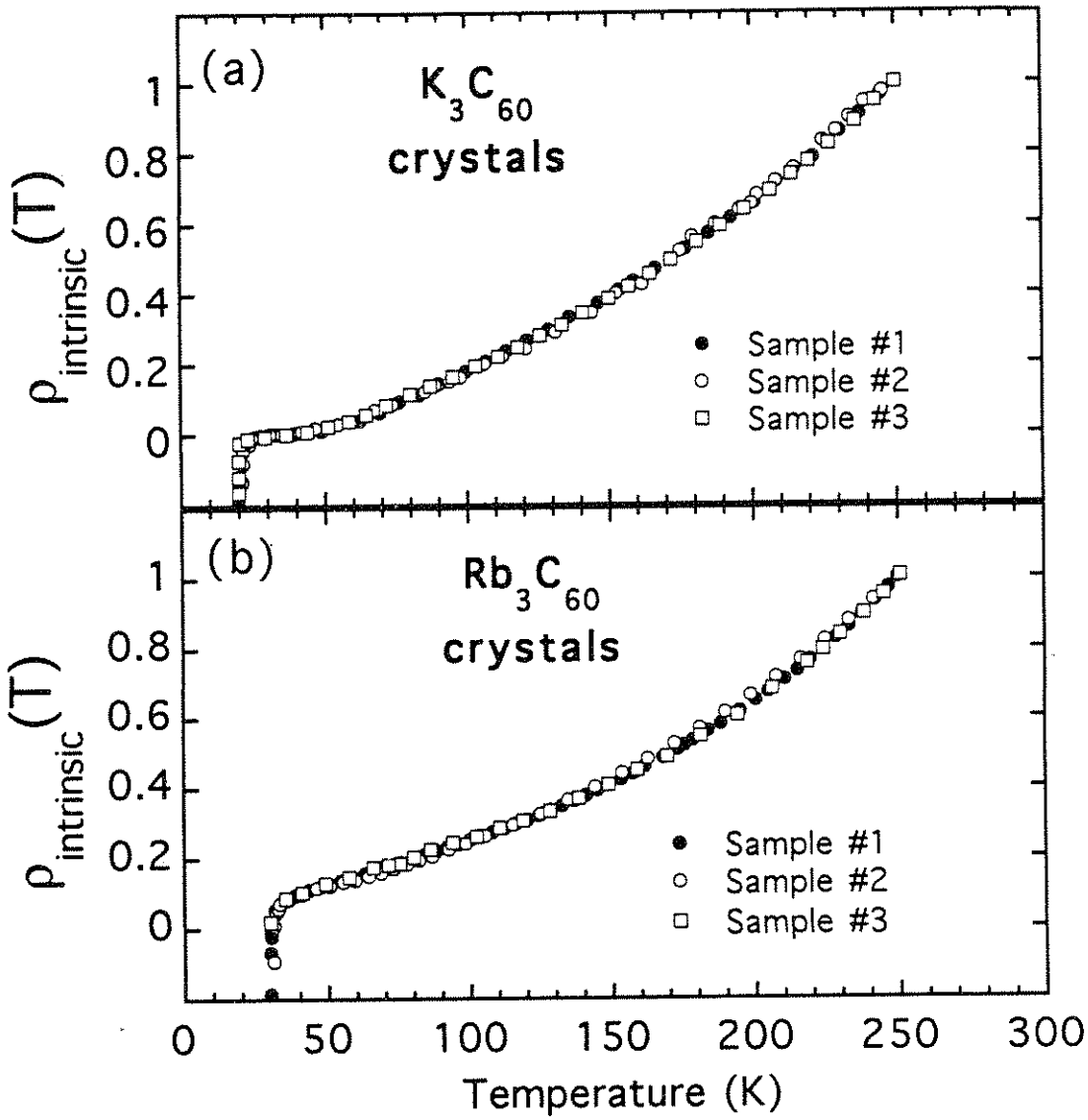

Figure 8.5 Normalized intrinsic resistivity below 250 K for several samples of (a) K_3C_{60} and (b) Rb_3C_{60}. A linear extrapolation was used to determine the residual zero-temperature resistivity which was then subtracted from the raw data to give the intrinsic resistivity.

each compound, all of the different samples show the same temperature dependence which strongly indicates that this is the true intrinsic temperature dependence of the resistivity. For temperatures greater than 100 K, both compounds have similar temperature dependences with $\rho_{intrinsic}(T) \sim \alpha T^2$. In the K_3C_{60} system this continues to very high temperatures,[120] T ~ 650 K, whereas for the Rb_3C_{60} compound the resistivity begins to saturate at T ~ 500 K. The presence of a T^2 - like dependence could be evidence for a novel scattering mechanism, e.g., electron-electron scattering.[121] However, the combination of high and low frequency phonons may also mimic[122] this behavior. This dependence will be addressed in detail in the following chapter. Careful examination of the low temperature data shows that the two compounds have different temperature dependences for T < 50K. In the K_3C_{60} compound the resistivity is very flat and does not change much with temperature whereas for the Rb_3C_{60} compound the resistivity is still falling with temperature. At present this phenomena is not well understood. The reproducibility of $\rho_{intrinsic}(T)$ between several samples with different magnitudes of ρ is consistent with the picture that these materials are granular metal conductors with a large volume fraction of metal. It has been shown[113,123] that the variation of the resistivity with doping concentration in the A_xC_{60} compound (A = K, Rb) is consistent with the picture that the A_3C_{60} phase is a line-phase and that the resulting material is a granular metal conductor with A_3C_{60} being the metallic phase and the pristine C_{60} being the insulating phase. In general, for granular metals the overall electrical properties depend critically on the volume ratio of the metal and insulator grains. For granular metals[124,125] with a high volume fraction of metal the temperature dependence of the resistivity is essentially the same as that of the bulk metal. However, it differs in two important respects. First, the size of the resistivity can be larger than the pure bulk value by several orders of magnitude due to the electron scattering effects at the grain boundaries. This is commonly observed in the A_3C_{60} compounds where samples

with similar sharp (< 1 K) superconducting transition widths can have room temperature resistivities that differ by a factor of five. Second, the temperature coefficient of the resistivity (TCR) or equivalently the relative slope defined as $\alpha_R = 1/\rho * d\rho/dT$ can be smaller than that in the pure bulk system. As the volume ratio of the metal approaches unity the value of α_R should approach that of the pure metal. Therefore, reproducibility in the normalized temperature dependent part of the resistivity strongly suggests that these samples are in the large volume-fraction-of-metal limit and hence the measured temperature dependence is intrinsic.

8.3 Resistive anomaly

Even though the volume fraction of metal is high in these nearly optimally intercalated compounds, the directly measured resistivity still remains quite large (~3-5 mΩ-cm @ room temperature) compared to "good" metals which typically have room temperature resistivities on the order of a few μΩ-cm. Much of this is due to the fact that these compounds are granular and still contain small amounts of pristine C_{60} which increase the resistivity through defect boundary scattering. In addition to increasing the resistivity, these small regions of C_{60} can also affect the measured transport behavior in another way. To see how this works we must first discuss the rotational ordering phase transition in the pristine C_{60} system.

The C_{60} molecule is very nearly spherical and the bonding between adjacent balls is quite weak, essentially a van der Waals type bonding. Still, it is quite surprising to find that at room temperature the balls freely rotate with an orientation that is completely uncorrelated with its neighbors. In fact, initially this lead to a difficulty in proving the cage-like structure of C_{60} because this rapid rotation of the balls resulted in x-ray diffraction analysis detecting only a relatively smooth even shell of charge at the radius of the ball. Hawkins *et al.* were able to attach an osmium compound to the bucky balls[126]

which prevented their rotation and allowed the first determination of the C-C bond lengths.

Although C_{60} behaves somewhat like a uniform spherical shell of charge, the underlying icosahedral structure eventually manifests itself through a freezing of the orientation of the balls at T ≈ 260 K, referred to as a rotational ordering transition (ROT). This was first conclusively shown in a differential-scanning-calorimetry measurement[93] and has subsequently be observed in numerous experiments including, NMR[127], Raman[128,129], elastic moduli studies[96,130,131], neutron scattering[132,133] and x-ray studies.[92,134] Of relevance to the discussion here is that this ROT is a first order transition with an accomanpying discontinuous change is the lattice constant. Fig. 8.6 taken from ref. [92] shows the temperature dependence of the lattice parameter with a distinct discontinuity of about 0.35% at T ≈ 260 K. Thus for our samples of A_xC_{60} with $x < 3$ one might expect this discontinuous change to result in a sudden change in the stain fields in the sample which could then couple to the resistivity.

For our best samples, where best is defined as those samples with the lowest measured value of room temperature resistivity and/or those with very narrow superconducting transition widths (≤ 0.3 K) we found no evidence for a resistive anomaly at this ROT temperature. On the other hand, many other samples did show a definite discontinuity in ρ(T) at T ≈ 260 K. The main part of Fig. 8.7 shows the normalized resistivity data for two Rb_3C_{60} samples in which one sample clearly displays a discontinuity whereas there is a lack of any anomalous behavior for the other "better" sample. The direction of the jump was generally that shown in Fig. 8.7, i.e., positive with increasing temperature, but some samples did show a jump which went down instead of up. The size of the jump varied from sample to sample with samples which were obviously underdoped (not doped to minimum in ρ) showing the largest discontinuities. Even for the same sample the size of the jump was found to vary from

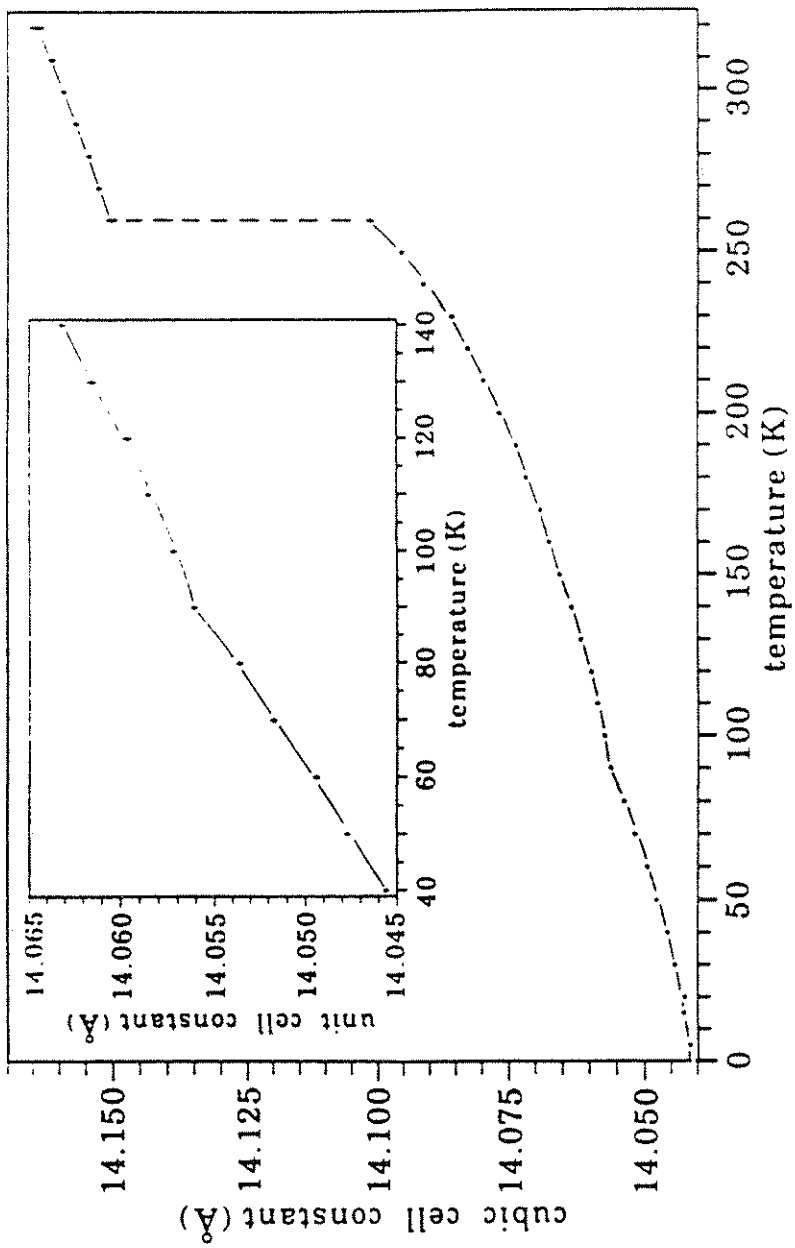

Figure 8.6 Temperature dependence of the cubic lattice constant in pristine C_{60} taken from ref. [92]. The discontinuity at 260 K is due to the first order rotational ordering phase transition.

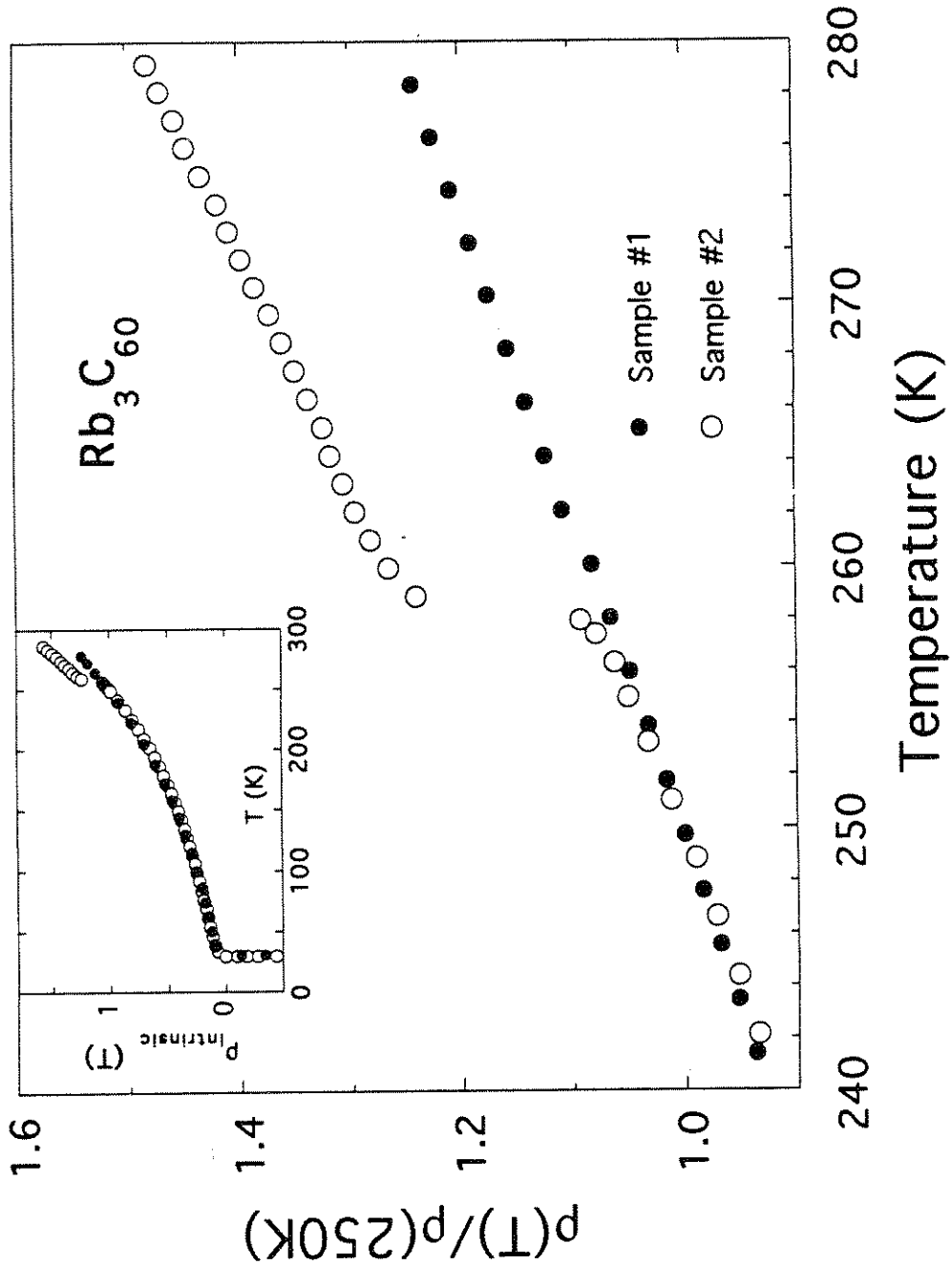

Figure 8.7 Normalized temperature dependence of the electrical resistivity near 260 K for two different Rb_3C_{60} samples. One sample clearly shows discontinuous behavior. The inset shows the temperature dependence of the intrinsic resistivity (see text) for these same two samples.

one temperature sweep to the next. Generally, after several temperature sweeps the magnitude and sign of the discontinuity would stabilize. If the sample was then further doped and annealed the size of the anomaly was generally reduced. It is important to note that the presence of the anomaly **does not** affect the normalized temperature dependence of the resistivity away from this transition. The inset to Fig. 8.7 shows the full temperature dependence of the normalized intrinsic resistivity, as defined in Eq. (8.1), for these same two samples. There is no detectable difference in $\rho_{intrinsic}$ (T). We conclude from this that the presence of this anomaly is due to a stain effect caused by the discontinuous change in the lattice constant in the small regions of remaining undoped C_{60}. This results in an offset in the measured resistivity but does not affect the general form of the temperature dependence. Further conclusive evidence that this anomaly is due to pristine C_{60} comes from pressure studies given in the next chapter.

In conclusion, by working with single crystals we have been successful in producing high quality superconducting samples. Theses samples have very narrow transition widths and a temperature dependent resistivity which has been shown to be intrinsic. Both Rb_3C_{60} and K_3C_{60} display a temperature dependent resistivity of the form $\rho(T) = \alpha + \beta T^2$ for $100 < T < 450$ K (and K_3C_{60} going up to 650 K). With these samples it is now possible to probe the intrinsic parameters in the materials, e.g., the electron-phonon coupling constant and the Hall coefficient, with an eye toward resolving the issue of what allows these compounds to have such relatively high superconducting transition temperatures.

Chapter 9

Pressure effects

9.1 Introduction

Numerous pressure effect studies have been performed on pristine C_{60} and the A_3C_{60} compounds. For a cubic material, the bulk modulus is defined as:

$$\begin{aligned} B &= -V\frac{\partial P}{\partial V} \\ &= -\frac{1}{3}\frac{\partial P}{\partial \ln(a)} \\ &= -\frac{1}{3}\frac{1}{\kappa} \end{aligned} \tag{9.1}$$

where P is the pressure, V is the volume, a is the cubic lattice constant, and κ is the linear compressibility. In pristine C_{60} the bulk modulus was measured[135] at room temperature and found to be B = 145 kbar. This gives a linear compressibility of $\kappa = 2.3 \times 10^{-3}$ 1/kbar. This value is comparable to the **c**-axis compressibility for graphite which is $\kappa \approx 1 \times 10^{-3}$ 1/kbar. In graphite one typically finds[136] a stiffening in the crystal upon intercalation. As one might expect, the intercalated compounds of C_{60} are somewhat stiffer than pristine C_{60} possibly[137] due to the additional ionic character of the bonding. One finds[138] $\kappa = 1.20 \pm 0.09 \times 10^{-3}$ and $1.52 \pm 0.09 \times 10^{-3}$ 1/kbar for K_3C_{60} and Rb_3C_{60}, respectively. No direct measurements of the temperature dependence of the bulk modulus have been reported for either pristine C_{60} or the A_3C_{60} compounds. The bulk modulus can be related however to the Young's modulus (see Appendix C) which has been measured[96,130] for C_{60} crystals. Unfortunately both of these measurements were on crystals which were grown from a solution and therefore had solvent which was incorporated into the crystal structure. An attempt was made to desolvenate the samples

by heating them to ~150-250°C which resulted[130] in a significant change in the detailed temperature dependence of the Young's modulus (Y). After heat treating the temperature dependence of Y was roughly linear with a slope of ~ 7.5-11% per 100 K. Evidence of the rotational ordering transition was clearly seen as well as a glassy transition which occurred between 80-150 K. The temperature dependence of Y below this glassy transition appears to be somewhat sensitive to the solvent used to grow the crystals and the heat treatment employed. No measurements have yet been reported for the Young's modulus in the alkali-metal doped C_{60} compounds. Finally, the thermal expansion coefficients for K_3C_{60} and Rb_3C_{60} have been measured[139] from room temperature to ~ T_c and they are highly linear over this entire range with a slope defined as $d\ln(a)/dT$ given by 2.4×10^{-5} and 3.05×10^{-5} K^{-1} for K_3C_{60} and Rb_3C_{60}, respectively.

In addition to these standard pressure related intrinsic parameters one also finds a strong pressure dependence of the superconducting transition. Fleming *et al.* initially found[137] a nearly linear relation between the room temperature lattice constant and T_c for several A_3C_{60} and $A_xB_{3-x}C_{60}$ compounds where A = K, Rb and B = K, Rb, and Cs. The slope was given by $\Delta T_c/\Delta a$ ~ 50 K/Å with T_c increasing for increasing lattice constant. This dependence on lattice constant can be thought of as a steric or "chemical" pressure dependence. Several groups[140-144] have also measured the dependence of T_c on externally applied pressure. As expected a negative dependence on pressure is found with dT_c/dP ~ -0.78 and -0.97 K/kbar for K_3C_{60} and Rb_3C_{60}, respectively. This pressure dependence is more that one order of magnitude greater than what is found in the A15 compounds (which have similar T_c's). For example[141] Nb_3Sn which has a T_c = 16.9 K has a pressure dependence of dT_c/dP = -0.022 K/kbar. On the other hand, some of the cuprates with comparable T_c's have pressure dependencies which approach[141] the value found in the intercalated fullerenes.

Contrary to Fleming *et al.* the data taken by varying the externally applied pressure show that the T_c vs. lattice constant relation is not truly linear. Surprisingly, however, a very linear relation has been found[145] between T_c and the calculated density of states at the Fermi level, $N(\varepsilon_f)$. In this picture the difference in chemical species of alkali-metal atoms has little affect on the electronic structure. Instead, the difference in $N(\varepsilon_f)$ between K_3C_{60} and Rb_3C_{60} is due to the increased lattice constant which reduces the electronic overlap, narrowing the bandwidth and thereby increases the density of states. In the standard weak coupling BCS model T_c is related to $N(\varepsilon_f)$ through

$$T_c = 1.14 \langle\omega\rangle \exp\left(-1/N(\varepsilon_f)V\right) \tag{9.2}$$

where $<\omega>$ is the relevant frequency and V is the coupling strength. This obviously does not have T_c varying linearly with $N(\varepsilon_f)$. However, Eq. (9.2) is only valid in the weak-coupling limit. For strong-coupling with the proper range of parameters[146] the Eliashberg equations may also mimic a linear dependence on $N(\varepsilon_f)$ and therefore this dependence can not be used to rule out a BCS-like mechanism for the superconductivity.

Although measurements had already been performed on the pressure dependence of T_c, no work had yet been reported on the pressure dependence of the transport properties in these compounds. Since we had already overcome the technical difficulties in producing good quality alkali-doped C_{60}, I chose to try to measure the pressure dependence of the resistivity in the Rb_3C_{60} compound. Since we knew the thermal expansion, the goal was to see if ρ was a strong function of pressure and if it was, how was this affecting the previous $\rho(T)$ measurements.

9.2 Experimental apparatus and techniques

In this section I will describe the pressure cell used in this study. The original cell which allowed for measurements up to 20 kbar (hydrostatic pressure) had already been fabricated[147] in the lab by Dr. Ian Parker. Because of the air sensitivity of the Rb_3C_{60} samples I had to modify this cell to allow for the mounting and unmounting of the sample in an inert atmosphere glove-box. This general type of pressure cell is referred to as a self-clamping piston (or bomb) pressure cell. This cell can be used to produce hydrostatic pressures up to 20 kbar (similar to cells in the literature[148,149] are usable to ~30 kbar). However, the current modifications made for the A_xC_{60} work limit this considerably to < 10 kbar. This will be discussed below.

Fig. 9.1 shows a schematic of the various components involved. The pressure cell body, the locking nuts at either end, and the electrical feedthrough heads are made from Beryllium Copper (Bruch Wellman, Engineered materials) which is machinable in its raw state. After machining it is age-hardened according to the annealing schedule supplied by Bruch Wellman[147] resulting in a material which is strong but not brittle. The strength of the cell body is then further increased through a process called autofrettaging, where the cell is pressurized with a lead plug until the walls swell by ~ 0.003". The complete manufacturing details are given in the pressure cell manual written by Dr. Ian Parker.[147]

The sample is mounted on the sample-mounting-transfer-head (SMTH), see Fig. 9.2, and this is plugged into the electrical feedthrough head. The teflon cap is filled with the hydrostatic fluid medium and placed over the sample on the electrical feedthrough head. This is then pushed into the pressure cell body using the lower locking nut which is turned all the way in and left in place. The upper teflon and Be-Cu washers and the tungsten carbide piston are placed in the cell along with the upper locking nut. The tungsten carbide piston is slightly narrower than the bore of the cell to avoid binding

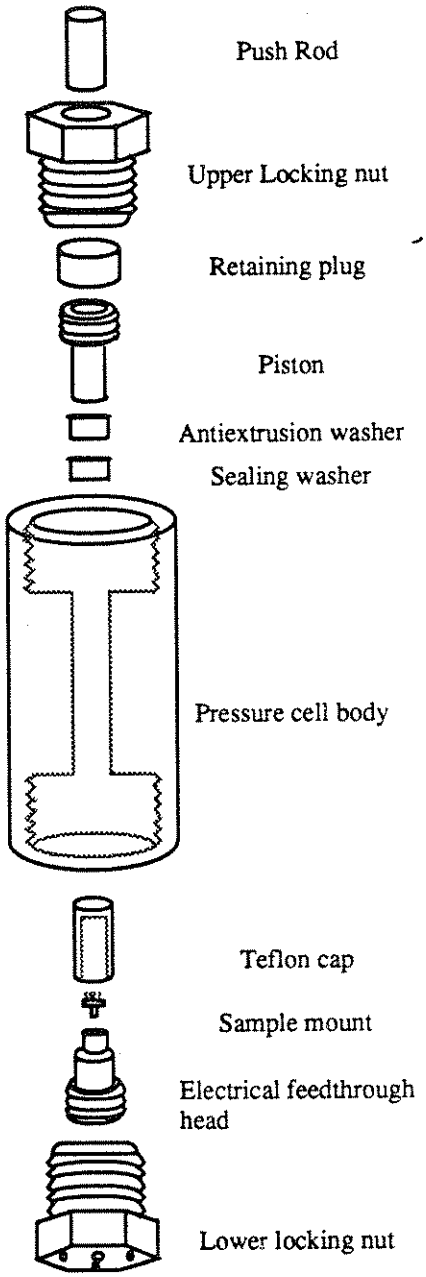

Figure 9.1 Schematic of the various components of the self-clamping pressure cell. The push rod, retaining plug, and piston are made of tungsten carbide, the cap is teflon, the sample mount is Macor and G-10. All other components are Be-Cu.

during the pressurization procedure. The Be-Cu washer makes a very tight fit in the bore of the cell and hence provides the upper sealing point for the cell. The teflon washer helps provide a good seal and keeps the teflon cap from tearing when the cap and electrical feedthrough head are removed from the cell body.

At room temperature, force applied to the upper piston by a conventional press is transmitted to the high-pressure region (inside the teflon cap) and then clamped in by tightening the upper locking nut. Several different hydrostatic fluids are used in this type of cell. The most common fluid referred to in the literature is a 1:1 mixture of *n*-pentane:isoamyl alcohol. Another similar fluid often previously used in the Zettl lab was a 1:1 mixture of *n*-pentane:isopentane. There are two main criteria used to determine the suitability of a hydrostatic fluid medium. First it must not freeze at room temperature for any pressure achieved in the cell. If it freezes, then additional pressure on the piston will result in essentially uniaxial stress on the sample and will lead to damage of the sample, the SMTH and/or the electrical feedthrough head. It is for this reason that mineral oil can not be used as a fluid medium for high pressures since at room temperature it will freeze at a pressure of about 8 kbar. The second criterion is that on cooling the cell the fluid should have a broad freezing transition, preferably going through a slush-like or glassy phase. If the fluid has too sharp of a freezing point then small variations within the cell can quickly destroy the sample and/or lead to anomalous pressure readings due to the shear stresses induced. The use of either mixture of fluids noted above leads to a broad freezing transition around 100 - 150 K. For work with alkali-metal doped C_{60} two additional criteria need be met. First the fluid can not react with raw alkali-metal since otherwise it would destroy the sample. Second, the fluid must not vaporize too quickly at room temperature. It is for this reason the above mixtures proved unsuitable for this work. The reason for this constraint is as follows: The sample is transferred from the doping chamber to the electrical feedthrough head in an inert-atmosphere glove box.

Inside the glove-box the teflon cap must be filled with fluid and placed on the electrical feedthrough head. This assembly must then be passed out of the glove-box and pressed into the pressure cell. It is only at this point that the seal of the teflon cap is good enough to prevent the fluid from vaporizing and escaping from inside the teflon cap. Any vapor region inside the teflon cap from either the initial seal or due to vaporization, will immediately compress under pressure and is likely to cause the top of the cap to be driven down into the sample or the SMTH. Since the transfer and loading procedure takes ~1 - 2 minutes, the high vaporization rates of *n*-pentane:isopentane can lead to vapor pockets forming in the teflon cap with resultant damage to the SMTH upon pressurization. Also, these vapor pockets can be difficult to detect while the sample is in the glove-box and once it is removed, the sample can not easily be returned to the glove-box to refill the teflon cap. The reason is that the sample must pass through the exchange port on the glove-box which has to be pumped and purged several times to reduce the oxygen and water vapor content in the surrounding atmosphere before it can pass inside the glove-box. It is during this pump and purge cycling that the sample quality degrades significantly, probably due to the trace amounts of O_2 and H_2O present on the initial pump down. To solve this problem we chose to use Fluorinert FC-75 (3M Company) as a hydrostatic fluid medium. This fluid is very inert to alkali-metals and can be pressurized[141] to over 20 kbar at room temperature. In addition it does not vaporize quickly and the freezing point, which occurs around 200-230 K for the pressures dealt with in this work, is somewhat broad due to its polymer-like structure. As is typical for organic liquids[150] the temperature at which this fluid seems to solidify increases somewhat with increasing pressure, roughly a few K per kbar.

The details of the sample mounting transfer head and the electrical feedthrough head are shown in Fig. 9.2. The SMTH shown in Fig. 9.2 (a) is removed from the doping chamber using the extraction/insertion tool shown in Fig. 9.2 (b). The tool is

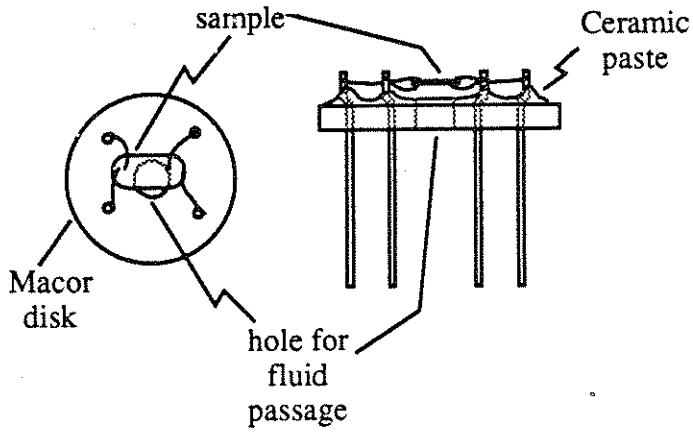

(a)

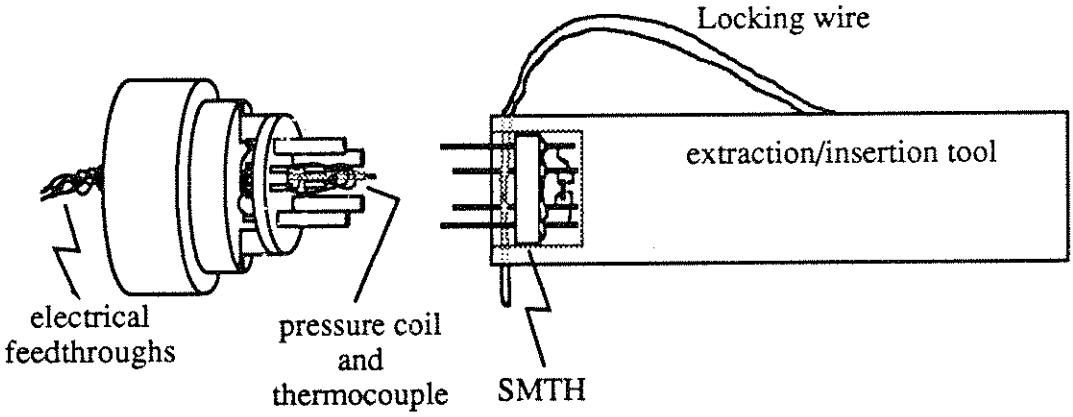

(b)

Figure 9.2 Schematic of the (a) sample-mounting-transfer-head (SMTH) (b) transfer procedure using the extraction/insertion tool.

placed over the SMTH and the locking wire is place underneath the Macor plate. The SMTH is then pulled from the plugs in the doping chamber and inserted into the plugs on the electrical feedthrough head. This method allows one to mount the delicate A_3C_{60} sample on the electrical feedthrough head while wearing the somewhat clumsy gloves in the glove-box. In particular, the wires to the sample could be attached prior to doping and did not have to be reattached when transferred to the electrical feedthrough head in the glove-box. Note that the hole in the center of the SMTH is to allow the hydrostatic fluid to pass freely to either side. Without this hole one is likely to trap vapor behind the SMTH when putting on the teflon cap filled with fluid.

The pressure inside the cell is determined by monitoring the 4-point resistance of a small coil of manganin wire mounted just underneath the SMTH. The resistance R of manganin wire varies linearly with pressure from $0 \leq P \leq 30$ kbar.[149] The typical pressure coefficient of resistance is $\frac{1}{R}\frac{\partial R_o}{\partial P} \sim 2.4 \times 10^{-3}$ per kbar. The exact value of this coefficient is determined by comparison to a standard coil which was calibrated against a commercial pressure sensing device. The pressure coefficient in manganin has been shown[151] to be temperature independent even though the actual resistance R_0 does vary with temperature. Therefore, to compute the pressure one needs to first measure $R(P\approx0,T)$, i.e., the temperature dependence of the resistance when no pressure is applied and then the pressure is determined by

$$P(T) = \frac{\left[R(P,T) - R(P \approx 0, T)\right]}{\left[R(P \approx 0, T) \times \left(\frac{1}{R_o}\frac{\partial R_o}{\partial P}\right)\right]} \tag{9.3}$$

Fig. 9.3 shows $R(P\approx0,T)$ for the manganin coil used in this experiment. Table 9.1 shows the actual raw data. Note that since $\frac{\partial R}{\partial T} \sim 0$ at room temperature, the pressure

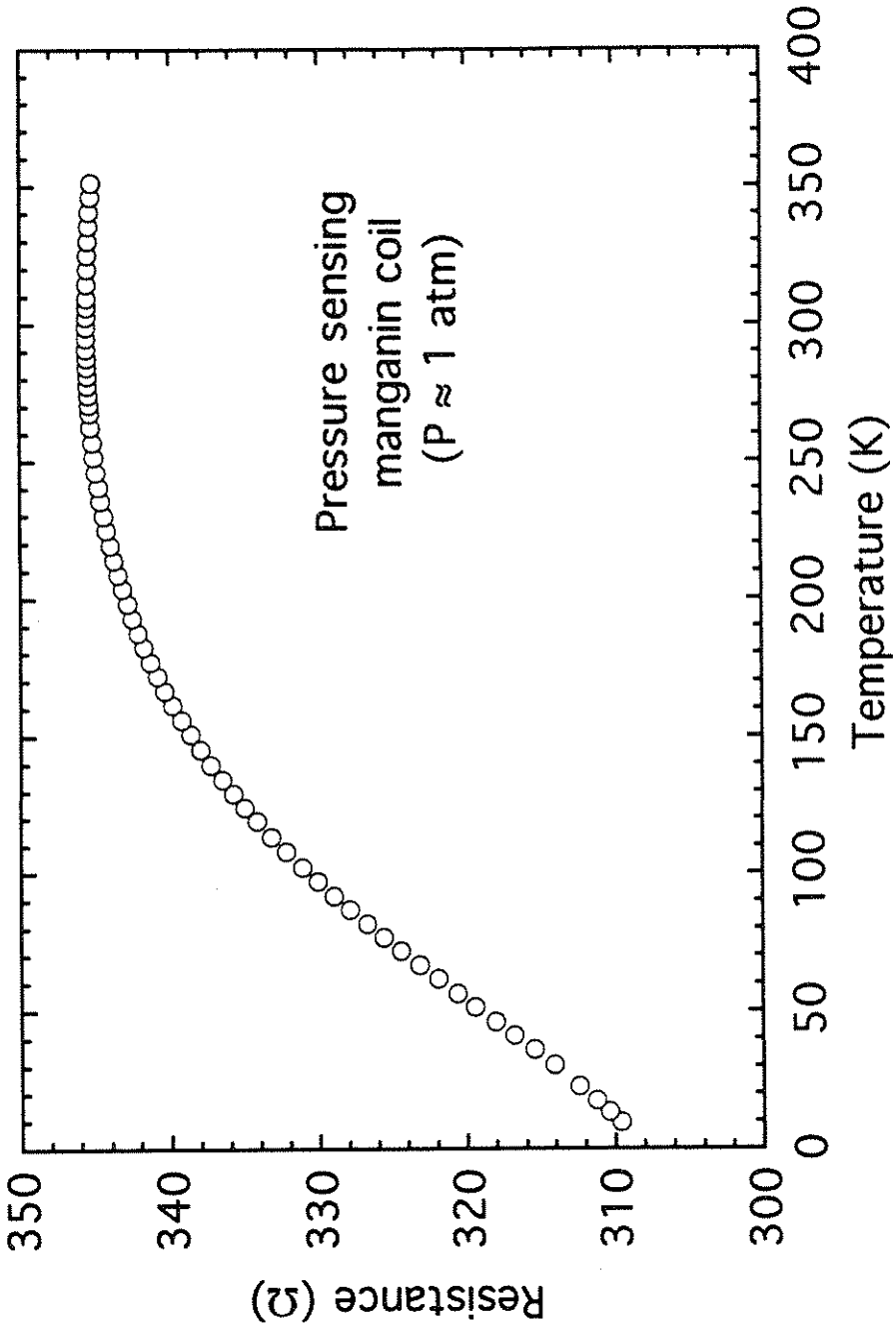

Figure 9.3 Temperature dependence of the resistivity of the pressure sensing manganin coil for $P \approx 0$.

Temp (K)	R (Ohm)	Temp (K)	R (Ohm)	Temp (K)	R (Ohm)	Temp (K)	R (Ohm)	Temp (K)	R (Ohm)	Temp (K)	R (Ohm)	Temp (K)	R (Ohm)
7.6125	309.2912	59.62	321.4865	112.23	333.0416	165.58	340.3036	219.38	344.0353	270.7	345.4104	306.82	345.5945
8.7137	309.4891	60.632	321.7417	113.39	333.2455	166.63	340.406	220.48	344.0835	271.37	345.4179	307.48	345.5935
9.5151	309.6339	61.583	321.9778	114.55	333.4479	167.67	340.5095	221.57	344.1313	272.04	345.4264	308.15	345.592
10.363	309.7905	62.404	322.1887	115.72	333.6479	168.71	340.6064	222.65	344.178	272.7	345.4333	308.81	345.591
11.189	309.9561	63.482	322.4667	116.85	333.8379	169.75	340.7049	223.73	344.2233	273.36	345.4403	309.45	345.589
11.968	310.1228	64.481	322.7209	118	334.0304	170.8	340.8024	224.81	344.2675	274.12	345.4478	310.66	345.5874
12.846	310.3163	65.475	322.9731	119.14	334.2198	171.84	340.8964	225.88	344.3108	274.81	345.4567	311.67	345.5865
13.334	310.4147	66.474	323.2267	120.21	334.3934	172.9	340.9929	226.94	344.3541	275.54	345.4642	312.68	345.584
13.829	310.5107	67.505	323.4828	121	334.5233	173.95	341.0864	228.01	344.3938	276.22	345.4706	313.71	345.58
14.793	310.7082	68.61	323.7564	121.89	334.6675	175	341.1779	229.07	344.4326	276.91	345.4766	314.72	345.574
15.744	310.9141	69.604	324.0011	122.97	334.845	176.05	341.2694	230.13	344.4724	277.65	345.4836	315.71	345.572
16.5	311.0872	70.619	324.2488	124.06	335.0211	177.09	341.358	231.18	344.5102	279.06	345.497	316.7	345.5685
17.45	311.2762	71.702	324.5124	125.17	335.1962	178.14	341.4445	232.23	344.5495	279.77	345.503	317.76	345.5656
18.392	311.4846	72.864	324.7924	126.25	335.3658	179.18	341.5316	233.28	344.5848	280.47	345.5089	318.78	345.5581
19.491	311.7312	74.021	325.0674	127.33	335.5284	180.21	341.6161	234.33	344.6212	281.15	345.5144	319.97	345.5546
20.435	311.957	75.415	325.4017	128.38	335.6906	181.24	341.6987	235.38	344.655	281.83	345.5184	320.99	345.5491
21.454	312.1858	75.972	325.532	129.17	335.808	182.3	341.7832	236.43	344.6888	282.5	345.5244	322.01	345.5442
22.632	312.4459	76.609	325.6822	130.23	335.9661	183.36	341.8673	237.48	344.7206	283.18	345.5293	323.04	345.5378
24.286	312.8235	77.45	325.8756	131.29	336.1243	184.43	341.9503	238.53	344.754	283.85	345.5323	324.08	345.5268
25.674	313.1383	78.165	326.0383	132.17	336.2486	185.51	342.0324	239.58	344.7838	284.52	345.5383	325.12	345.5223
27.27	313.5003	79.259	326.288	133.2	336.4048	186.58	342.1125	240.65	344.8166	285.18	345.5417	326.15	345.5168
28.067	313.6888	80.379	326.5411	134.29	336.5589	187.65	342.1925	241.72	344.8464	285.84	345.5452	327.19	345.5059
30.261	314.1857	81.456	326.7868	135.39	336.7141	188.73	342.2696	242.79	344.8748	286.5	345.5502	328.23	345.5014
31.429	314.4821	82.424	327.0091	136.49	336.8663	189.8	342.3472	243.86	344.9061	287.17	345.5537	329.27	345.49
32.424	314.7199	83.492	327.2534	137.59	337.0155	191.95	342.4959	244.93	344.9325	287.83	345.5567	330.31	345.4845
33.725	315.0168	84.474	327.4756	138.69	337.1662	193.02	342.5685	246.03	344.9604	288.49	345.5602	331.36	345.4766
34.354	315.1416	85.557	327.7209	139.8	337.3134	194.09	342.6402	247.26	344.9922	289.15	345.5627	332.39	345.4661
35.874	315.5072	86.62	327.9571	140.91	337.4601	195.16	342.7098	248.32	345.0171	289.81	345.5656	333.45	345.4552
36.898	315.7683	87.703	328.1933	142	337.6049	196.22	342.7809	249.38	345.0424	290.46	345.5701	334.49	345.4487
37.896	316.0319	88.806	328.4341	143.1	337.7501	197.28	342.847	250.44	345.0673	291.12	345.5721	335.53	345.4418
38.888	316.2935	89.913	328.6743	144.21	337.8924	198.34	342.9127	251.49	345.0897	291.77	345.5736	336.59	345.4279
39.919	316.5606	90.871	328.8777	145.31	338.0326	199.39	342.9769	252.55	345.1135	293.07	345.5781	337.64	345.4224
41.018	316.8421	91.698	329.0523	146.4	338.1709	200.44	343.0425	253.62	345.1359	293.71	345.582	338.7	345.405
42.096	317.1127	92.641	329.2487	147.5	338.3072	201.49	343.1057	254.7	345.1588	294.37	345.5835	339.76	345.4005
43.093	317.3688	93.538	329.4362	148.59	338.4395	202.54	343.1678	255.8	345.1807	295.04	345.586	340.81	345.3876
44.13	317.6334	94.5	329.6337	149.68	338.5708	203.58	343.2275	256.91	345.2011	296.37	345.5885	341.87	345.3796
45.053	317.8682	95.734	329.8834	150.75	338.6976	204.64	343.2897	258.04	345.2234	297.04	345.5905	342.93	345.3632
46.045	318.1158	98.06	330.3499	151.82	338.8224	205.7	343.3499	259.17	345.2458	297.7	345.5915	343.98	345.3597
47.019	318.3645	98.892	330.5121	152.89	338.9463	206.75	343.4081	260.31	345.2632	298.36	345.5915	345.04	345.3473
48.125	318.6445	99.874	330.703	153.94	339.0671	207.8	343.4653	261.46	345.2831	299.05	345.5925	346.1	345.3354
49.253	318.9295	100.95	330.9184	155	339.187	208.85	343.522	262.62	345.302	300.02	345.5934	347.16	345.3229
50.336	319.2031	102.11	331.1497	156.06	339.3039	209.89	343.5782	263.78	345.3199	300.83	345.594	348.22	345.3055
51.413	319.4736	103.35	331.3869	157.12	339.4202	210.94	343.6319	264.94	345.3373	301.5	345.595	349.28	345.2946
52.433	319.7243	104.5	331.6127	158.18	339.5361	211.98	343.6856	266.13	345.3557	302.16	345.5965	350.34	345.2821
53.237	319.9252	105.58	331.8216	159.25	339.65	213.03	343.7368	267.2	345.3627	302.82	345.597	351.39	345.2717
54.2	320.1655	106.66	332.0265	160.31	339.7625	214.06	343.7871	267.74	345.3716	303.48	345.596	352.44	345.2588
55.272	320.4261	107.78	332.2329	161.37	339.8748	215.1	343.8383	268.32	345.3786	304.15	345.596	353.5	345.2448
56.269	320.6713	108.84	332.4314	162.43	339.9857	216.14	343.887	268.88	345.3871	304.82	345.5935	354.53	345.2314
57.317	320.9289	110	332.6417	163.48	340.0937	217.18	343.9353	269.46	345.3945	305.48	345.5955		
58.423	321.195	111.11	332.8427	164.54	340.1996	218.25	343.985	270.03	345.401	306.15	345.594		

Table 9.1 Numerical data shown in Figure 9.3.

readings taken at room temperature while pressurizing the cell are not affected by small fluctuations in the ambient temperature.

Because of differing thermal contractions between the Be-Cu pressure cell walls and the hydrostatic fluid, the sample pressure decreases as the pressure cell is cooled. Typically[148,151,152] the pressure drops by about 3.5 kbar from ~300 K to ~4.2 K and therefore if a predetermined low-temperature pressure is required then this temperature-induced drop must be accounted for by setting the room temperature pressure approximately 3.5 kbar greater than the low-temperature target pressure. Also, if the initial room temperature pressure is ≤ 3.5 kbar then the pressure just falls to ~zero at some temperature and remains ~zero for all lower temperatures. For high initial room-temperature pressure, the pressure falls roughly linearly with temperature down to ~ 220 K at a rate of ~ 0.02 kbar/K. Below ~200 K the pressure in the cell falls somewhat linearly at a new rate of ~ 0.01 kbar/K. This change in the rate of pressure decrease is characteristic[147,151,152] at the freezing point of the hydrostatic fluid medium and hence we conclude that Fluorinert FC-75 freezes around 200-220 K. One difference between Fluorinert and the pentane-based hydrostatic fluids is that for the pentane-based fluids the pressure does not usually continue to fall for temperatures below the freezing temperature (≲100-150 K). However, this is clearly related to the relative size of the thermal expansion coefficient of Be-Cu and that of the frozen fluid medium.

The volume of the high-pressure region inside the teflon cap is considerably reduced during pressurization. For a pressure of 20 kbar the length of the cap may be reduced by up to 10-15 mm. The original cell allowed for a clearance of 20 mm which would safely allow for the cell to be pressurized to 20 kbar without allowing the top of the teflon cap to hit the sample. Because the doped sample could not be exposed to air, we added the sample-mounting-transfer-head which could then be unplugged from the doping chamber and plugged into the electrical feedthrough head. One drawback,

however, was that this significantly raised the height of the sample in the pressure cell cavity such that the top of the teflon cap will compress down and hit the SMTH at a pressure of ~10 kbar (determined by experiment). Therefore, for the measurements performed on samples, at no point was the pressure increased beyond 9.5 kbar.

The final measurement detail to address is temperature measurement. Because of the large thermal mass of the pressure cell and the relatively poor thermal conductivity of the hydrostatic fluid medium, large temperature gradients can be established between the outside of the pressure cell and the sample. Since a diode can not be used in the high pressure region, a two stage temperature measurement technique was employed. First, a diode was used to measure the absolute temperature of a copper block mounted near the pressure cell. Then a chromel/constantan thermocouple which passed through the electrical feedthrough head was used to measure the temperature difference between the copper block and a point inside of the cell very near the sample. It has been shown[153] that a pressure gradient along the length of a thermocouple does not significantly alter the thermopower behavior. This method is more accurate (and more practical) than using a single large thermocouple from inside the cell to room temperature (outside the probe) since this would be > 1 m long and would almost certainly have problems due to strange temperature gradients along the probe combined with inhomogeneities in the wire.

9.3 Pressure dependence of the resistivity in Rb_3C_{60}

Previous studies[33,61,63,90,120,154-156] have shown that the temperature dependence of the resistivity for the doped fullerenes varies as

$$\rho(T) \approx a + bT^2 \qquad (9.4)$$

from T ≈ 100 K to well above room temperature. For a typical metal, the electron-

phonon (el-ph) scattering mechanism is expected to dominate for temperatures $T \geq \theta_D$ (the Debye temperature) resulting in a linear temperature dependence of the resistivity. The presence of a T^2 - like dependence could be evidence for a novel scattering mechanism, e.g., electron-electron scattering.[121] An important observation, however, is that all measurements so far reported for the resistivity of doped fullerenes have been performed at constant sample pressure, $\rho_p(T)$, whereas most theoretical treatments assume constant sample volume, $\rho_v(T)$. Differences between $\rho_p(T)$ and $\rho_v(T)$ have been shown to be important in other compounds including the high T_c oxide superconductors[157] and organic conductors. Given that the compressibility, κ, of the representative material Rb_3C_{60} is comparable to the c-axis compressibility of graphite[138] one is naturally led to the question of how important is the volume dependence of the resistivity in this material. To address this concern, we first look at the pressure dependence of the resistivity at fixed temperature.

For the samples used in this study, the temperature dependence of the resistivity for $P \approx 0$ was determined by measuring $\rho(T)$ in the doping chamber after the doping procedure was completed. The samples displayed the characteristic $\rho_p(T) \sim T^2$ temperature dependence. After ambient pressure measurements, the samples were then transferred to a self-clamping pressure cell in an inert atmosphere glove-box. To insure no sample degradation occurred, the contact and 4-point resistances were measured before and after the transfer procedure and neither were found to have changed. While the pressure cell was on the press the 4-point resistance of the sample and the manganin pressure coil were monitored as the pressure of the cell was increased. The inset to Fig. 9.4 shows the pressure dependence of the normalized resistivity measured at room temperature. Clearly the effect of pressure on the resistivity is quite large with greater than a 50% reduction in ρ at $P = 8$ kbar. There is a small anomaly in the data at $P \approx 2$ kbar which reflects trace amounts of undoped C_{60} in this sample. As shown earlier, for

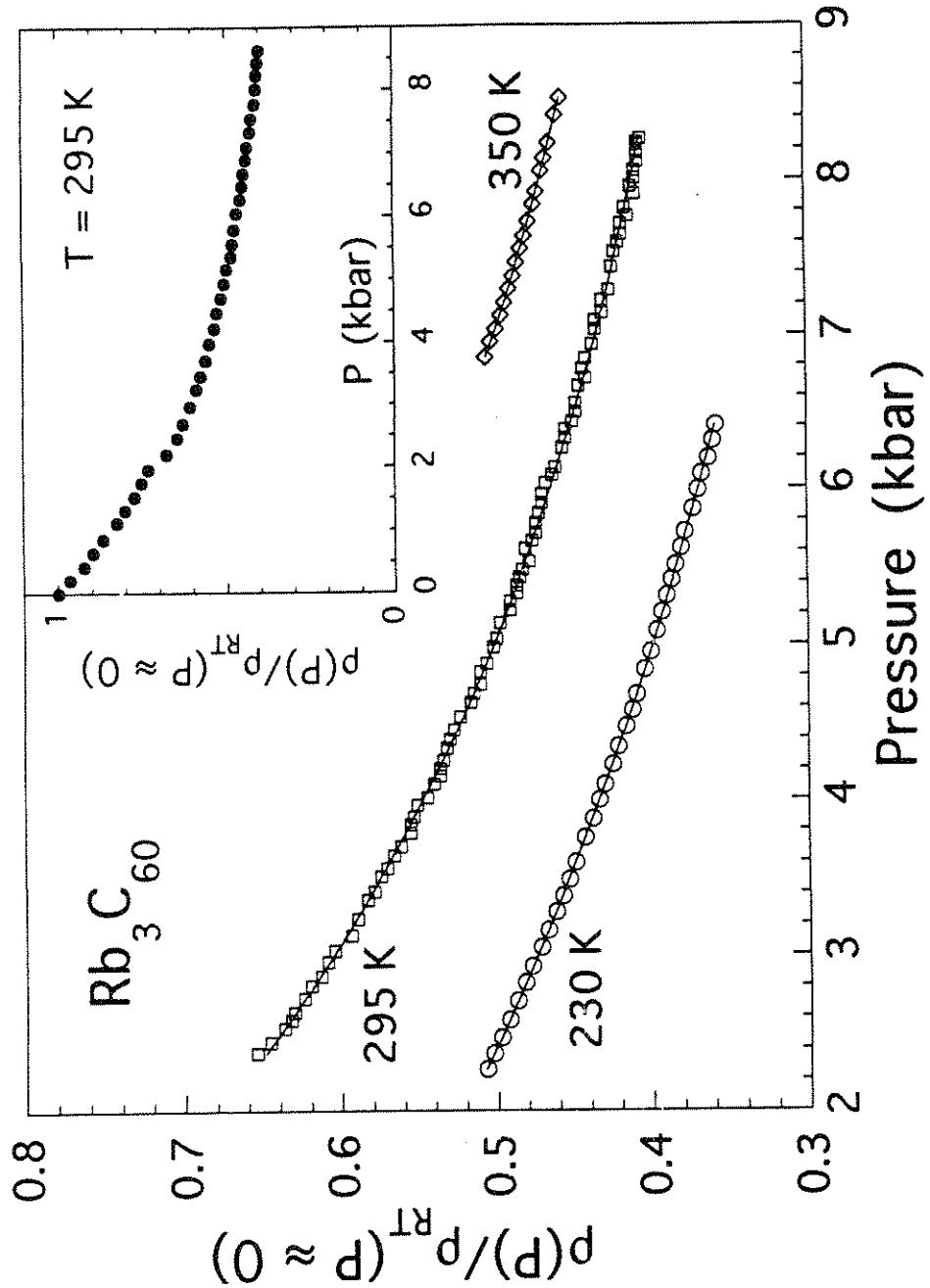

Figure 9.4 Pressure dependence of the resistivity for fixed temperatures. The resistivity is normalized to the room temperature, P ≈ 0 value. For each temperature the data are fit to the form $\rho(P) = \rho_0 + \rho_1 \exp(-P/P_0)$. For T = 230 K, $\rho_0 = 0.18$, $\rho_1 = 0.46$, $P_0 = 6.7$; for T = 295 K, $\rho_0 = 0.31$, $\rho_1 = 0.56$, $P_0 = 4.4$; for T = 350 K, $\rho_0 = 0.36$, $\rho_1 = 0.80$, $P_0 = 4.0$. Inset shows the full $\rho(P)$ curve for T = 295 K.

$P \approx 0$, some samples show a similar anomaly in $\rho_p(T)$ at T = 260 K which is attributed to a strain effect in the sample as the small undoped C_{60} regions undergo a rotational ordering transition (ROT). From data shown in the inset to Fig. 9.4, we find the pressure dependence of the ROT is $dT_{ROT}/dP \approx 16.5$ K/kbar which is consistent[158] with independent measurements.

Unlike $\rho_p(T)$ measurements where the size of the discontinuity stabilizes as the sample is swept back and forth through this ROT temperature (~260 K), if the sample is taken back and forth through the ROT at room temperature by sweeping pressure, the magnitude of the resistivity can increase significantly on each full sweep and the quality of the sample can rapidly diminish. For one sample, after several sweeps through this ROT the general temperature dependence of the resistivity became erratic probably due to the introduction of a significant amount of cracks and other defects. Therefore, only data taken after samples had passed through this ROT only once, on the initial pressurization, were used in this study. Great care was taken to insure that all subsequent measurements were taken such that the small C_{60} regions remained in the rotationally ordered (i.e., frozen) state. The presence of this anomaly in the $\rho_p(T)$ data has already been shown not to affect the measured normalized temperature dependence of the resistivity. Different samples in this study show similar independence to the presence of this anomaly provided the sample only passes through the anomaly once, on the initial pressurization, hence this also strongly implies the measured behavior is intrinsic.

One interesting point to note is that the 2-point contact resistance was reduced by nearly a factor of two with the application of ~8 kbar of pressure. This is very fortunate since it is often difficult to get good 2-point contact resistances to the A_3C_{60} samples. Thus, even if the contact resistances are large the samples may still be measurable under pressure. However, there is one new problem. One sample which had been under ~4 - 8 kbar over several days had the room temperature pressure set to ~2.8 kbar so that at low

temperature it would be under approximately zero pressure. At almost precisely the temperature at which P went to ~zero, all four contacts went bad with resistances > 20 MΩ. This suggests that the application of pressure "pushes" the contacts into the sample making them better while the pressure is applied, but as soon as pressure is removed the contacts are likely to break off, damaging the sample.

The pressure dependence of the resistivity was measured at three different fixed temperatures. To measure the data at 350°C the pressure cell was mounted on the press and then wrapped in heater tape. The same temperature measuring technique used on the low-temperature probe was also used here, namely the temperature of a copper block was measured with a diode and the temperature difference between the block and the inside of the cell was measured with a chromel/constantan thermocouple. The cell was initially under a pressure of about 8 kbar and the temperature slowly increased to ~350°C. Once the temperature was stabilized, the ρ(P) data were taken by varying the pressure applied by the press. The pressure was changed at a rate of less than 0.2 kbar per minute. If the data were taken too quickly (~2 kbar per minute) then a significant response lag between the pressure indicated by the pressure-coil and the resistivity of the sample was observed. For example, if the pressure was changed quickly by 1 kbar and then held fixed as indicated by the coil, the resistance of the sample would continue to change over a period of about 10-60 seconds. Also, the initial room temperature pressurization data indicate that the ROT in pristine C_{60} should occur for a pressure of ~ 5.5 - 6 kbar assuming a linear dependence.[158] To avoid any chance of the sample passing through this transition the value of the pressure was kept > 6.8 kbar for this T ≈ 350°C data. The low temperature ρ(P) data were obtained by filling a liquid-tight container which was made to fit snugly over the pressure cell with a mixture of methanol and dry ice. A small heater was also placed on the pressure cell to help stabilize the temperature. Again, the pressure was changed at a rate of less than 0.2 kbar per minute.

The main body of Fig. 9.4 shows $\rho(P)$ (normalized to the room-temperature, $P \approx 0$ value) for the same sample measured at the three different temperatures. All three sets of data are fit to the same functional form,

$$\rho(P) = \rho_o + \rho_1 \exp(-P/P_o) \tag{9.5}$$

indicated by solid lines. The value of P_o is intrinsic to the material and is not dependent on doping quality. Samples with significantly different ρ's (7mΩ-cm vs. 30mΩ-cm at $T \approx 290K$) yielded roughly the same P_o indicating the exponential form in Eq. (9.5) is not simply due to a percolation effect, e.g., the small change in volume fraction due to the different compressibility's of Rb_3C_{60} and C_{60}. In addition to fitting an exponential, the data can also be fit quite well to the form

$$\rho(P) = \rho_o + \frac{b}{P + P_o} \tag{9.6}$$

In fact, if we assume that the room temperature anomaly which occurs at 2 kbar simply results in an offset of the value of the resistivity then Eq. (9.6) actually fits the additional 0-2 kbar data somewhat better than Eq. (9.5). This offset assumption works relatively well for the $\rho_p(T)$ data which show the anomaly at $T = 260$ K. Of course, both of these fits are merely empirical since at present there is no theoretical understanding of the pressure dependence of the resistivity in this compound.

Given that at room temperature a pressure of ~5.2 kbar yields a reduction in the lattice constant of Rb_3C_{60} comparable to what occurs due to thermal contraction when the sample is cooled from room temperature to T_c, it is clear that the problem of constant volume vs. constant pressure must be addressed.

9.4 Temperature dependent resistivity at constant volume

In a typical temperature-dependent run, the cell was initially pressurized and clamped at room temperature and then the sample resistivity was measured as a function of temperature. As mentioned previously, the sample pressure dropped with decreasing temperature. The pressure dependence of the superconducting transition was determined to be $dT_c/dP = -0.94 \pm 0.1$ K/kbar consistent with previous measurements.[143] The "residual" resistivity, which is quite large in this material, was found to be strongly pressure dependent. By comparing the $\rho(T,P)$ data for different initial pressures, the pressure dependence of ρ at low temperatures was found to be consistent with Eq. (9.5) with $P_0 \approx 3$ - 6 kbar. Typical sources for residual resistivity, e.g., impurities (C_{60}), defects, etc., are not expected to show such a strong and reversible pressure dependence. In addition the ratio $\rho_p(T=290K)/\rho_p(T\approx 0K)$ is roughly equal to 2 for nearly all Rb_3C_{60} samples, even though the magnitude of ρ_p can differ by a factor of five between samples. Therefore the ratio of the room temperature resistivity to the "residual" resistivity is insensitive to the volume fraction of metal and yet shows a strong lattice constant dependence. This implies that the mechanism responsible for the high "residual" resistivity in doped fullerenes is unique and intrinsic. Two possible explanations for the high residual resistivity are that it is related to the rotational disorder known to exist in this material or to a localization effect, both of which would be expected to show a pressure dependence.

To determine the constant-volume resistivity of the sample we exploited the natural pressure drop in the cell with decreasing temperature (which largely compensated for the thermal contraction of the sample). Additional corrections were made to the data as described below. The corrections require knowledge of the thermal expansion coefficient and the bulk modulus of Rb_3C_{60}. The thermal expansion coefficient has been measured[139] and it is $d\ln(a)/dT = 3.05 \times 10^{-5}$ 1/K and linear over the relevant temperature

range. The room temperature bulk modulus is B = 219 kbar.[92,138] The problem remains as to what is the temperature dependence of B. For most materials the bulk modulus is relatively insensitive to temperature. However data for pristine C_{60} do show roughly a linear temperature dependence with a slope of 7.5 - 11% per 100 K. Therefore, we have used two different approximations for B. First we assume the bulk modulus is a constant B_0 independent of temperature, and second we assume it has a linear temperature dependence B(T) with a slope of 11% per 100 K. In our cell, the combination of decreasing temperature and pressure gives rise to a net change in the lattice constant (for T = 295 K to 100 K) of -0.08% for B(T) and -0.18% for B_0 compared to -0.6 % with no pressure compensation. We further correct for this small volume change error as follows: At all temperatures the pressure required to maintain a constant sample volume is known, along with the approximate form of $\rho(P)$. At each temperature point, we determine the additional pressure deviation (from the true experimental pressure cell pressure) necessary to reach the reference sample volume. This pressure deviation is converted to a resistance deviation which is used to correct the measured resistance.

Fig. 9.5(a) shows the corrected and normalized constant-volume resistivity for Rb_3C_{60} for both B_0 (open circles) and B(T) (open diamonds) for the sample initially at a pressure of 8 kbar. In addition, the dashed line indicates the raw data from which the size of the correction can be assessed. Fig. 9.5(b) shows data corrected the same way for the sample initially at a pressure of 6.5 kbar. For the 8 kbar data the resistivity is absolutely **linear** in temperature between 100 K and 350 K for both forms of the bulk modulus. However the slopes of the data differ somewhat depending on the assumption used for B. If an intermediate temperature dependence is used for B then a linear resistivity over this temperature range is still obtained with a slope intermediate to the two sets of data shown in Fig. 9.5(a). The 6.5 kbar data show a linear resistivity for the assumption of a

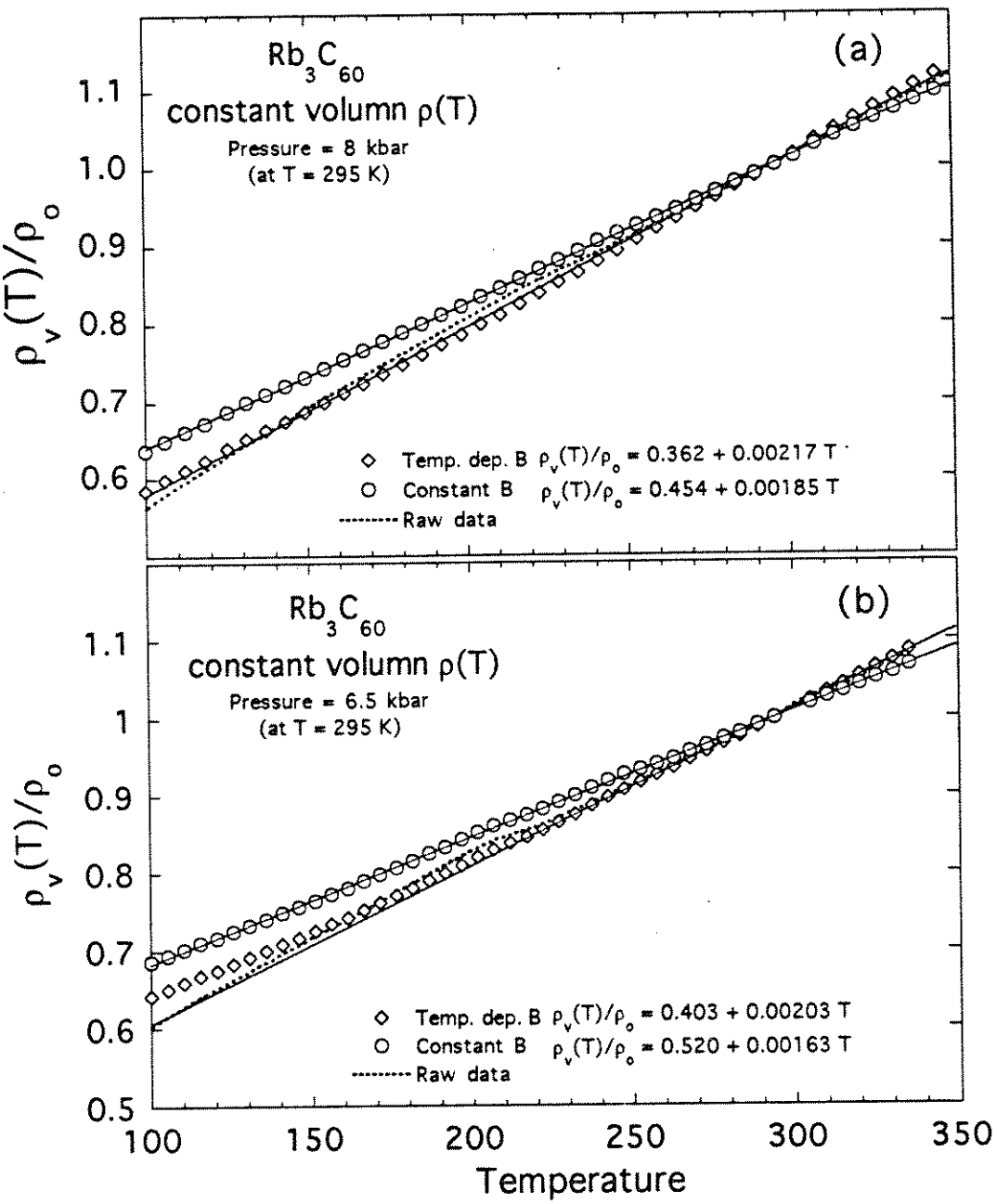

Figure 9.5 Constant volume resistivity vs. temperature for a Rb_3C_{60} sample initially pressurized to (a) 8 kbar and (b) 6.5 kbar. The data are normalized to ρ_o the value of the resistivity at 295 K. The bulk modulus is assumed to be either a constant (open circles) or linearly dependent on temperature (open diamonds). The dashed line corresponds to the raw uncorrected data.

constant B but they show a deviation from linearity at T ≈ 200 K for the assumption of a temperature dependent B. Hence, for temperatures ≥ 200 K and constant sample volume, we find

$$\rho_V(T) = \alpha + \beta T, \tag{9.7}$$

in sharp contrast to Eq. (9.4), $\rho_P(T) \approx a + bT^2$, relevant for constant sample pressure. Depending on the assumption used for the temperature dependence of the bulk modulus the onset of the linearity can occur at anywhere from ~100 K up to ~200 K. Above 200 K the assumption of the temperature dependence of the bulk modulus merely influences the slope of the resistivity however the data still remain highly linear up to the highest temperature measured. Note that the 8 and 6.5 kbar data yield roughly matching slopes for either assumption of the temperature dependence of the bulk modulus however there does appear to be a small pressure dependence with a slight increase in the slope for increasing pressure.

In the high temperature regime the slope of the $\rho_V(T)$ curve, $d\rho/dT$, is related to the transport el-ph coupling constant, λ_{tr} as follows. The transport el-ph coupling constant is defined in terms of the el-ph spectral function $\alpha^2_{tr}F(\omega)$ as

$$\lambda_{tr} = 2\int_0^{\omega_m} \alpha^2_{tr}F(\omega)\,\frac{d\omega}{\omega} \tag{9.8}$$

where the integral is over phonon frequencies ω up to the maximum phonon frequency ω_m which in the Debye model is just the Debye frequency ω_D. The temperature dependent resistivity is given by[159]

$$\rho(T) = \frac{m}{n e^2}\,\tau^{-1} = 4\pi\omega^{-2}\,\tau^{-1} \tag{9.9}$$

where m is the electron mass, n is the number density, ω_p is the plasma frequency and τ^{-1} is the el-ph scattering rate defined as

$$\tau^{-1} = \frac{2\pi}{k_B T}\int_0^{\omega_m} \hbar\omega\,\alpha_{tr}^2 F(\omega)\left[\cosh\left(\frac{\hbar\omega}{k_B T}\right) - 1\right]^{-1} d\omega \tag{9.10}$$

In the high temperature limit, $\hbar\omega/k_B T << 1$ for all $\omega < \omega_m$, Eq. (9.10) reduces to

$$\tau^{-1} = \frac{2\pi}{\hbar}\,\lambda_{tr}\,k_B T \tag{9.11}$$

Hence, the resistivity is predicted to vary linearly with temperature with the relation between the slope of the resistivity and λ_{tr} given by

$$\lambda_{tr} = \frac{\hbar\omega_p^2}{8\pi^2 k_B}\frac{d\rho}{dT} = 0.246(\hbar\omega_p)^2\frac{d\rho}{dT} \tag{9.12}$$

with units $[d\rho/dT] = \mu\Omega$-cm/ K, and $[\hbar\omega_p] = eV$. To solve for λ_{tr}, it is necessary to determine the true value of the slope, $d\rho/dT$. Since Rb_3C_{60} has been shown to be a granular metal[113] we must take into consideration the fact that this granularity can affect the measured slope. In particular, for a typical granular metal the relative slope defined as $\alpha_R = (1/\rho)*d\rho/dT$ can be smaller than that in the pure bulk system. As the volume ratio of the metal approaches unity (i.e., we approach optimum doping in the Rb_xC_{60} system)

the value of α_R should approach a constant value equal to that of the pure metal. The relative slope for the best sample measured in this pressure study ($\rho(T = 295\ K) \approx 7\ m\Omega$-cm) was $\alpha_R \approx 1.9 \times 10^{-3}\ K^{-1}$ assuming a constant B. On the other hand, the sample which had a room temperature resistivity which was four times greater, $\rho(295\ K) \approx 30\ m\Omega$-cm, had a relative slope of $\alpha_R \approx 1.7 \times 10^{-3}\ K^{-1}$ for a constant B. The small difference in α_R between these two samples shows that we are near enough to optimal doping such that α_R is roughly equal to the pure bulk value. Therefore, the different assumptions for B(T) yield a range of values for $\alpha_R = 1.9 - 2.2 \times 10^{-3}\ K^{-1}$ for pure Rb_3C_{60}. To extract λ_{tr} the actual slope $d\rho/dT$ is needed and therefore this value of α_R must be scaled by the true intrinsic value of the resistivity.

The best value for the room temperature resistivity of Rb_3C_{60} comes from two independent measurements: an indirect measurement[99,160] from fluctuation conductivity, and from optical reflectivity.[66,161] Both measurements yield $\rho(295\ K) \approx 0.5\ m\Omega$-cm. Hence $d\rho/dT = 0.95 - 1.1\ \mu\Omega$-cm/K. The range of experimental values for the plasma frequency in Rb_3C_{60} is found[59,162] to be $\omega_p \approx 0.93$-1.67 eV. Using these values of $d\rho/dT$ and ω_p in Eq. (9.12) yields a range of values for the transport coupling constant of $\lambda_{tr} \approx 0.2 - 0.75$. It is important to realize that there are no free parameters involved in this determination of λ_{tr} and yet the range of values obtained is characteristic of a typical metal.

Finally we address the implications of the low temperature limit of the linearity in $\rho_V(T)$. For an electron-phonon scattering mechanism the lower limit of the linearity in the resistivity is closely related to the Debye temperature. In practice, this linearity can extend down to about 1/4 of the Debye temperature.[163] The energies of the intra-ball phonons are on the order of 400-2000 K. Therefore, given the uncertainty in the temperature dependence of the bulk modulus, we can not distinguish whether these high energy modes or the lower energy alkali-C_{60} phonons or the inter-ball phonons are

responsible for the electron scattering mechanism. Most theories[29,31,154,164-166] of superconductivity in this material have focused on the high temperature intra-ball phonons as being the dominantly coupled modes and the inter-ball modes have been ignored. An important point is that in transport measurements the scattering process involves real phonons whereas the superconducting pairing mechanism is a virtual process. Therefore, if a broad range of the high frequency intra-ball optical modes are coupled with roughly equal strength, one expects the number density to be significantly suppressed for increasing phonon energy. As a result, the coupling to all of the intra-ball modes could be quite strong and yet the transport measurements would still be influenced only by the lower energy intra-ball modes at or below room temperature. By similar arguments, the transport may also be strongly influenced by the even lower energy alkali-C_{60} phonons or the inter-ball phonons. However then one needs to address the problem of the failure of the resistivity to saturate when the mean free path becomes comparable to the lattice constant.[120] What role, if any[167], the low energy inter-ball modes play in the superconductivity has yet to be fully resolved.

In conclusion, the constant volume resistivity, $\rho_v(T)$, is found to vary linearly with temperature over a wide range of temperatures, (100-200) to 350 K. This linearity is consistent with the picture that the scattering mechanism is simply of the electron-phonon type with a coupling constant $\lambda_{tr} \approx 0.2$ - 0.75. In addition, the resistivity of Rb_3C_{60} is found to vary strongly with pressure with an empirical exponential or $1/(P+P_o)$ dependence given by Eqs. (9.5) and (9.6), respectively. This strong dependence on pressure, or equivalently lattice constant, accounts for the significant difference between constant volume and constant pressure resistivity verses temperature.

References

[1]H. K. Onnes, Leiden Comm. **120b**, (1911).

[2]J. Bardeen, L. N. Cooper and J. R. Schrieffer, Phys. Rev. **108**, 1175 (1957).

[3]G. M. Eliashberg, Sov. Phys. JETP **111**, 696 (1960).

[4]W. L. McMillan, Phys. Rev. **167**, 331 (1968).

[5]J. G. Bednorz and K. A. Muller, Z. Phys. B **64**, 189 (1986).

[6]C. W. Chu, L. Gao, F. Chen, Z. J. Huang, R. L. Meng and Y. Y. Xue, Nature **365**, 323 (1993).

[7]J. M. Wheatley, T. C. Hsu and P. W. Anderson, Phys. Rev. B **37**, 5897 (1988).

[8]A. F. Hebard, *et al.*, Nature **350**, 600 (1991).

[9]M. S. Whittingham, in *Intercalation chemistry*, M. S. Whittinghame and A. J. Jacobson, Eds. (Academic Press, New York, 1982) pp. 1.

[10]A. R. Ubbelohde, in *Intercalated Layered Materials*, F. Levy, Ed. (D. Reidel Publishing Co., Boston, 1979), vol. 6, pp. 1.

[11]M. S. Whittingham and L. B. Ebert, in *Intercalated Layered Materials*, F. Levy, Ed. (D. Reidel Publishing Co., Boston, 1979), vol. 6, pp. 533.

[12]G. Kirczenow, in *Graphite intercalation compounds I:Structure and dynamics*, H. Zabel and S. A. Solin, Eds. (Springer-Verlag, Berlin, 1990), vol. 14, pp. 59.

[13]E. McRae and J. F. Mareche, J. Mater. Res. **3**, 75 (1988).

[14]N. Daumas and A. Herold, Bull. Soc. Chim. Fr. **5**, 1598 (1971).

[15]J. M. Thomas, G. R. Millword, R. F. Schlogl and H. P. Boehm, Mat. Res. Bull. **15**, 671 (1980).

[16]M. S. Dresselhaus and G. Dresselhaus, Adv. Physics **30**, 139 (1981).

[17]P. C. Eklund, in *Intercalation in layered materials*, M. S. Dresselhaus, Ed. (Plenum Press, New York, 1986), vol. 148, pp. 163.

[18]M. Zanini, S. Basu and J. E. Fischer, Carbon **16**, 211 (1978).

[19]W. Y. Liang, in *Intercalation in layered materials*, M. S. Dresselhaus, Ed. (Plenum Press, New York, 1986), vol. 148, pp. 31.

[20]S. W. Tozer, A. A. Kleinsasser, T. Penney, D. Kaiser and F. Holtzberg, Phys. Rev. Lett. **59**, 1768 (1987).

[21]Y. Koike, Y. H. Iwabuchi S., N. Kobayashi and T. Fukase, Physica C **159**, 105 (1989).

[22]K. Yvon and M. Francois, Z. Phys. B **76**, 413 (1989).

[23]R. M. Hazen, in *Physical properties of high-temperature superconductors*, D. M. Ginsberg, Ed. (World Scientific, Teaneck, NJ., 1990), vol. 2,.

[24]Y. Matsui and S. Horiuchi, Jpn. J. Appl. Phys. **27**, L2306 (1988).

[25]D. B. Mitzi, L. W. Lombardo, A. Kapitulnik, S. S. Laderman and R. D. Jacowitz, Phys. Rev. B **41**, 6564 (1990).

[26]A. Maeda, M. Hase, I. Tsukada, K. Noda, S. Takebayashi and K. Uchinokura, Phys. Rev. B **41**, 6418 (1990).

[27]G. A. Scholz and F. W. Boswell, Solid State Commun. **74**, 959 (1990).

[28]X.-D. Xiang, S. McKernan, W. A. Vareka, A. Zettl, J. L. Corkill, T. W. Barbee and M. L. Cohen, Nature **348**, 145 (1990).

[29]X.-D. Xiang, A. Zettl, W. A. Vareka, J. L. Corkill, T. W. Barbee and M. L. Cohen, Phys. Rev. B **43**, 11496 (1991).

[30]X.-D. Xiang, *et al.*, Science **254**, 1487 (1991).

[31]X.-D. Xiang, W. A. Vareka, A. Zettl, J. L. Corkill, M. L. Cohen, N. Kijima and R. Gronsky, Phys. Rev. Lett. **68**, 530 (1992).

[32]N. Kijima, R. Gronsky, X.-D. Xiang, W. A. Vareka, A. Zettl, J. L. Corkill and M. L. Cohen, Physica C **181**, 18 (1991).

[33]N. Kijima, *et al.*, Physica C **198**, 309 (1992).

[34]N. Kijima, R. Gronsky, X.-D. Xiang, W. A. Vareka, A. Zettl, J. L. Corkill and M. L. Cohen, Physica C **190**, 597 (1992).

[35]N. A. Fleischer, J. Manassen, P. Coppens, P. Lee, Y. Gao and S. G. Greenbaum, Physica C **190**, 367 (1992).

[36]N. A. Fleischer, J. Manassen, P. Coppens, P. Lee and Y. Gao, Superconductivity and its Applications. 5th Annual Conference (Buffalo, NY, 1991), pp. 366.

[37]W. J. Macklin, S. Claude, V. Brien and P. T. Moseley, J. Mat. Chem. **2**, 439 (1992).

[38]M. Ohashi, W. Gloffke and M. S. Whittingham, Sol. St. Ion. **57**, 183 (1992).

[39]M. Mochida, Y. Koike, K. Sasaki, A. Fujiwara, T. Noji and Y. Saito, Physica C **212**, 191 (1993).

[40]Y. Koike, T. Okubo, A. Fujiwara, T. Noji and Y. Saito, Solid State Commun. **79**, 501 (1991).

[41]L. S. Grigoryan and A. R. Arutyunyan, Dokl. Akad. Nauk **313**, 350 (1990).

[42]L. S. Grigoryan and A. R. Harutyunyan, First International Conference. Strongly Correlated Electron States in Condensed Media. SCESCM-91 (Crimea, USSR, 1991), vol. 17, pp. 1073.

[43]L. S. Grigoryan, N. Chakravarty and A. Z. Capri, Mod. Phys. Lett. B **6**, 1843 (1992).

[44]L. S. Grigoryan, R. Kumar, S. K. Malik, R. Vijayaraghavan and A. R. Harutyunyan, Physica C **198**, 137 (1992).

[45]L. S. Grigoryan, *et al.*, Physica C **205**, 296 (1993).

[46]H. Nakashima, *et al.*, International Conference on Materials and Mechanisms of Superconductivity. High Temperature Superconductors III (Kanazawa, Japan, 1991), vol. 1, pp. 677.

[47]T. Okubo, A. Fujiwara, Y. Koike, T. Noji and Y. Saito, International Conference on Materials and Mechanisms of Superconductivity. High Temperature Superconductors III (Kanazawa, Japan, 1991), vol. 2, pp. 847.

[48]H. Kumakura, J. Ye, J. Shimoyama, H. Kitaguchi and K. Togano, Jpn. J. Appl. Phys. **32**, L894 (1993).

[49]M. Tinkham, *Introduction to superconductivity* (Robert E. Krieger Publishing Co., Malabar, Fl, 1980).

[50]M. R. Presland, J. L. Tallon, R. G. Buckley, R. S. Liu and N. E. Flower, Physica C **176**, 95 (1991).

[51]G. Liang, *et al.*, Phys. Rev. B **47**, 1029 (1993).

[52]A. Fujiwara, Y. Koike, K. Sasaki, M. Mochida, T. Noji and Y. Saito, Physica C **208**, 29 (1993).

[53]D. Pooke, *et al.*, Physica C **198**, 349 (1992).

[54]Y. Koike, K. Sasaki, A. Fujiwara, M. Mochida, T. Noji and Y. Saito, Physica C **208**, 363 (1993).

[55]Y. Muraoka, M. Kikuchi, N. Ohnishi, K. Hiraga, R. Suzuki, N. Kobayashi and Y. Syono, Physica C **204**, 65 (1992).

[56]J. M. Wheatley, T. C. Hsu and P. W. Anderson, Nature **333**, 121 (1988).

[57]J. Ihm and B. D. Yu, Phys. Rev. B **39**, 4760 (1989).

[58]P. W. Anderson and R. Schrieffer, in *Physics Today* **44**, No. 6 (1991), pp. 54.

[59]*High temperature superconductivity*, K. Bedell, D. Coffey, D. E. Meltzer, D. Pines and R. Schrieffer, Eds. (Addison-Wesley, Redwood City, CA, 1990).

[60]T. Ito, H. Takagi, S. Ishibashi, T. Ido and S. Uchida, Nature **350**, 596 (1991).

[61]H. C. Montgomery, J. Appl. Phys. **42**, 2971 (1971).

[62]B. F. Logan, S. O. Rice and R. F. Wick, J. Appl. Phys. **42**, 2975 (1971).

[63]L. J. van der Pauw, Philips Res. Repts. **13**, 1 (1958).

[64]T. Sakakibara, T. Goto and N. Miura, Rev. Sci. Instrum. **60**, 444 (1989).

[65]T. Van Duzer and C. W. Turner, *Principles of superconductive devices and circuits* (Elsevier, New York, 1981).

[66]H. Lee N.S., H. McKinzie, D. S. Tannhauser and A. Wold, J. Appl. Phys. **40**, 602 (1969).

[67]J.-P. Issi, in *Graphite intercalation compounds II (Transport and Electronic properties)*, H. Zabel and S. A. Solin, Eds. (Springer-Verlag, New York, 1992), vol. 18, pp. 195.

[68]M. S. Dresselhaus, in *Intercalation in layered materials*, M. S. Dresselhaus, Ed. (Plenum Press, New York, 1986), vol. 148, pp. 1.

[69]N. Bartlett and B. W. McQuillan, in *Intercalation chemistry*, M. S. Whittinghame and A. J. Jacobson, Eds. (Academic Press, New York, 1982) pp. 19.

[70]I. L. Spain, A. R. Ubbelohde, F. R. S. Young and D. A. Young, Phil. Trans. Roy. A **262**, 345 (1967).

[71]I. L. Spain, in *The physics of semimetals and narrow-gap semiconductors*, D. L. Carter and R. T. Bate, Eds. (Pergamon Press, New York, 1971) pp. 177.

[72]P. W. Anderson and Z. Zou, Phys. Rev. Lett. **60**, 132 (1988).

[73]L. P. Gor'kov, Soviet Phys. JETP **9**, 1364 (1959).

[74]J. Bardeen and M. J. Stephen, Phys. Rev. **140**, A1197 (1965).

[75]P. W. Anderson, Phys. Rev. Lett. **9**, 309 (1962).

[76]Y. B. Kim, C. F. Hempstead and A. R. Strnad, Phys. Rev. **131**, 2486 (1963).

[77]T. T. M. Palstra, B. Batlogg, L. F. Schneemeyer and J. V. Waszczak, Phys. Rev. Lett. **61**, 1662 (1988).

[78]M. Tinkham, Physica B **169**, 66 (1991).

[79]P. H. Kes and C. J. van der Beek, Physica B **169**, 80 (1991).

[80]W. Lawerence and S. Doniach, in *Proceedings of the Twelfth International Congerence on Low Temperature Physics*, E. Kanda, Ed. (Academic Press, Kyoto, 1971) pp. 361.

[81]S. Theodorakis, Phys. Rev. B **42**, 10172 (1990).

[82]G. Briceno, M. F. Crommie and A. Zettl, Physica C **204**, 389 (1993).

[83]J. Clem, Bull. Am. Phys. Soc. **35**, 260 (1990).

[84]Y. Iye, A. Watanabe, S. Nakamura, T. Tamegai, T. Terashima, K. Yamamoto and Y. Bando, Physica C **167**, 278 (1990).

[85]P. H. Kes, J. Aarts, V. M. Vinokur and C. J. van der Beek, Phys. Rev. Lett. **64**, 1063 (1990).

[86]D. H. Kim, K. E. Gray, R. T. Kampwirth and D. M. McKay, Phys. Rev. B **42**, 6249 (1990).

[87]J. W. P. Hsu, D. B. Mitzi, A. Kapitulnik and M. Lee, Phys. Rev. Lett. **67**, 2095 (1991).

[88]M. F. Crommie, G. Briceno and A. Zettl, Phys. Rev. B **45**, 13148 (1992).

[89]R. C. Haddon, *et al.*, Nature **350**, 320 (1991).

[90]H. W. Kroto, J. R. Heath, S. C. O'Brian, R. F. Curl and R. E. Smalley, Nature **318**, 162 (1985).

[91]J. P. Lu, X.-P. Li and R. M. Martin, Phys. Rev. Lett. **68**, 1551 (1992).

[92]W. I. F. David, *et al.*, Nature **353**, 147 (1991).

[93]P. A. Heiney, *et al.*, Phys. Rev. Lett. **66**, 2911 (1991).

[94]R. Tycko, G. Dabbagh, R. M. Fleming, R. C. Haddon, A. V. Makhija and S. M. Zahurak, Phys. Rev. Lett. **67**, 1886 (1991).

[95]P. A. Heiney, *et al.*, Phys. Rev. B **45**, 4544 (1992).

[96]S. Hoen, N. G. Chopra, X.-D. Xiang, R. Mostovoy, J. Hou, W. A. Vareka and A. Zettl, Phys. Rev. B **46**, 12737 (1992).

[97]R. Sachidanandam and A. B. Harris, Phys. Rev. Lett. **67**, 1467 (1991).

[98]S. E. Barrett and R. Tycko, Phys. Rev. Lett. **69**, 3754 (1992).

[99]W. Kratschmer, L. D. Lamb, K. Fostiropoulos and D. R. Huffman, Nature **347**, 354 (1990).

[100]B. Morosin and X.-D. Xiang, (unpublished data).

[101]Y. Maniwa, K. Mizoguchi, K. Kume, K. Kikuchi, I. Ikemoto, S. Suzuki and Y. Achiba, Solid State Commun. **80**, 609 (1991).

[102]R. M. Fleming, *et al.*, Phys. Rev. B **44**, 888 (1991).

[103]K. Holczer, O. Klein, S.-M. Huang, R. B. Kaner, K.-J. Fu, R. L. Whetten and F. Diederich, Science **252**, 252 (1991).

[104]M. J. Rosseinsky, *et al.*, Phys. Rev. Lett. **66**, 2830 (1991).

[105]T. T. M. Palstra, R. C. Haddon, A. F. Hebard and J. Zaanen, Phys. Rev. Lett. **68**, 1054 (1992).

[106]H. S. Chen, *et al.*, Appl. Phys. Lett. **59**, 2956 (1991).

[107]P. C. Eklund, A. M. Rao, P. Zhou, Y. Wang, K.-A. Wang, G. T. Hager and J. M. Holden, 4th NEC Symposium on Fundamental Approaches to New Material Phases, Physics and Chemistry of Nanometer Scale Materials (Karuizawa, Japan, 1992), vol. 19, pp. 154.

[108]A. Hamed, Y. Y. Sun, Y. K. Tao, R. L. Meng and P. H. Hor, Phys. Rev. B **47**, 10873 (1993).

[109]T. Arai, Y. Murakami, H. Suematsu, K. Kikuchi, Y. Achiba and I. Ikemoto, Solid State Commun. **84**, 827 (1992).

[110]R. K. Kremer, T. Rabenau, W. K. Maser, M. Kaiser, A. Simon, M. Haluska and H. Kuzmany, Appl. Phys. A **56**, 211 (1993).

[111]D. M. Poirier and J. H. Weaver, Phys. Rev. B **47**, 10959 (1993).

[112]G. P. Kochanski, A. F. Hebard, R. C. Haddon and A. T. Fiory, Science **255**, 184 (1992).

[113]F. Stepniak, P. J. Benning, D. M. Poirier and J. H. Weaver, Phys. Rev. B **48**, 1899 (1993).

[114]A. F. Hebard, (personal communication) .

[115]Y. Maruyama, T. Inabe, H. Ogata, Y. Achiba, S. Suzuki, K. Kikuchi and I. Ikemoto, Chem. Lett. **10**, 1849 (1991).

[116]Y. Maruyama, T. Inabe, M. Ogata, Y. Achiba, K. Kikuchi, S. Suzuki and I. Ikemoto, 4th NEC Symposium on Fundamental Approaches to New Material Phases, Physics and Chemistry of Nanometer Scale Materials (Karuizawa, Japan, 1992), vol. 19, pp. 162.

[117]B. Morosin, P. P. Newcomer, R. J. Baughman, E. L. Venturini, D. Loy and J. E. Schirber, Physica C **184**, 21 (1991).

[118]S. Shimomura, Y. Fujii, S. Nozawa, K. Kikuchi, Y. Achiba and I. Ikemoto, Solid State Commun. **85**, 471 (1993).

[119]N. W. Ashcroft and N. D. Mermin, *Solid State Physics* (Saunders College, Philadelphia, PA, 1976).

[120]J. G. Hou, X.-D. Xiang, A. Zettl and M. L. Cohen, (Submitted to Phys. Rev. Lett.), (1993).

[121]A. H. Thompson, Phys. Rev. Lett. **35**, 1786 (1975).

[122]V. H. Crespi, J. G. Hou, X.-D. Xiang, M. L. Cohen and A. Zettl, Phys. Rev. B **46**, 12064 (1992).

[123]M. C. Martin, D. Koller and L. Mihaly, Phys. Rev. B **47**, 14607 (1993).

[124]B. Abeles, *Granular Metal Films*, R. Wolfe, Ed., Applied Solid State Science (Academic Press, New York, 1976), vol. 6.

[125]C. A. Neugebaueer, Thin Solid Films **6**, 443 (1970).

[126]J. M. Hawkins, S. Loren, A. Meyer and R. Nunlist, J. Am. Chem. Soc. **113**, 7770 (1991).

[127]R. D. Johnson, C. S. Yannoni, H. C. Dorn, J. R. Salem and D. S. Bethune, Science **255**, 1235 (1992).

[128]P. H. M. van Loosdrecht, P. J. M. van Bentum and G. Meijer, Phys. Rev. Lett. **68**, 1176 (1992).

[129]K. Akers, K. Fu, P. Zhang and M. Moskovits, Science **259**, 1152 (1993).

[130]X. D. Shi, A. R. Kortan, J. M. Williams, A. M. Kini, B. M. Savall and P. M. Chaikin, Phys. Rev. Lett. **68**, 827 (1992).

[131]W. Schranz, A. Fuith, P. Dolinar and H. Warhanek, Phys. Rev. Lett. **71**, 1561 (1993).

[132]D. A. Neumann, *et al.*, Phys. Rev. Lett. **67**, 3808 (1991).

[133]D. A. Neumann, *et al.*, J. Chem. Phys. **96**, 8631 (1992).

[134]H. Kasatani, H. Terauchi, Y. Hamanaka and S. Nakashima, Phys. Rev. B **47**, 4022 (1993).

[135]J. E. Fischer, P. A. Heiney, A. R. McGhie, W. J. Romanow, A. M. Denenstein, J. P. McCauley and A. B. Smith, Science **252**, 1288 (1991).

[136]H. Zabel, in *Graphite intercalation compounds I:Structure and dynamics,* H. Zabel and S. A. Solin, Eds. (Springer-Verlag, Berlin, 1990), vol. 14, pp. 101.

[137]R. M. Fleming, A. P. Ramirez, M. J. Rosseinsky, D. W. Murphy, R. C. Haddon and S. M. Zahurak, Nature **352**, 787 (1991).

[138]O. Zhou, *et al.*, Science **55**, 833 (1992).

[139]O. Zhou, *et al.*, Novel forms of carbon, C. L. Renschler, J. J. Pouch and D. M. Cox, Eds. (Mat. Res. Soc., San Fransisco, CA, 1992), vol. 270, pp. 191.

[140]J. E. Schirber, *et al.*, Physica C **178**, 137 (1991).

[141]G. Sparn, *et al.*, Science **252**, 1829 (1991).

[142]S. L. Bud'ko, R. L. Meng, C. W. Chu and P. H. Hor, in *Frontiers of High-Pressure Research*, H. D. Hochheimer and R. D. Etters, Eds. (Plenum Press, New York, 1991) pp. 485.

[143]G. Sparn, *et al.*, Phys. Rev. Lett. **68**, 1228 (1992).

[144] W. A. Vareka and A. Zettl, (Submitted to Phys. Rev. Lett.), (1993).

[145]A. Oshiyama and S. Saito, Solid State Commun. **82**, 41 (1992).

[146]M. L. Cohen and V. H. Crespi, in *Buckminsterfullerenes*, W. E. Billips and M. A. Ciufolini, Eds. (VCH Publishers, New York, 1993) pp. 197.

[147]I. Parker, *Pressure cell manual* (Zettl group, 1990).

[148]H. Fujiwara, H. Kadomatsu and K. Tohma, Rev. Sci. Instrum. **51**, 1345 (1980).

[149]A. Jayaraman, A. R. Hutson, J. H. McFee, A. S. Coriell and R. G. Maines, Rev. Sci. Instrum. **38**, 44 (1967).

[150]A. Quach and R. Simha, J. Phys. Chem. **76**, 416 (1972).

[151]J. D. Thompson, Rev. Sci. Instrum. **55**, 231 (1984).

[152]W. M. Becker and K. Hoo, Rev. Sci. Instrum. **47**, 587 (1976).

[153]D. R. P. Guy, *et al.*, J. Phys. E. **19**, 430 (1986).

[154]X.-D. Xiang, *et al.*, Science **256**, 1190 (1992).

[155]O. Klein, G. Gruner, S.-M. Huang, J. B. Wiley and R. B. Kaner, Phys. Rev. B **46**, 11247 (1992).

[156]W. B. Zhao, X. D. Zhang, Z. Y. Ye, J. L. Zhang, C. Y. Li and D. L. Yin, Solid State Commun. **85**, 945 (1993).

[157]D. M. Ginsberg, W. C. Lee and S. E. Stupp, Phys. Rev. B **47**, 12167 (1993).

[158]G. A. Samara, L. V. Hansen, R. A. Assink, B. Morosin, J. E. Schirber and D. Loy, Phys. Rev. B **47**, 4756 (1993).

[159]G. Grimvall, *The Electron-Phonon Interaction in Metals* (North-Holland Publishing Co., 1991).

[160]X.-D. Xiang, J. G. Hou, V. H. Crespi, A. Zettl and M. L. Cohen, Nature **61**, 54 (1993).

[161]L. Degiorgi, P. Wachter, G. Gruner, S.-M. Huang, J. Wiley and R. B. Kaner, Phys. Rev. Lett. **69**, 2987 (1992).

[162]L. Degiorgi, *et al.*, Phys. Rev. B **46**, 11250 (1992).

[163]J. Friedel, J. Phys. **1**, 7757 (1989).

[164]R. A. Jishi and M. S. Dresselhaus, Phys. Rev. B **5**, 2597 (1992).

[165]M. Schluter, M. Lannoo, M. Needels, G. A. Baraff and D. Tomanek, Phys. Rev. Lett. **68**, 526 (1992).

[166]C. M. Varma, J. Zaanen and K. Raghavachari, Science **54**, 989 (1991).

[167]T. W. Ebbesen, *et al.*, Physica C **203**, 163 (1992).

[168]*International Tables of X-ray Crystallography*, N. F. M. Henry and K. Lonsdale, Eds. (The Kynoch Press, Birmingham, England, 1952), vol. 1.

[169]K. R. Simon, *Mechanics* (Addison-Wesley, Reading, Mass., 1971).

Appendix A

Interpreting Wyckoff indices

The first step is to look up the symmetry in the International Tables for X-ray Crystallography, vol. 1 (ITXC)[168] These tables have necessarily made a choice as to the unit cell directions (**a**,**b**,**c**). If the crystal in question is considered to be oriented with its axes in the same directions as assumed in the table then the symmetry quoted will be one of the standard symmetries. I will discuss this case first and then come back to the problem of how to use the tables if the crystal is assumed to be oriented in a different direction.

As a first example I will consider YBCO which is defined[22] in Table Aa.1. The crystal symmetry is $P_{4/mmm}$ which is one of the standard symmetries. If you look up $P_{4/mmm}$ (or equivalently No. 123) you will find a list of Wyckoff sites along with the associated symmetries. If we look for example at Ba, Table Aa.1 lists it has having a Wyckoff site symmetry of 2*h* with x = 1/2, y = 1/2 and z = 0.19. All of the x,y, and z coordinates given are normalized to a unit cell of 1:1:1. That is why Table Aa.1 also lists the actual unit cell dimensions. The ITXC lists the 2*h* site as having the following symmetries

$$\left(\frac{1}{2}, \frac{1}{2}, z\right) \; ; \left(\frac{1}{2}, \frac{1}{2}, \bar{z}\right) \qquad \text{(Aa.1)}$$

$\bar{z}$ corresponds to the position (1-z). Therefore there are two Ba atoms located at the positions (1/2, 1/2, 0.19) and (1/2, 1/2, 0.81). These values should then be scaled by the actual unit cell dimensions. This process can be repeated for the other atoms in the unit cell which all have similar simple symmetries. Note that the oxygen atoms O1 with Wyckoff symmetry of 2*f* have very low occupancy which results in the chain-like

YBa_2CuO_x $P_{4/mmm}$ $a \approx b \approx 3.9$ Å $c \approx 11.8$ Å

Atoms	Site	x	y	z
Y	(1d)	0.5	0.5	0.5
Ba	(2h)	0.5	0.5	0.19
Cu1	(1a)	0	0	0
Cu2	(2g)	0	0	0.36
O1*	(2f)	0	0.5	0
O2	(2g)	0.5	0	0.15
O3	(4i)	0	0.5	0.38

O1* has a site occupancy of << 1.0

Table Aa.1 Crystal structure of $YBa_2Cu_3O_\delta$ using the standard Wyckoff notation. Data obtain from ref. [22].

structure in the associated CuO planes. The final results for the other atoms are as follows:

Y: (1/2, 1/2, 1/2)

Cu1: (0,0,0)

Cu2: (0, 0, 0.36); (0, 0, 0.64)

O1: (0, 1/2, 0); (1/2, 0, 0) (Aa.2)

O2: (0, 0, 0.15); (0, 0, 0.85)

O3: (0, 1/2, 0.38); (1/2, 0, 0.38); (0, 1/2, 0.62); (1/2, 0, 0.62)

Now to look at a slightly more complicated crystal structure, consider Bi-2212. Table 1.1 lists the Wyckoff symmetries for the various atoms. The overall symmetry is F_{mmm} (or equivalently No. 69). In addition to the local Wyckoff symmetries the ITXC tables show that the F_{mmm} symmetry has four equivalent positions

$$(0, 0, 0); (0, 1/2, 1/2); (1/2, 0, 1/2); (1/2, 1/2, 0) \qquad \text{(Aa.3)}$$

Lets consider the Bi atoms which have a site symmetry of 8*i* and a position of (0, 0, 0.2). The ITXC lists the 8*i* site as having equivalent sites (0, 0, z) and (0, 0, $\bar{z}$). Thus each of these two sites will yield four atom locations by transforming using the four crystal equivalent positions in Eq. (Aa.3). Thus we get a total of 8 Bi atom locations in the unit cell:

$$\left.\begin{matrix}(0,\,0,\,0.2)\\(0,\,0,\,0.8)\end{matrix}\right\}\text{from } 8i \text{ symmetry}$$

$$\left.\begin{matrix}(0,\,1/2,\,0.7)\\(0,\,1/2,\,0.3)\end{matrix}\right\}\text{from } 8i \text{ symmetry} + (0,\,1/2,\,1/2)$$

$$\left.\begin{matrix}(1/2,\,0,\,0.7)\\(1/2,\,0,\,0.3)\end{matrix}\right\}\text{from } 8i \text{ symmetry} + (1/2,\,0,\,1/2) \qquad \text{(Aa.4)}$$

$$\left.\begin{matrix}(1/2,\,1/2,\,0.2)\\(1/2,\,1/2,\,0.8)\end{matrix}\right\}\text{from } 8i \text{ symmetry} + (1/2,\,1/2,\,0)$$

Notice that if the symmetry transformation results in a coordinate larger than 1 or less than 0 then you simply fold it back into the unit cell by adding or subtracting integers until the coordinate is between 0 and 1. This same process can be used to generate the positions of all the other atoms in the unit cell.

As I mentioned earlier, the ITXC has made a choice for the directions of the **a**, **b**, and **c** axes with respect to the symmetry operations. Sometimes, however, it is more convenient to choose a different set of axes to define the actual crystal. For example, in BSCCO we want to define the **c**-axis as being normal to the CuO_2 planes. A different orientation of the axes is referred to as a different setting. Clearly the symmetries in the two systems are related by a coordinate transformation. If the symmetry listed for the material in question is not one of the standard symmetries then you need to look it up in the index of three-dimensional space-group symbols for various settings located in the back of the ITXC. They are organized by crystal symmetries; monoclinic, orthorhombic, etc. In addition, a description of how to perform the transformation on the symmetries is given on pg. 528 of the ITXC. As an example, a refinement of the Bi-2212 structure[22] has the following symmetry: A_{2aa} [C_{cc2}]. The symmetry listed in the square brackets

identifies the standard orientation symmetry. The settings table (pg. 547 in the ITXC) indicates that the relationship between the different crystal axes are

$$\begin{aligned} &\mathbf{a} \rightarrow \mathbf{b} \\ &\mathbf{b} \rightarrow \mathbf{c} \\ &\mathbf{c} \rightarrow \mathbf{a} \end{aligned} \tag{Aa.5}$$

Thus if I distinguish the coordinates by the subscripts 1 for C_{cc2} and 2 for A_{2aa} then

$$\begin{aligned} x_1 &= y_2 \\ y_1 &= z_2 \\ z_1 &= x_2 \end{aligned} \tag{Aa.6}$$

Now to convert the symmetries, lets look at the 8*d* site in C_{cc2} which has the following symmetry equivalent positions:

$$\left(x_1, y_1, z_1\right); \left(\bar{x}_1, \bar{y}_1, z_1\right); \left(\bar{x}_1, y_1, 1/2 + z_1\right); \left(x_1, \bar{y}_1, 1/2 + z_1\right) \tag{Aa.7}$$

First lets take an arbitrary point in the C_{cc2} coordinate system, (0.1, 0.2, 0.3). In the A_{2aa} coordinate system this same point would be represented as (0.3, 0.1, 0.2). Therefore, by analogy, the actual coordinates represented in Eq. (Aa.7) would be represented in the A_{2aa} coordinate system as:

$$\left(z_1, x_1, y_1\right); \left(z_1, \bar{x}_1, \bar{y}_1\right); \left(1/2 + z_1, \bar{x}_1, y_1\right); \left(1/2 + z_1, x_1, \bar{y}_1\right) \tag{Aa.8}$$

Now you need to use Eq. (Aa.6) to express Eq. (Aa.8) in terms of the 2 coordinates:

$$\left(x_2, y_2, z_2\right); \left(x_2, \bar{y}_2, \bar{z}_2\right); \left(1/2 + x_2, \bar{y}_2, z_2\right); \left(1/2 + x_2, y_2, \bar{z}_2\right) \tag{Aa.9}$$

Now you simply drop the subscripts and you have the symmetries in the new setting, i.e. for A_{2aa}. Thus in the A_{2aa} symmetry, the 8*d* sites have the equivalent points

$$(x, y, z); (x, \bar{y}, \bar{z}); (1/2 + x, \bar{y}, z); (1/2 + x, y, \bar{z}) \qquad \text{(Aa.10)}$$

Note that it is important to remember to transform the crystal's equivalent points also. In this case the C_{cc2} equivalent points

$$(0, 0, 0) ; (1/2, 1/2, 0) \qquad \text{(Aa.11)}$$

become

$$(0, 0, 0) ; (0, 1/2, 1/2) \qquad \text{(Aa.12)}$$

Once you have generated the symmetries in the new setting, one uses the same process as before to determine the locations of the atoms in the unit cell.

Appendix B

Relationship between Bulk and Young's modulus.

We first define $\vec{\vec{P}}$ to be the stress tensor and $\vec{\vec{S}}$ the strain tensor. Under the application of a strain let all points in the sample be displace from $\mathbf{r}$ to $\mathbf{r} + \boldsymbol{\rho}(\mathbf{r})$. Define the components of $\mathbf{r}$ as (x, y, z) and of ρ by (ξ, η, ζ). The strain in the material can be written as

$$\nabla\rho = \begin{pmatrix} \partial_x\xi & \partial_x\eta & \partial_x\zeta \\ \partial_y\xi & \partial_y\eta & \partial_y\zeta \\ \partial_z\xi & \partial_z\eta & \partial_z\zeta \end{pmatrix} \qquad \text{(Ab.1)}$$

where $\partial_x\xi \equiv \frac{\partial\xi}{\partial x}$ and similarly for the other components. We only need consider the symmetric part of $\nabla\rho$ since the antisymmetric part describes the rigid rotation of the sample about the point $\mathbf{r} + \rho$.[169] For an isotropic system the most general decomposition of the symmetric part of $\vec{\vec{S}}$ is given by[169]

$$\vec{\vec{S}}_c = \frac{1}{3}\nabla\cdot\rho\,\mathbf{1} = \frac{1}{3}\frac{\Delta(\delta V)}{\delta V}\mathbf{1}$$
$$\vec{\vec{S}}_{st} = \frac{1}{2}\nabla\rho + \frac{1}{2}(\nabla\rho)^{\dagger} - \frac{1}{3}\nabla\cdot\rho\,\mathbf{1} \qquad \text{(Ab.2)}$$

where the dagger means transpose. $\vec{\vec{S}}$ describes the volume compression and $\vec{\vec{S}}_{st}$ is a symmetric traceless tensor. When written this way one can equate the stress and strain tenors as[169]

$$\vec{\vec{P}} = B\,\nabla\cdot\rho\,\mathbf{1} + 2G\,\vec{\vec{S}}_{st} \qquad \text{(Ab.3)}$$

where B is the bulk modulus and G is the shear modulus. If we apply a pure tension force τ per unit area A along **x**, then the definition of the Young's modulus Y is

$$\frac{\tau}{A} = Y \frac{\Delta x}{x} \tag{Ab.4}$$

where Δx is the resulting elongation of the sample. Therefore, what we need to do is write down the components of the stress and strain tensors for a pure tension force and solve the resulting system of equations. This results in the following equality

$$\begin{aligned} \vec{\mathbf{P}} &= \begin{pmatrix} \frac{\tau}{A} & 0 & 0 \\ 0 & 0 & 0 \\ 0 & 0 & 0 \end{pmatrix} \\ &= \begin{pmatrix} \psi - 2G\partial_x\xi & -2G(\partial_x\eta + \partial_y\xi) & -2G(\partial_x\zeta + \partial_z\xi) \\ -2G(\partial_x\eta + \partial_y\xi) & \psi - 2G\partial_y\eta & -2G(\partial_y\zeta + \partial_z\eta) \\ -2G(\partial_x\zeta + \partial_z\xi) & -2G(\partial_y\zeta + \partial_z\eta) & \psi - 2G\partial_z\zeta \end{pmatrix} \end{aligned} \tag{Ab.4}$$

where

$$\psi = \left(\tfrac{2}{3}G - B\right)(\partial_x\xi + \partial_y\eta + \partial_z\zeta)$$

Now from the yy and zz components we get

$$2G\partial_y\eta = 2G\partial_z\zeta = \left(\tfrac{2}{3}G - B\right)(\partial_x\xi + \partial_y\eta + \partial_z\zeta) \tag{Ab.5}$$

so

$$\partial_y\eta = \partial_z\zeta = \left(\frac{2G - 3B}{6B + 2G}\right)\partial_x\xi \tag{Ab.6}$$

Note that this necessarily implies that there must be a change in the lateral dimension even though the force is purely along **x**.

From the xx component we get

$$\frac{\tau}{A} = \left(\frac{2}{3}G - B\right)\left(\partial_x\xi + \partial_y\eta + \partial_z\zeta\right) - \partial_x\xi$$
$$= \left(\frac{9BG}{3B+G}\right)\partial_x\xi \qquad \text{(Ab.7)}$$

Now the **x** component of ρ must be given by αx since the elongation is a cumulative effect. Since $\alpha x = \Delta x$ this defines $\alpha = \Delta x/x$. Hence we see that $\partial_x\xi$ is just $\Delta x/x$ and combining this with Eqs. (Ab.4) and (Ab.7) we arrive at the relation between B, Y, and G

$$Y = \left(\frac{9BG}{3B+G}\right) \qquad \text{(Ab.8)}$$

or

$$B = \frac{1}{3}\frac{YG}{3G-Y} \qquad \text{(Ab.9)}$$

Although this may look like one needs to know both Y and G to determine B we now show that B is roughly proportional to Y and is very insensitive to G. By using symmetry arguments one can show that the general form of $\boldsymbol{\rho}$ is given by

$$\boldsymbol{\rho} = \alpha x\,\hat{\mathbf{x}} + \beta y\,\hat{\mathbf{y}} + \gamma z\,\hat{\mathbf{z}} \qquad \text{(Ab.10)}$$

Using Eq. (Ab.6) and Eq. (Ab.10) we define a new quantity called Poisson's ratio ν as the ratio of the relative lateral contraction to the relative longitudinal extension

$$\nu = \frac{3B - 2G}{6B + 2G} \qquad \text{(Ab.11)}$$

It is straight forward to show that Eq. (Ab.9) can then be rewritten as

$$B = \frac{Y}{3(1-2\nu)} \qquad \text{(Ab.12)}$$

The dimensionless parameter ν is extremely insensitive to the material and is typically equal to about 0.3 for most metals. Thus one can conclude that for isotropic (or cubic) materials any variation in the Young's modulus will be quite closely tracked by the bulk modulus.